DESIGN, SYNTHESIS, AND CHARACTERIZATION OF AMPHIPHILIC MOLECULES FOR BIOMEDICAL APPLICATIONS

by

YINGYUE ZHANG

A dissertation submitted to

Graduate School-New Brunswick

Rutgers, The State University of New Jersey

In partial fulfillment of the requirements

For the degree of

Doctor of Philosophy

Graduate Program in Chemistry and Chemical Biology

Written under the direction of

Dr. Kathryn E. Uhrich

And approved by

_____

_____

_____

_____

New Brunswick, New Jersey

OCTOBER, 2016

ABSTRACT OF THE DISSERTATION

Design, synthesis, and characterization of amphiphilic molecules for biomedical applications

by YINGYUE ZHANG

Dissertation Director:

Kathryn E. Uhrich

Amphiphilic molecules, comprised of both hydrophilic and hydrophobic domains, have been extensively developed and investigated for various biomedical applications. In this dissertation, polymeric and small molecular weight amphiphiles were rationally designed and utilized as atherosclerotic therapeutics, antimicrobials, and liposome stabilizing agent.

Atherosclerosis, a leading cause of mortality in developed countries, is characterized by the buildup of oxidized low-density lipoprotein (oxLDL) within the vascular intima, unregulated oxLDL uptake by macrophages, and ensuing formation of arterial plaque. Amphiphilic macromolecules (AMs) comprised of a branched hydrophobic domain and a hydrophilic poly(ethylene glycol) (PEG) tail have shown promising anti-atherogenic effects through direct inhibition of oxLDL uptake by macrophages. In this study, five AMs with controlled variations were evaluated for their micellar and structural stability in the presence of serum and lipase, respectively, to develop underlying structure-atheroprotective activity relations. In parallel,

molecular dynamics simulations were performed to explore the AM conformational preferences within an aqueous environment. Notably, AMs with ether linkages between the hydrophobic arms and sugar backbones demonstrated enhanced degradation stability and storage stability, and also elicited enhanced anti-atherogenic bioactivity. Additionally, AMs with increased hydrophobicity elicited increased atheroprotective bioactivity in the presence of serum. These studies provide key insights for designing more serum-stable polymeric micelles as prospective cardiovascular nanotherapies.

The rapid emergence of antibiotic-resistant bacteria and lack of efficacious treatments have prompted extensive research in development of novel antimicrobial agents. Inspired by the unique membrane-targeting mechanism of naturally occurring antimicrobial peptides (AMPs), two series of cationic amphiphiles (CAms) were strategically designed with hydrophilic head groups and non-polar domains segregated to opposite sides of the amphiphiles' backbone, known as a facially amphiphilic conformation. This orientation has been determined to be critical to elicit membrane-lytic properties. The CAms self-assembled into supramolecular nanostructures above their respective critical micelle concentrations (CMCs) upon direct dissolution. By systematically tuning the hydrophobicity, CAms with optimized compositions exhibited potent activity against both Gram-positive and Gram-negative bacteria as well as displaying negligible hemolytic activity. Scanning electron microscope and transmission electron microscope images revealed the morphology and ultrastructure changes of bacterial membranes induced by CAm treatment and further attested to their membrane-disrupting mechanism. Additionally, an all-atom molecular dynamics simulation was employed to understand the CAm-membrane interaction on a molecular level. This study shows that these CAms can serve as viable scaffolds for rationally designing the next generation of AMP mimics as effective antimicrobials to combat drug-resistant pathogens.

Sterically stabilized liposomes have been widely used as long-circulating delivery vehicles. They are typically prepared with poly(ethylene glycol)- (PEG-) modified lipids, where the lipid portion is inserted in the lipid bilayers as an anchor and the hydrophilic PEG coats the surface to

prevent liposome aggregation and rapid clearance *in vivo*. However, these steric protection effects are compromised upon systemic administration due to low retention of PEGylated lipids within liposome membranes upon dilution. Bolaamphiphiles (bolas), comprised of two hydrophilic head groups connected by a hydrophobic domain, can predominantly adopt a membrane-spanning configuration that confers robust bilayer retention. Hence, a series of PEG-bolas were developed to increase retention in the lipid bilayer, presumably leading to enhanced integrity of the PEG protective layer, and thus improved colloidal and biological stability (i.e., phagocytosis by macrophages) of resulting liposome formulations. We hypothesized that PEG-bolas with a sufficiently long hydrophobic domain and rigid central group could preferentially extend across lipid bilayers. Liposomes stabilized by PEG-bolas comprised of a biphenyl core and twelve-carbon alkyl chain exhibited similar storage and biological stability compared to conventional PEGylated lipid stabilized liposomes, but with significantly improved retention upon dilution.

In this thesis, bioinspired amphiphiles were rationally designed by mimicking key characteristics of relevant biological molecules. Through systematic structure-activity relationship studies, the physicochemical properties and bioactivity of amphiphiles can be optimized for specific applications.

DEDICATION

This work is dedicated to my parents, Yuhong Li and Zhihong Zhang, for their unconditional love and support, and my husband, Wei Meng, who has continuously supported me in both research and life over the past four years.

ACKNOWLEDGEMENTS

I would like to express my sincere thanks to professors, friends, and family who have guided and supported me throughout this journey. Your advice, company, and understanding have made my Ph.D. life enjoyable and fruitful.

Special thanks to:

My advisor, Dr. Kathryn Uhrich, my committee members, Dr. Larry Romsted, Dr. Deirdre O'Carroll, Dr. Probhas Moghe, my collaborators, Dr. Michael Chikindas, Dr. Vlad Kholodovych, Dr. William Welsh, Dr. Evan Mintzer, Dr. Alan Schilowitz, Dr. Anne Marie Shough, Dr. Ng Man Kit, Dr. Shuji Luo, Dierolf Marcia, Dr. Latrisha Peterson, Ammar Algburi, Qi Li, past and current group members of Uhrich group, Dr. Sabrina Snyder, Dr. Li Gu, Dr. Allison Faig, Dr. Nicholas Stebbins, Dr. Bahar Demirdirek, Dr. Ruslan Guliyev, Dr. Weiling Yu, Dr. Jennifer Chan, Dr. Dalia Abdelhamid, Dr. Hulya Arslan, Dr. Bryan Langowski, Kristina Wetter, Dr. Jason Hackenberg, Dr. Jeannette Marine, Dr. Renxun Chan, Jonathan Faig, Alysha Moretti, Stephan Bien-Aime, Ning Wang, Dania Davie, Yaniv Pines, Drym Oh, Michelle Moy, Kervin Smith, and other current and past undergraduate researchers, my colleagues, Dr. Adam York, Dr. Junlin Sun, Dr. Daniel Lewis, Margot Zevon, Becky Chmielowski, Chenfei Zhao, Boning Wu, Yijie Niu, Letao Yang, Yixiao Zhang, and other graduate students in Chemistry and Chemical Biology department, staff in Chemistry and Chemical Biology department, Allison Larkin, Karen Fowler, Ann Doeffinger, Rutgers Office of Technology Commercialization, Dr. Shan Wan, Dr. Tatiana Litvin-Vechnyak, Dr. Leon Segal, Dr. Lisa Lyu, and my friend, Weijie Zhou.

TABLE OF CONTENTS

LIST OF TABLES

LIST OF ILLUSTRATIONS

ABBREVIATIONS

Abs	Absorbance	ddH_2O	Double-distilled water
ACK	Ammonium-chloride-potassium	DI	Deionized
AMs	Amphiphilic macromolecules	DiI	1,1′-dioctadecyl-3,3,3′,3′-tetramethylindocarbocyanine perchlorate
AMPs	Antimicrobial peptides	DiO	3,3′-dioctadecyloxacarbocyanine perchlorate
ApoE	Apolipoprotein E	DLS	Dynamic light scattering
BHI	Brain-heart infusion	DMAP	4-Dimethylaminopyridine
Bola	Bolaamphiphile	DMEM	Dulbecco's Modified Eagle Medium
BP	Biphenyl	DMF	Dimethylformamide
BZ	Benzene	DMSO	Dimethyl sulphoxide
CAms	Cationic amphiphiles	DPPC	1,2-dipalmitoylphosphatidylcholine
CD36	Cluster of differentiation 36	DPTS	(Dimethylamino)pyridine p-toluene sulphonate
CHO	Cholesterol	DTT	Di-*tert*-butyl *L*-tartrate
CM	Cell membrane	EDC•HCl	1-(3-Dimethylaminopropyl)-2-ethylcarbodiimide hydrochloride
CMC	Critical micelle concentration	EDTA	Ethylenediaminetetraacetic acid
COF	Coefficient of friction	ESI	Electrospray ionization
CTAB	Cetyltrimethylammonium	FBS	Fetal bovine serum
CVD	Cardiovascular disease	FDA	Food and drug administration
CW	Cell wall	FMS	Friction modifiers
DCC	N,N′-dicyclohexylcarbodiimide	FRET	Förster resonance energy transfer
DCM	Dichloromethane	FR-IR	Fourier transform infrared

GPC	Gel permeation chromatography	MTT	(3-(4,5-dimethylthiazol-2-yl)-2,5-diphenyltetrazolium bromide
HEPES	4-(2-hydroxyethyl)-1-piperazineethanesulfonic acid	M_w	Molecular weight
HFRR	High frequency reciprocating rig	MWCO	Molecular weight cutoff
hMDMs	Human monocytes derived macrophages	NPSA	Non-polar surface area
hRBCs	Human red blood cells	OFMs	Organic friction modifiers
HPLC	High performance liquid chromatography	oxLDL	Oxidized low-density lipoprotein
kDa	Kilodalton	PAO	Polyalphaolefin
LDL	Low-density lipoprotein	PBMC	Peripheral blood mononuclear cell
LUV	Large unilamellar vesicles	PBS	Phosphate buffer saline
NHS	N-hydroxysuccinimide	PC	Phosphatidylcholine
NMR	Nuclear magnetic resonance	PDI	Polydispersity index
MC	Monte Carlo	PE	Phosphatidylethanolamine
M-CSF	Macrophage colony-stimulating factor	PEG	Poly(ethylene glycol)
MD	Molecular dynamics	PEO	Poly(ethylene oxide)
MDR	Multi-drug resistant	PG	Phosphatidylglycerol
MFI	Mean fluorescence intensity	POPC	1-palmitoyl-2-oleoyl-*sn*-glycero-3-phosphocholine
MIC	Minimum inhibitory concentration	POPE	1-palmitoyl-2-oleoyl-*sn*-glycero-3-phosphoethanolamine
MMFF	Merck molecular force field	POPG	1-palmitoyl-2-oleoyl-*sn*-glycero-3-phospho-(1'-rac-glycerol)
Mol Vol	Molecular volume	POPS	1-palmitoyl-2-oleoyl-*sn*-glycero-3-phospho-L-serine
MPS	Mononuclear phagocyte system	PPO	Poly(propylene oxide)
MSR	Macrophage scavenger receptor	PVDF	Poly(vinyldidene fluoride)

RES	Reticuloendothelial system
Rh-PE	Rhodamine B 1,2 dihexadecanoyl-*sn*-glycero-3-phosphoethanolamine
PSA	Polar surface area
PTFE	Polytetrafluoroethylene
RPM	Rounds per minute
RPMI	Roswell park memorial institute
SEM	Scanning electron microscope
SDS	Sodium dodecyl sulfate
SI	Selectivity index
SR	Scavenger receptor
TEM	Transmission electron microscopy
TFA	Trifluoroacetic acid
THF	Tetrahydrofuran
TLC	Thin layer chromatography
TMS	Trimethylsilane
TSA	Total surface area
UV/vis	Ultraviolet–visible spectroscopy

1. Introduction

1.1. Amphiphilic Molecules

Amphiphiles are molecules containing both a hydrophobic, nonpolar group and a hydrophilic, polar group [1]. For conventional amphiphiles, while the nonpolar moiety is typically a long alkyl chain with varying carbon numbers, the polar portion can be a charged (anionic, cationic, and zwitterionic) or uncharged group covalently attached to the alkyl chain, such as a carboxylate, sulfate, phosphate, ammonium, or poly(ethylene glycol) (PEG). Due to their tendency to preferentially accumulate at an interface to lower surface tension, amphiphiles are considered surface-active agents, also termed as surfactants [2, 3]. Above a critical micelle concentration (CMC), amphiphiles form self-assembled aggregates (e.g., micelles, liposomes) in aqueous environments via an entropy-driven process to minimize the unfavorable interactions between hydrophobic chains and water (i.e., hydrophobic effect) [4, 5]. For example, one of most widely used amphiphiles, sodium dodecyl sulfate (SDS), spontaneously forms spherical micelles with a hydrophobic core and a hydrophilic corona above its CMC (**Figure 1.1**).

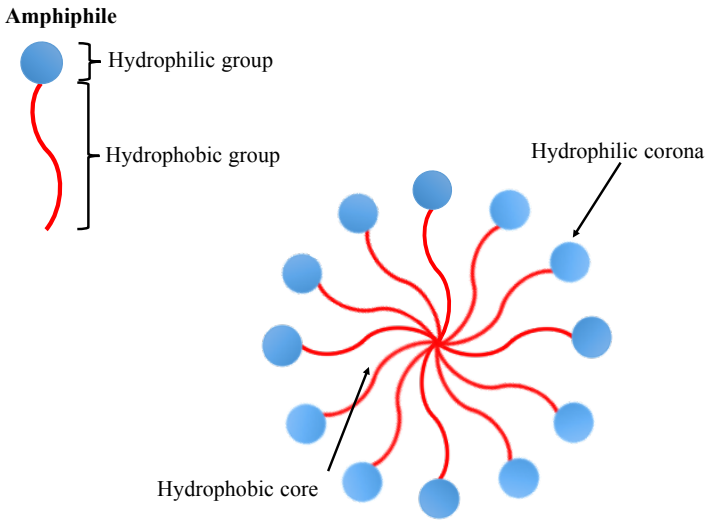

Figure 1.1. Schematic representation of micelle formed by amphiphile.

In addition to conventional amphiphiles with one hydrophilic group and one hydrophobic group, novel amphiphiles with diverse topologies have emerged and attracted considerable attentions in both academia and industry due to their unique solution behaviors [6]. Gemini and bola amphiphiles are two such examples with a wide variety of applications (**Figure 1.2**) [7-9]. Gemini amphiphiles are comprised of two hydrocarbon chains and two hydrophilic head groups, which are connected by a spacer group [10]. This special geometry confers gemini amphiphiles with CMC values roughly two orders-of-magnitude lower than their single chain counterparts. The length and flexibility of spacer groups have a dramatic influence on their organization and presentation, leading to intriguing properties at the air/water interface and aggregation behaviors [10, 11]. In contrast, bola amphiphiles have two hydrophilic end groups linked by one or two long hydrophobic chains. The presence of an additional hydrophilic end group increases the water solubility and raises their CMC values with respect to conventional amphiphiles [12, 13].

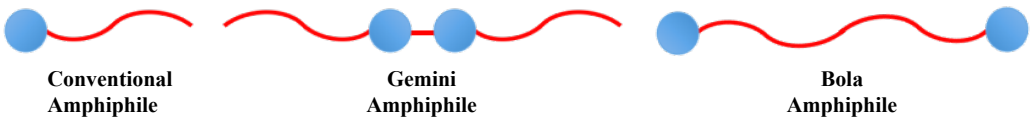

Figure 1.2. Schematic representation of amphiphiles with different topologies, where hydrophilic groups are designated by blue spheres and hydrophobic tail by red lines.

Amphiphiles can be derived from natural or synthetic sources. Phospholipids [14], fatty acids [15], and amphiphilic peptides [16] are commonly known naturally occurring amphiphiles with important roles in biological systems. Advances in synthetic approaches have broadened the structure and chemical compositions of amphiphiles for various applications. While the discussion thus far has focused on small molecule amphiphiles, it is worth noting that amphiphiles can also be polymeric, where at least one component of amphiphile is made of a polymers [17, 18]. Based on the architecture (i.e., distribution of hydrophilic and hydrophobic parts), synthetic polymeric amphiphiles can be further classified into two categories: linear block copolymers and branched polymers (e.g., star-like, comb, graft) [19]. Pluronic®, which consists of two poly(ethylene oxide) (PEO) blocks and one poly(propylene oxide) (PPO) block and is one of the most widely used polymeric amphiphile systems (**Figure 1.3**) [19, 20]. Compared to small molecular weight amphiphiles, polymeric amphiphiles typically have lower CMC values and improved solubilization capacity [21].

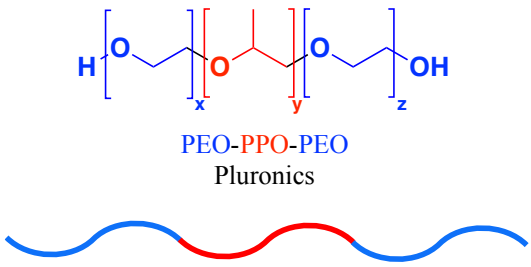

Figure 1.3. Chemical structure of Pluronic® triblock copolymers, where the hydrophilic block denoted in blue and hydrophobic block in red.

1.2. Amphiphile Applications

Owing to their ability to accumulate at interfaces and spontaneously form supramolecular structures, amphiphiles are widely used as detergents, foaming agents, emulsifiers, and dispersants in personal care and cosmetic products [3]. As the organized structures (e.g., micelles, liposomes) formed by amphiphiles are capable of solubilizing hydrophobic compounds, they are also employed as pharmaceutical carriers to improve bioavailability of hydrophobic drugs and protect them from degradation during circulation [22]. Polymeric amphiphiles have exhibited greater promise in biomedical applications as self-assemblies formed by small molecular weight amphiphiles dissociate upon extensive dilution *in vivo*, which is caused by their relatively high CMCs [20]. For instance, the aforementioned tri-block copolymers Pluronic®, first commercialized by BASF as industrial detergents, have been used as micellar anticancer drug carriers to improve efficiency and overcome associated side effects [23, 24].

In addition to applications as delivery vehicles, amphiphilies can exhibit inherent biological activity and thus be used as therapeutics. Amphiphilic peptides have been investigated for their antimicrobial [25] and anticancer [26] properties. Cationic

amphiphilic peptides, as known as antimicrobial peptides, can self-assemble into stable helical structures with functional group presentations that are beneficial for their selective disruption of bacterial membranes over host cells [25]. Amphiphilic materials with specific spatial arrangements and compositions can be rationally designed for various biomedical applications, which are discussed in this thesis.

1.3. Specific Projects

1.3.1. Amphiphilic Macromolecules with Enhanced Physiological Stability as Atherosclerotic Therapeutics

Cardiovascular disease triggered by atherosclerosis is one of the leading causes of adult mortality worldwide [27]. Atherosclerosis is an inflammatory disease characterized by increased plasma levels of low-density lipoproteins (LDL). During early stage of the disease, LDL from the circulating bloodstream enters the artery wall and accumulates in the subendothelial space, where it is chemically modified through oxidation reactions to oxidized LDL (oxLDL). OxLDL triggers recruitment of monocytes and their differentiation into macrophages with upregulated scavenger receptor (SR) expression on their cell surface. The lack of negative feedback mechanisms causes uncontrolled cellular uptake of oxLDL via SRs in macrophages and formation of lipid-laden foam cells. The accumulation of foam cells in artery walls results in plaque formation and buildup, leading to subsequent narrowing of arteries and heart disease [28-30].

Amphiphilic macromolecules (AMs) developed by the Uhrich group are comprised of an acylated branched sugar backbone as the hydrophobic domain and a hydrophilic PEG tail [28-31]. Due to their amphiphilic nature, AMs can self-assemble into micelles at very

low CMCs (10^{-7} – 10^{-5} M) with a PEG corona that may prevent non-specific protein absorption *in vivo*. Interestingly, AMs can effectively inhibit oxLDL uptake through competitive binding to SRs and abrogate the atherosclerotic cascade. Further experiments revealed the importance of AMs' hydrophobicity and anionic charge, which mimic the key characteristics of oxLDL, a natural ligand of SRs [28-30]. AMs with negative charges demonstrated higher bioactivity compared to their neutral analogues, as they could more effectively bind to positive amino acid residues (arginine and lysine) of SRs via electrostatic interactions. The hydrophobic interactions further enhance AMs' interactions with SR binding pockets. Therefore, AMs have been investigated as novel atherosclerotic therapeutics [31].

However, the performance and delivery efficiency of AM micelles *in vivo* upon intravenous administration are influenced by many factors. Specifically, the effects of serum proteins and an esterase were evaluated in this project (**Figure 1.4**). The serum proteins can complex with AM micelles through hydrophobic interactions and induce micelle disassembly, leading to premature clearance and a drastically reduced circulation time. Considering the abundant presence of ester bonds within AM structures, the presence of an esterase, which is capable of catalyzing ester bond hydrolysis, could be particularly detrimental to their *in vivo* performance. The degradation can reduce the bioavailability of AMs below their therapeutic levels, and diminish their potency [30].

In this project, a more predictive model of AM potency *in vivo* was generated for the first time, which provided better insights to identify lead compounds for animal studies. AMs with enzymatically more stable ether linkages were designed and synthetized to impart robust degradation stability and improved bioactivity.

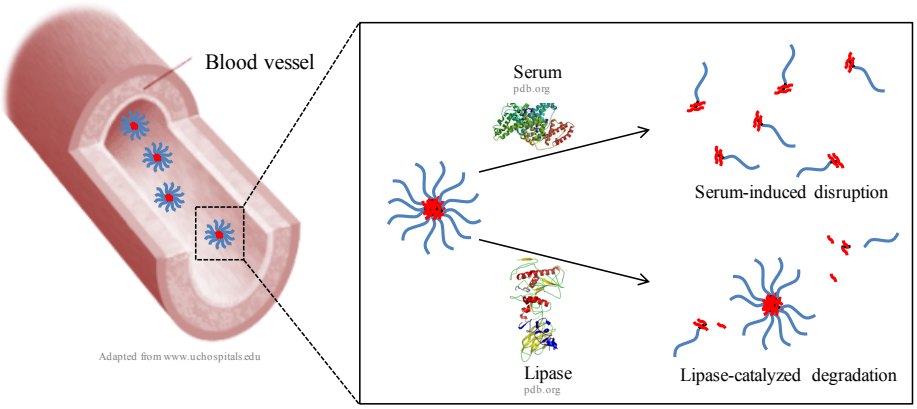

Figure 1.4. Serum proteins and lipase are two major factors that can influence the performance of AMs *in vivo* as atherosclerotic therapeutics.

1.3.2. Cationic Amphiphiles as Antimicrobial Peptide Mimics

The emergence of multi-drug resistant (MDR) bacteria worldwide has become a severe threat to public health due to misuse and overuse of antibiotics [32]. In the United States, at least 2 million people become affected with MDR bacteria each year and at least 23,000 people die as a direct result of these infections [33]. This threat motivates extensive research in exploring antibiotic alternatives [25].

Conventional antibiotics work on a specific biochemical process (e.g., membrane synthesis) or molecule (e.g., enzyme, DNA) of microorganisms, so it is easier for bacteria to develop resistance to through genetic mutation [25]. Naturally occurring antimicrobial peptides (AMPs), as part of immune defense approaches of eukaryotes [2], have attracted substantial interest due to their broad-spectrum activity and high selectivity towards bacteria cells. More importantly, the majority of them can preferentially bind, insert, and destabilize bacterial membranes in addition to interfering with DNA and enzyme synthesis, which largely reduces resistance development [25]. The bacterial cell membrane integrity

is critical in maintaining many essential biological functions including protection, transport, osmoregulation, and biosynthesis [34]. Its disruption can cause various devastating and irreversible processes such as loss of cytoplasm, metabolic dysfunction, and eventual cell death [35].

AMPs are generally 12 to 50 amino acids long with various compositions and sequences (e.g., melittin, magainin) [36]. However, strong evidence accumulated over past decades indicated that it is mainly amphiphilicity is the main contributor to their unique antimicrobial properties [25, 37]. Taking a biomimetic strategy, this project focused on design, synthesis, and evaluation of cationic amphiphiles (CAms) with gemini geometries as potent antimicrobials. CAms were comprised of two cationic ammonium head groups as the hydrophilic domains and saturated hydrocarbon arms as the hydrophobic domains. The influence of linkage type between alkyl arms and the sugar backbone and hydrophobicity were systematically investigated. As they closely resembled AMP architecture, a membrane-targeting mechanism was proposed and validated through electron microscopy.

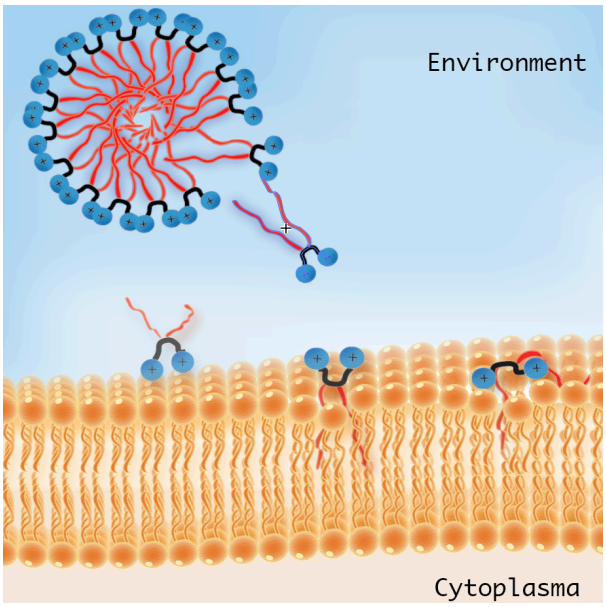

Figure 1.5. CAms can self-assemble into nanoscale micelles and preferentially interact with negatively charged bacteria membrane via electrostatic interactions.

1.3.3. PEGylated Bolaamphiphiles with Enhanced Retention in Liposomes

Liposomes are spherical, enclosed bilayers primarily composed of phospholipids. They have received significant attention as drug delivery vehicles because they can effectively alter the pharmacokinetics and biodistribution to improve drug efficiency and reduce off-target effects [38, 39]. Additionally, liposomes can encapsulate both hydrophobic and hydrophilic drugs in the lipid bilayer and internal aqueous compartment, respectively [40, 41], as biodegradable and essentially non-toxic drug carriers.

The development of long-circulating liposomes, which were shielded with a biocompatible PEG coating, drastically extended liposomes' circulation half-life *in vivo* [42, 43]. Several such liposome-based drug formulations (e.g., Doxil®) have been approved by Food and Drug Administration (FDA) [44]. The most widely used method to prepare long-circulating liposomes is through incorporation of PEGylated lipids. However,

PEGylated lipids have low retention and are likely to diffuse out of lipid bilayers with drastic dilution (e.g., systemic administration), severely compromising the stabilizing effects of the PEG coating and the efficacy of the liposomal delivery vehicle *in vivo* [45, 46]. Consequently, an alternative to PEGylated lipids is urgently needed and would meet a significant medical need.

Bolas are amphiphililic molecules with two polar end groups connected by long alkyl chain spacer(s) [12] that can play a major role in the unusual membrane stability of *Archaebacteria*. Bolas with rigid spacer groups preferably span the membrane and exhibit robust lipid bilayer retention, keeping the membrane intact under harsh conditions [47]. Therefore, novel PEGylated lipids that leverage the bola architecture (i.e., PEGylated bolas) were developed to prepare highly stabilized liposomes. PEGylated bolas with rigid spacer groups could expected to extend completely across the membrane layer to exhibit enhanced membrane retention as well as provide steric protection of liposomes.

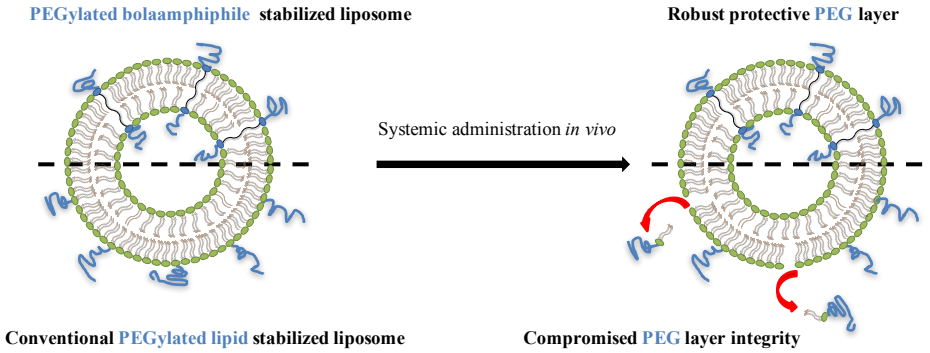

Figure 1.6. PEGylated bolaamphiphiles with membrane-spanning conformation can provide robust protective PEG layer on liposome surface upon systemic administration *in vivo*.

1.4. Summary

Bioinspired amphiphiles were rationally designed by mimicking key characteristics of relevant biological molecules. Through systematic structure-activity relationship studies, the physicochemical properties and bioactivity of amphiphiles can be optimized for specific applications.

This thesis describes three different medical applications that leverage simple hydrophilic and hydrophobic building blocks.

1.5. Reference

[1] Deamer D. Amphiphile. In: Gargaud M, Amils R, Quintanilla JC, Cleaves HJ, Irvine WM, Pinti DL, et al., editors. Encyclopedia of Astrobiology. Berlin, Heidelberg: Springer Berlin Heidelberg; 2011. p. 43-.

[2] Ganz T. The Role of Antimicrobial Peptides in Innate Immunity. Integrative and Comparative Biology. 2003;43:300-4.

[3] Porter MR. Handbook of surfactants: Springer; 2013.

[4] Marsh D. Thermodynamics of Phospholipid Self-Assembly. Biophysical Journal. 2012;102:1079-87.

[5] von Maltzahn G, Vauthey S, Santoso S, Zhang S. Positively Charged Surfactant-like Peptides Self-assemble into Nanostructures. Langmuir. 2003;19:4332-7.

[6] Zana R. Dimeric and oligomeric surfactants. Behavior at interfaces and in aqueous solution: a review. Advances in Colloid and Interface Science. 2002;97:205-53.

[7] Lombardo D, Kiselev MA, Magaz S, Calandra P. Amphiphiles Self-Assembly: Basic Concepts and Future Perspectives of Supramolecular Approaches. Advances in Condensed Matter Physics. 2015;2015:22.

[8] Negm NA, Mohamed AS. Synthesis, characterization and biological activity of sugar-based gemini cationic amphiphiles. Journal of Surfactants and Detergents. 2008;11:215-21.

[9] Zhang X, Wang C. Supramolecular amphiphiles. Chemical Society Reviews. 2011;40:94-101.

[10] Menger FM, Littau CA. Gemini surfactants: a new class of self-assembling molecules. Journal of the American Chemical Society. 1993;115:10083-90.

[11] Shukla D, Tyagi V. Cationic gemini surfactants: a review. Journal of oleo science. 2006;55:381-90.

[12] Fuhrhop J-H, Wang T. Bolaamphiphiles. Chemical reviews. 2004;104:2901-38.

[13] Shimizu T, Masuda M. Stereochemical effect of even-odd connecting links on supramolecular assemblies made of 1-glucosamide bolaamphiphiles. Journal of the American Chemical Society. 1997;119:2812-8.

[14] Dubertret B, Skourides P, Norris DJ, Noireaux V, Brivanlou AH, Libchaber A. In vivo imaging of quantum dots encapsulated in phospholipid micelles. Science. 2002;298:1759-62.

[15] Severson Jr RG. Anionic surfactant, fatty acid. Google Patents; 1985.

[16] Santoso SS, Vauthey S, Zhang S. Structures, function and applications of amphiphilic peptides. Current opinion in colloid & interface science. 2002;7:262-6.

[17] Lundberg P, Walter MV, Montañez MI, Hult D, Hult A, Nyström A, et al. Linear dendritic polymeric amphiphiles with intrinsic biocompatibility: synthesis and characterization to fabrication of micelles and honeycomb membranes. Polymer Chemistry. 2011;2:394-402.

[18] Zupancich JA, Bates FS, Hillmyer MA. Aqueous dispersions of poly (ethylene oxide)-b-poly (γ -methyl- ε -caprolactone) block copolymers. Macromolecules. 2006;39:4286-8.

[19] Raffa P, Wever DAZ, Picchioni F, Broekhuis AA. Polymeric Surfactants: Synthesis, Properties, and Links to Applications. Chemical Reviews. 2015;115:8504-63.

[20] Tadros T. Polymeric surfactants in disperse systems. Advances in Colloid and Interface Science. 2009;147–148:281-99.

[21] Torchilin VP. Structure and design of polymeric surfactant-based drug delivery systems. Journal of Controlled Release. 2001;73:137-72.

[22] Kataoka K, Harada A, Nagasaki Y. Block copolymer micelles for drug delivery: design, characterization and biological significance. Advanced drug delivery reviews. 2001;47:113-31.

[23] Kabanov AV, Batrakova EV, Alakhov VY. Pluronic® block copolymers for overcoming drug resistance in cancer. Advanced drug delivery reviews. 2002;54:759-79.

[24] Zhang W, Shi Y, Chen Y, Yu S, Hao J, Luo J, et al. Enhanced antitumor efficacy by paclitaxel-loaded pluronic P123/F127 mixed micelles against non-small cell lung cancer based on passive tumor targeting and modulation of drug resistance. European Journal of Pharmaceutics and Biopharmaceutics. 2010;75:341-53.

[25] Findlay B, Zhanel GG, Schweizer F. Cationic amphiphiles, a new generation of antimicrobials inspired by the natural antimicrobial peptide scaffold. Antimicrobial agents and chemotherapy. 2010;54:4049-58.

[26] Schweizer F. Cationic amphiphilic peptides with cancer-selective toxicity. European Journal of Pharmacology. 2009;625:190-4.

[27] Glass CK, Witztum JL. Atherosclerosis: the road ahead. Cell. 2001;104:503-16.

[28] Iverson NM, Sparks SM, Demirdirek B, Uhrich KE, Moghe PV. Controllable inhibition of cellular uptake of oxidized low-density lipoprotein: Structure–function relationships for nanoscale amphiphilic polymers. Acta biomaterialia. 2010;6:3081-91.

[29] Abdelhamid DS, Zhang Y, Lewis DR, Moghe PV, Welsh WJ, Uhrich KE. Tartaric acid-based amphiphilic macromolecules with ether linkages exhibit enhanced repression of oxidized low density lipoprotein uptake. Biomaterials. 2015;53:32-9.

[30] Zhang Y, Li Q, Welsh WJ, Moghe PV, Uhrich KE. Micellar and structural stability of nanoscale amphiphilic polymers: Implications for anti-atherosclerotic bioactivity. Biomaterials. 2016.

[31] Faig A, Petersen LK, Moghe PV, Uhrich KE. Impact of Hydrophobic Chain Composition on Amphiphilic Macromolecule Antiatherogenic Bioactivity. Biomacromolecules. 2014;15:3328-37.

[32] Giamarellou H. Treatment options for multidrug-resistant bacteria. Expert review of anti-infective therapy. 2006;4:601-18.

[33] Control CfD, Prevention. Antibiotic resistance threats in the United States, 2013: Centres for Disease Control and Prevention, US Department of Health and Human Services; 2013.

[34] Salton MRJ. Structure and Function of Bacterial Cell Membranes. Annual Review of Microbiology. 1967;21:417-42.

[35] Hartmann M, Berditsch M, Hawecker J, Ardakani MF, Gerthsen D, Ulrich AS. Damage of the Bacterial Cell Envelope by Antimicrobial Peptides Gramicidin S and PGLa as Revealed by Transmission and Scanning Electron Microscopy. Antimicrobial Agents and Chemotherapy. 2010;54:3132-42.

[36] Zasloff M. Antimicrobial peptides of multicellular organisms. nature. 2002;415:389-95.

[37] Pushpanathan M, Gunasekaran P, Rajendhran J. Antimicrobial Peptides: Versatile Biological Properties. International Journal of Peptides. 2013;2013:15.

[38] Samad A, Sultana Y, Aqil M. Liposomal drug delivery systems: an update review. Curr Drug Deliv. 2007;4:297-305.

[39] Torchilin VP. Recent advances with liposomes as pharmaceutical carriers. Nature reviews Drug discovery. 2005;4:145-60.

[40] Khan DR, Rezler EM, Lauer-Fields J, Fields GB. Effects of Drug Hydrophobicity on Liposomal Stability. Chemical Biology & Drug Design. 2008;71:3-7.

[41] Schiffelers R, Storm G, Bakker-Woudenberg I. Liposome-encapsulated aminoglycosides in pre-clinical and clinical studies. J Antimicrob Chemother. 2001;48:333-44.

[42] Immordino ML, Dosio F, Cattel L. Stealth liposomes: review of the basic science, rationale, and clinical applications, existing and potential. International Journal of Nanomedicine. 2006;1:297-315.

[43] Maruyama K, Yamashita A, Suzuki R, Takizawa T, Utoguchi N. Development of PEG-liposomal formulation encapsulating anti-cancer drugs. Maku. 2005;30:298-303.

[44] Barenholz YC. Doxil®—the first FDA-approved nano-drug: lessons learned. Journal of Controlled Release. 2012;160:117-34.

[45] Takeoka S, Mori K, Ohkawa H, Sou K, Tsuchida E. Synthesis and Assembly of Poly(ethylene glycol)-Lipids with Mono-, Di-, and Tetraacyl Chains and a Poly(ethylene glycol) Chain of Various Molecular Weights. J Am Chem Soc. 2000;122:7927-35.

[46] Parr MJ, Ansell SM, Choi LS, Cullis PR. Factors influencing the retention and chemical stability of poly(ethylene glycol)-lipid conjugates incorporated into large unilamellar vesicles. Biochim Biophys Acta, Biomembr. 1994;1195:21-30.

[47] Popov M, Linder C, Deckelbaum RJ, Grinberg S, Hansen IH, Shaubi E, et al. Cationic vesicles from novel bolaamphiphilic compounds. J Liposome Res. 2010;20:147-59.

2. Amphiphilic Macromolecules with Enhanced Physiological Stability as Atherosclerotic Therapeutics

[This work has been published in Biomaterials, year 2016, volume 84, pages 230-240, under the title "Micellar and structural stability of nanoscale amphiphilic polymers: Implications for anti-atherosclerotic bioactivity". Qi Li, William J. Welsh, Prabhas V. Moghe, and Kathryn E. Uhrich are co-authors for this work.]

2.1. Introduction

The American Heart Association's 2015 statistics cite cardiovascular disease (CVD) as the leading global cause of death, accounting for 17.3 million deaths per year. By 2030, the mortality number is expected to grow to more than 23.6 million [1]. Atherosclerosis is an inflammatory disease characterized by increased plasma levels of low-density lipoprotein (LDL), which ultimately lead to arterial plaque development, a key pathology underlying CVDs. During the early stages of the disease, LDL circulating in the bloodstream infiltrates into the arterial wall and accumulates in the subendothelial space, where it undergoes oxidative modification to oxidized LDL (oxLDL). OxLDL triggers monocyte recruitment and their differentiation into macrophages, which leads to scavenger receptor (SR) upregulation on cell surfaces. In addition, the reduced localized positive charge of oxLDL leads to the reduced recognition by the classical LDL receptors but increased affinity to SRs on macrophages [2]. While the uptake of native LDL via LDL receptors is regulated by the intracellular cholesterol content, SR-mediated oxLDL uptake lacks negative feedback mechanisms and leads to uncontrolled oxLDL accumulation. These combined effects result in the conversion of macrophages to foam cells and the formation and subsequent buildup of plaque, where arteries become narrowed and

hardened, becoming one of the focal triggers for stroke, heart attack, or peripheral vascular disease [3, 4].

Conventional CVD therapeutics focus on lowering LDL cholesterol levels (e.g., statin) [5] or reducing plasma triglycerides (e.g., fibrates) [6], both of which contribute to atherosclerosis progression. Due to their systemic administration and their mechanisms of action, these therapies do not directly target atherosclerotic lesion sites and can lead to severe adverse effects (e.g., muscle damage, liver toxicity) [7, 8]. Consequently, novel drug targets including receptors and enzymes that are involved in signaling pathways and lipid metabolism at the sites of atherosclerotic plaque development have drawn tremendous interest over the last few decades [9]. An emerging strategy to abrogate the atherosclerotic cascade locally is through SR inhibition, by managing the disease from upstream events and preventing a series of pro-inflammatory events implicated in the incipient stages of the atherosclerotic cascade [10, 11]. For example, $ApoE^{-/-}$ mice with macrophages deficient in the expression of certain SRs (e.g., macrophage scavenger receptor 1 (MSR1) and cluster of differentiation 36 (CD36)) have demonstrated significant reduction (~ 80%) in lesion area of proximal aorta [12, 13].

Previously, our lab evaluated amphiphilic macromolecules (AMs) consisting of a hydrophobically modified sugar backbone and a hydrophilic poly(ethylene glycol) (PEG) tail that modulated oxLDL uptake and macrophage trafficking [14, 15]. By mimicking the anionic and hydrophobic characteristics of oxLDL and thus eliciting higher binding affinity to SRs, AMs were then designed and explored as SR inhibitors [16]. Subsequent *in vitro* studies revealed their strong potency to inhibit unregulated oxLDL uptake in macrophages primarily through competitive binding with SRs, particularly MSR1 and CD36.

Furthermore, the AM hydrophobic segment with unique 3D presentation served as the synthetic ligand binding domain for SRs, which is distinct from non-bioactive polymers (e.g., Pluronics) with similar composition [17]. Given their amphiphilicity, AMs spontaneously self-assemble into nanoscale micelles in aqueous environments at their critical micelle concentrations (CMC) [18, 19].

To deliver polymeric micelles effectively for biomedical applications, overcoming biological barriers *in vivo* such as serum instability and degradation susceptibility is prerequisite to fully achieving their therapeutic potential. Upon intravenous injection, AM micelles undergo a drastic dilution in the bloodstream and are exposed to a variety of serum proteins, which induce micelle dissociation and reduce circulation time [20, 21]. Due to the fast clearance of unimers by renal filtration, a more stable form of AMs is critical to enable longer blood circulation after intravenous injection and consequently enhanced accumulation in the vascular intima target sites [22]. Previous studies also indicated that the atheroprotective bioactivity of AMs reported in the presence of serum can be significantly lower than serum-free conditions [23], which may be caused by competitive complexation with serum proteins and leading to reduced bioavailability [20]. Furthermore, a range of enzymes in the human body fluids are capable of catalyzing hydrolysis, and their potential impact on AM's plasma concentration or bioavailability must be considered [24] as a minimum effective concentration of AMs is necessary to produce desirable anti-atherosclerotic potency. In view of the abundant presence of ester bonds within AM structures (e.g., ester bond between sugar backbone and PEG), esterase-catalyzed AM degradation could be particularly detrimental to their *in vivo* performance [14].

A rigorous evaluation of AMs under biologically relevant conditions is critical to generate a more predictive model of the AM potency *in vivo*. Building upon our previous work, three ester-linked AMs and two ether-linked AMs were synthesized with systematic modifications expected to enhance biological activity (**Figure 2.1**). The structure-activity relationship was analyzed and a system developed that correlated specific chemical features with anti-atherogenic properties as well as delivery efficacy under physiological conditions. The main parametric variations of chemical structure were relative hydrophobicity, backbone stereochemistry, linkage type, and backbone presentation. The degree of oxLDL uptake in macrophages was quantified by incubating AMs under both serum-free and serum-containing conditions. Solution properties of AM micelles, such as CMC value and half-life time ($t_{1/2}$) in serum, were carefully evaluated to predict their circulation behaviors *in vivo*. These experimental results were correlated to their respective 3D structures and evaluated by computational molecular simulations, which provide insights into key chemical attributes that not only elicit the intended bioactivity but also provide relevant physiochemical properties. Subsequently, the bioactivity of these AMs in lipase-containing conditions was investigated by treating macrophages with AMs that had previously been "conditioned" through exposure to lipase. Lastly, the stability of AM micelles upon storage was assessed to evaluate their translational potential as bioactive formulations.

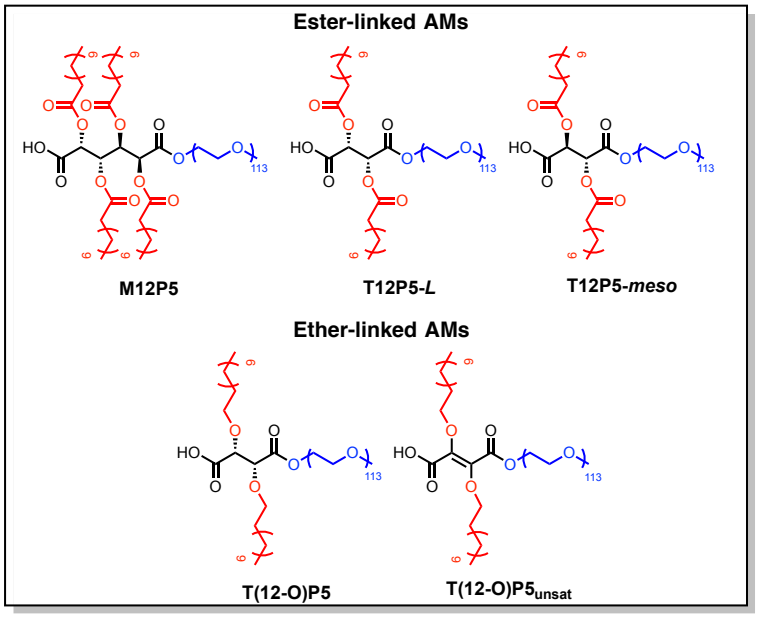

Figure 2.1. Chemical structures of ester-linked AMs and ether-linked AMs. AMs were designed to investigate the role of chemical composition on serum and degradation stability as well as atheroprotective bioactivity. The sugar backbones (black) and hydrophobic arms (red) together confer bioactivity in terms of binding to scavenger receptors for blockage of oxLDL uptake.

2.2. Results and Discussion

2.2.1. AM Synthesis and Characterization

Five AM structures were designed and selected with systematic variations to identify the critical chemical elements that influence bioactivity, serum stability, degradation stability, and storage stability. The hydrophobic domain size was varied to investigate the influence of hydrophobicity, while the backbone was altered to determine the role of stereochemistry and rigidity. In addition, linkage types between the backbone and hydrocarbon arms were modified to study the effect on resultant molecular conformation, physicochemical properties, and bioactivity.

M12P5, T12P5-*meso*, and T12P5-*L* were prepared as previously published [18, 25]. The synthetic scheme of T(12-O)P5 has been previously reported; however, extremely low yield (~ 10%) for the alkylation step using dibenzyl *L*-tartrate has limited its further investigation and evaluation as an atherosclerotic therapeutic [14]. Herein, a new method using di-*tert*-butyl *L*-tartrate as a starting material for the alkylation was developed with significant yield improvement (~ 50%) and reduction of reaction time (**Figure 2.2**). A trace amount of sodium hydroxide was generated during the reaction as NaH reacts with residual water in the solvent, catalyzing benzyl group cleavage and leading to dibenzyl *L*-tartrate consumption. The sterically hindered *tert*-butyl esters minimized hydrolysis, resulting in improved efficiency. Following alkyl arm conjugation, DTT(12-O) was readily deprotected in the presence of strong acid trifluoroacetic acid (TFA) and subsequently subjected to carbodiimide catalyzed PEG coupling. A stoichiometric excess of diacid DTT(12-O) was used to ensure PEG only coupled to one side of the two carboxylic acids. The chemical compositions of AM precursors were confirmed via nuclear magnetic resonance (NMR), fourier transform infrared (FT-IR) spectroscopies and mass spectra, while the successful synthesis of mono-PEGylated AM was verified by ^{1}H-NMR spectroscopy (i.e., AM precursor to PEG ratio) and further confirmed with GPC (i.e., M_w).

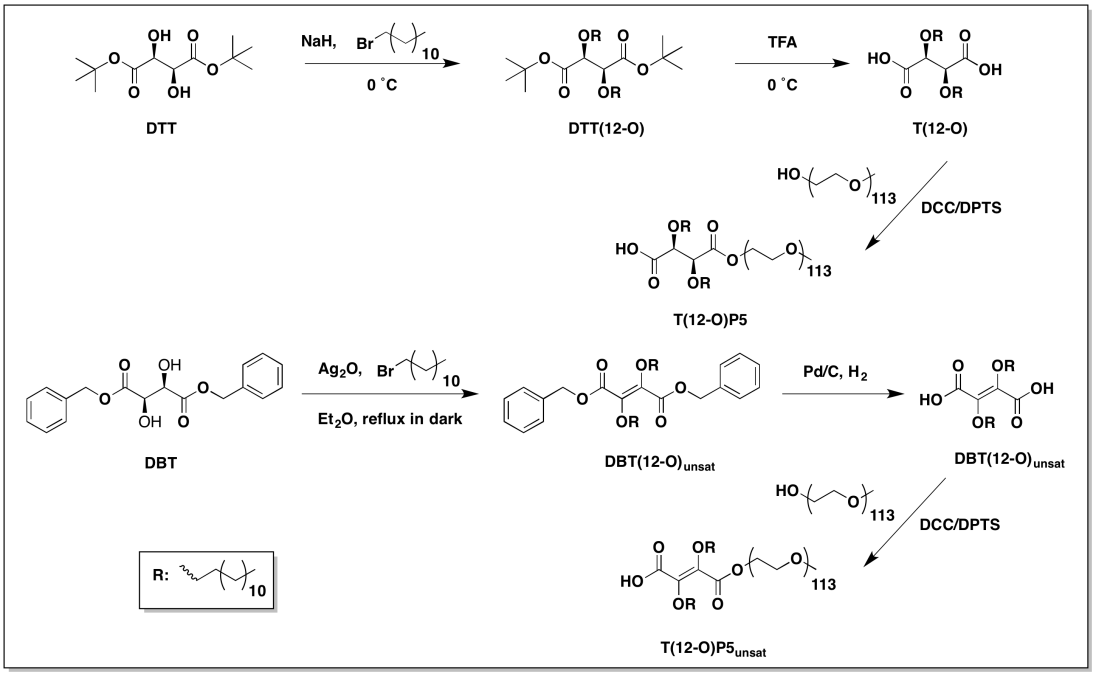

Figure 2.2. Synthetic scheme of ether-linked AMs T(12-O)P5 and T(12-O)$P5_{unsat}$.

To assess the influence of molecular conformation on bioactivity [26], the double bond that restricted rotational flexibility was introduced to the backbone and T(12-O)$P5_{unsat}$ was synthesized. Ag_2O served as both catalyst for ether formation [27] and oxidizing reagent [28] in the first step. The successful synthesis was indicated by the disappearance of the methine backbone peak (**Figure 2.3**). Hydrogenolysis was first attempted to deprotect benzyl groups of DBT(12-O) despite the presence of the unsaturated bond. Interestingly, the double bond was preserved, which is likely attributed to the steric hindrance caused by the bulky alkyl arms. Subsequent PEG coupling was accomplished with reasonably high yield (72 %).

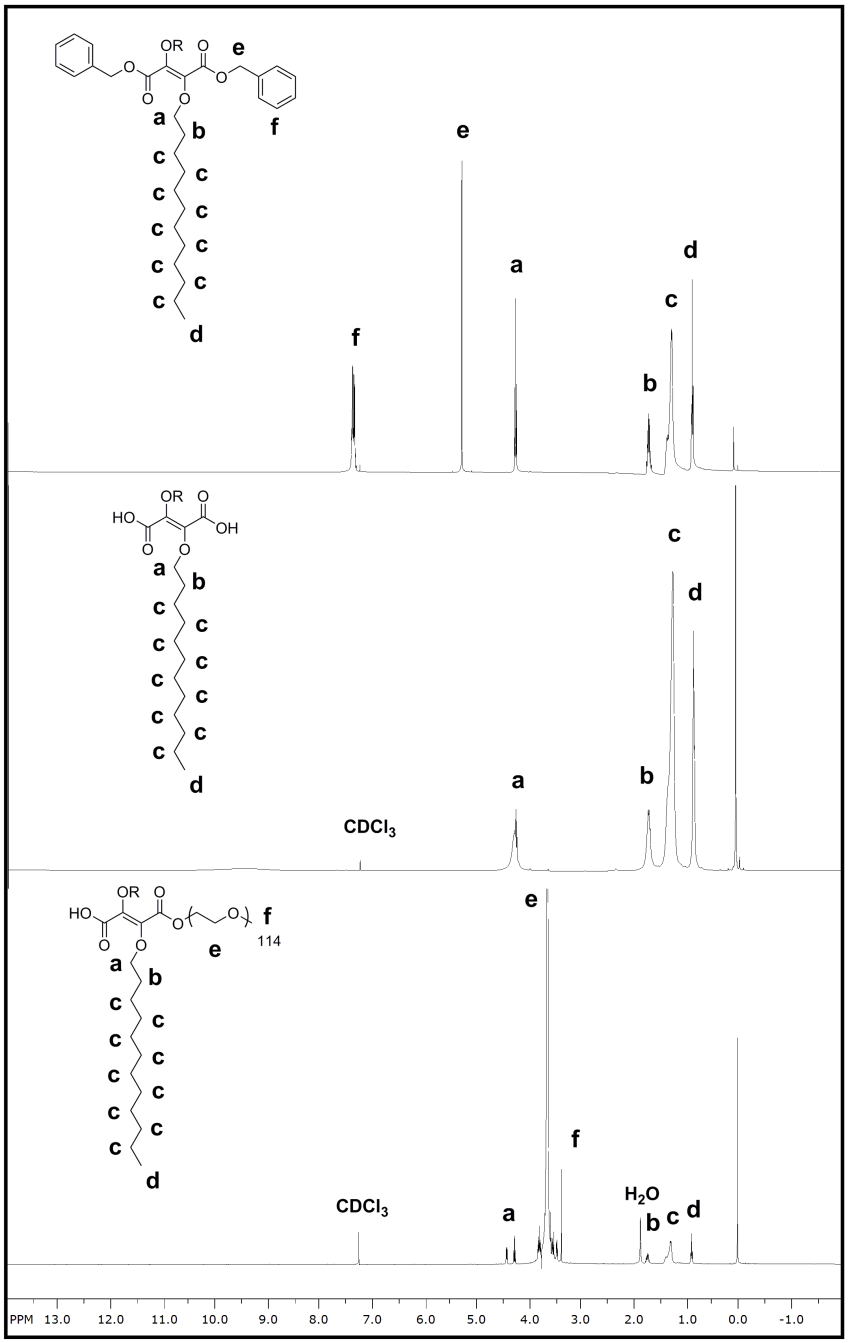

Figure 2.3. ^{1}H NMR spectra of T(12-O)P5$_{unsat}$ confirmed successful synthesis.

Upon successful synthesis, the physicochemical properties of AMs as micelles were evaluated in deionized (DI) water at room temperature (**Table 2.1**). Micelle particle size, surface charge, and CMC values were determined, which are indicators of *in vivo*

stability. To determine the applicability of these micellar systems for *in vivo* delivery, dynamic light scattering (DLS) was employed to measure micelle size. Furthermore, the morphology of micelles was characterized by transmission electron microscope (TEM). Notably, T(12-O)P5$_{unsat}$ exhibited a significant larger size compared to its flexible counterparts. This phenomenon likely due to the rigid hydrophobic domain, leading to a loose packing behavior of micelle hydrophobic core, as observed in molecular simulation. Computer snapshots of ether-linked AMs T(12-O)P5 and T(12-O)P5$_{unsat}$ in their respective low-energy conformations (**Figure 2.5**D and E) revealed improved alignment of the alkyl arms in the former relative to the latter. The arrangement is also reflected by the larger molecular volume and surface area of T(12-O)P5$_{unsat}$ (829 Å^3, 918 Å^2) compared with its flexible analogue T(12-O)P5 (742 Å^3, 824 Å^2) obtained from the simulations in anionic form (**Table 2.2**). All AMs exhibited nanoscale sizes, ranging from 11 nm to 110 nm, considered optimal for extended blood circulation (10 – 200 nm) [22]. Thus, despite variations in sizes, AM micelles were within the size range desirable for drug delivery applications (10 – 200 nm). TEM images provided a direct visualization of morphology of polymeric micelles and indicated that micelles were successfully prepared with AMs with an approximately spherical shape. Additionally, the zeta potential was evaluated as micelle colloidal stability is partially attributed to electrostatic repulsion arising from the net surface charge of the particles [29]. AM micelles exhibited slightly negative charge (~ -1.1 – -2.3 mV), demonstrating a similar degree of electronic stabilization effect.

CMC is defined as the concentration above which unimer (i.e., individual AM molecules) spontaneously self-assemble into micelles, and is assessed by a well-established pyrene assay [18, 19]. Micelles typically undergo tremendous environmental

changes upon intravenous administration, including exposure to serum proteins as well as extensive dilution, leading to dissociation of micelles into unimer form. Low CMC values imply that micelles maintain better integrity upon drastic dilution in the bloodstream, which is beneficial for *in vivo* delivery. Among all formulations tested, mucic acid-derived M12P5 had a CMC value one or two orders-of-magnitude lower than all the tartaric acid (TA)-derived AM micelles, implying a better stability towards dilution. As the micellization process is driven by hydrophobic interactions [30], the observed difference in CMC likely stems from M12P5 having a larger hydrophobic domain (4 hydrocarbon arms) than tartaric-acid based AMs (2 hydrocarbon arms), resulting in a stronger hydrophobic interaction. This observation is confirmed by calculated values of the non-polar surface area (NPSA) of the low-energy conformers (**Table 2.2**), indicating the AM hydrophobicity. Specifically, the NPSA is at least 50% larger for M12P5 compared with the other four TA-based AMs in this study. Overall, all AMs exhibited very low CMC values (10^{-7} – 10^{-5} M) compared to current drug delivery systems under investigation [31, 32], suggesting their promise for drug delivery applications.

Table 2.1. Physicochemical properties of ester-linked AMs and ether-linked AMs as micelles at room temperature.

	Ester-linked AMs			**Ether-linked AMs**	
AMs	M12P5	T12P5-*meso*	T12P5-*L*	T(12-O)P5	T(12-O)P5$_{unsat}$
Micelle size (nm)	23.7 ± 0.3	11.6 ± 1.1	15.2 ± 0.4	18.0 ± 0.2	110.0 ± 10.0
Zeta potential (mV)	-2.1 ± 0.3	-1.1 ± 0.6	-2.3 ± 0.8	-2.1 ± 0.7	-1.3 ± 0.6
CMC (mol/L)	1.2×10^{-7}	6.1×10^{-6}	6.5×10^{-5}	8.9×10^{-6}	7.0×10^{-5}

2.2.2. AM Biological Activity

Despite the importance of administering AMs above their CMCs to ensure successful delivery in a biological setting, micelle formation has a minimal influence on the corresponding anti-atherosclerotic activity compared to chemical composition, as shown previously [33]. To evaluate the influence of a single chemical structural change on bioactivity, human monocytes derived macrophages (HMDMs) were first coincubated with AMs at 10^{-6} M and fluorescently-labeled oxLDL for 24 h under serum-free conditions, after which oxLDL uptake was quantified with flow cytometry (**Figure 2.4**). It was previously demonstrated and further confirmed herein that oxLDL uptake levels were markedly reduced with 10^{-6} M M12P5 treatment (~ 17%), and thus, M12P5 is referred to as the "gold standard" for these studies [17]. Compared to M12P5, T12P5-*meso* with reduced hydrophobicity exhibited a comparable effect on oxLDL uptake inhibition effect (~ 27%), suggesting that hydrophobicity is not the exclusive determinant of bioactivity. However, T12P5-*L* with differing backbone stereochemistry compared to T12P5-*meso*, presented little inhibitory effect and oxLDL uptake remained as high as 78%, demonstrating that sugar backbone stereochemistry is critical to enhance bioactivity. To examine the effect of linkage type and backbone flexibility, T(12-O)P5 was compared to T12P5-*L* and T(12-O)$P5_{unsat}$, respectively. Replacing the ester linkage with ether linkage, T(12-O)P5 inhibited oxLDL uptake to a greater extent and lowered levels of intracellular oxLDL to nearly basal levels (~ 10%). In contrast, the introduction of a rigid functionality into the sugar backbone did not elicit enhancement of bioactivity. In fact, the *trans* double bond of T(12-O)$P5_{unsat}$ showed no bioactivity compared to the oxLDL-only control group (i.e., no AM treatment). Collectively, these results highlight the key criteria for bioactivity:

backbone stereochemistry, linkage type, and molecular conformation conferred by backbone presentation. Overall, M12P5, T12P5-*meso*, and T(12-O)P5 significantly reduced cellular uptake of oxLDL in macrophages to basal level.

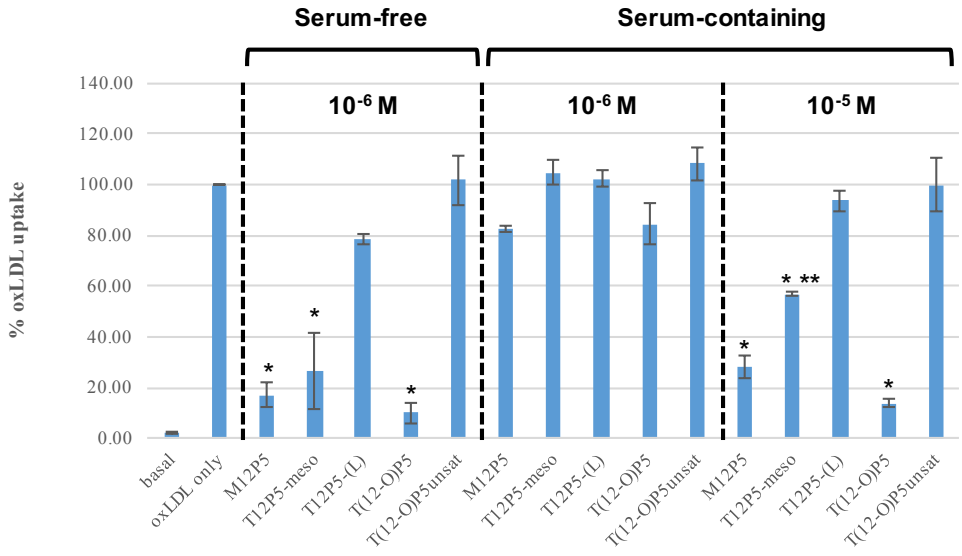

Figure 2.4. Effect of serum and concentration on AMs' oxLDL uptake inhibitory effects. HMDMs treated with AMs under the same condition (i.e., concentration and serum presence or absence) are grouped between dashed lines. The single asterisk (∗) represents a significant difference from the positive oxLDL only control. The double asterisk (**) indicates significant difference compared to M12P5 and T(12-O)P5 at 10^{-5} M under serum-containing conditions.

To mimic physiological conditions, AM's ability to block oxLDL uptake under serum-containing conditions was also investigated. However, at the same concentration (10^{-6} M), all AMs lost their biological activity in the presence of serum proteins. Similar observations were reported in the literature with other therapeutics, which may result from serum protein interactions with drugs. Therefore, AMs were further studied at a higher

concentration (10^{-5} M) in the presence of serum. An overall improvement of oxLDL uptake inhibition potency was observed, suggesting a strong concentration-dependent effect of AMs. Although both M12P5 and T12P5-*meso* were able to significantly lower oxLDL internalization, M12P5 (28%) was twice as efficacious as the less hydrophobic analog T12P5-*meso* (57%), indicating the potential impact of hydrophobicity on enhanced bioactivity under serum-containing conditions. As previously shown by Gao *et al.* [34], increased polymer hydrophobicity leads to increase in both the tendency to form polymeric micellar aggregates and to bind to serum proteins. Given our results, it is plausible that enhanced hydrophobic interactions within the M12P5 micellar core prevents AMs from binding with serum proteins. Meanwhile, T(12-O)P5 was able to effectively impede oxLDL uptake and maintained the nearly basal levels, implying its potential benefits for *in vivo* use. Thus, the structure-activity relationship trends observed in serum-containing conditions parallels those of serum-free conditions except for the role of hydrophobicity.

Lead AMs selected through *in vitro* cell study based on oxLDL uptake inhibitory efficacy, including M12P5, T12P5-*meso*, and T(12-O)P5, were further studied in terms of serum stability, degradation stability, and storage stability for viability as atherosclerotic therapeutic candidates.

2.2.3. Molecular Simulations

To further elucidate the solution behavior as well as biological activity of the AMs, we evaluated the influence of varied structural features on the molecular conformation of the hydrophobic core domains, given that hydrophobic interactions are the main driving force for micellization as well as anti-atherosclerotic bioactivity via enhanced binding with

SRs [33]. We adapted a previously established molecular modeling framework and compared the conformational features and overall molecular architectures of the selected AMs that share the same alkyl arm length but differ with respect to their stereochemistry, linkage (ester vs. ether), and sugar backbone (mucic vs. tartaric acid). Monte Carlo (MC) simulations were performed on model compounds of the five subject AMs to identify the low-energy conformer and calculate selected biophysical properties, i.e., dipole moment, molecular volume (Mol Vol), total surface area (TSA), polar surface area (PSA), non-polar surface area (NPSA), and the average C…C distance between the neighboring alkyl arms ($<C\ldots C>_{avg}$). These values were tabulated for the AMs simulated as both uncharged (**Table 2.2**) and anionic species (**Table 2.3**). Snapshots of the calculated low-energy conformer for each anionic species are presented in **Figure 2.5**.

Some generalizations were established between individual AMs. The calculated dipole moments are far larger in magnitude for the anionic analogs (range 23 –34 Debye) than for their uncharged counterparts (range 2.6 – 4.8 Debye). This finding is a direct consequence of greater polarity of free negative charge on the carboxylate moiety of anionic analogs.

Table 2.2. Summary of selected AMs' biophysical properties calculated as neutral species.

AMs/Property	Dipole (debye)	Molecular volume (Å³)	Molecular area (Å²)	Polar surface area (Å²) [%]	Non-polar surface area(Å²) [%]	$< C\ldots C>_{avg}$ (Å)
M12P5	3.4	1299	1422	152 [10.7]	1270 [89.3]	4.3
T12P5-L	2.95	875	956	122 [12.8]	834 [87.2]	6.2
T12P5-meso	2.89	876	958	120 [12.5]	838 [87.5]	4.3
T(12-O)P5	4.84	798	884	93 [10.5]	791 [89.5]	5
$T(12\text{-}O)P5_{unsat}$	2.62	831	928	104 [11.2]	824 [88.8]	15

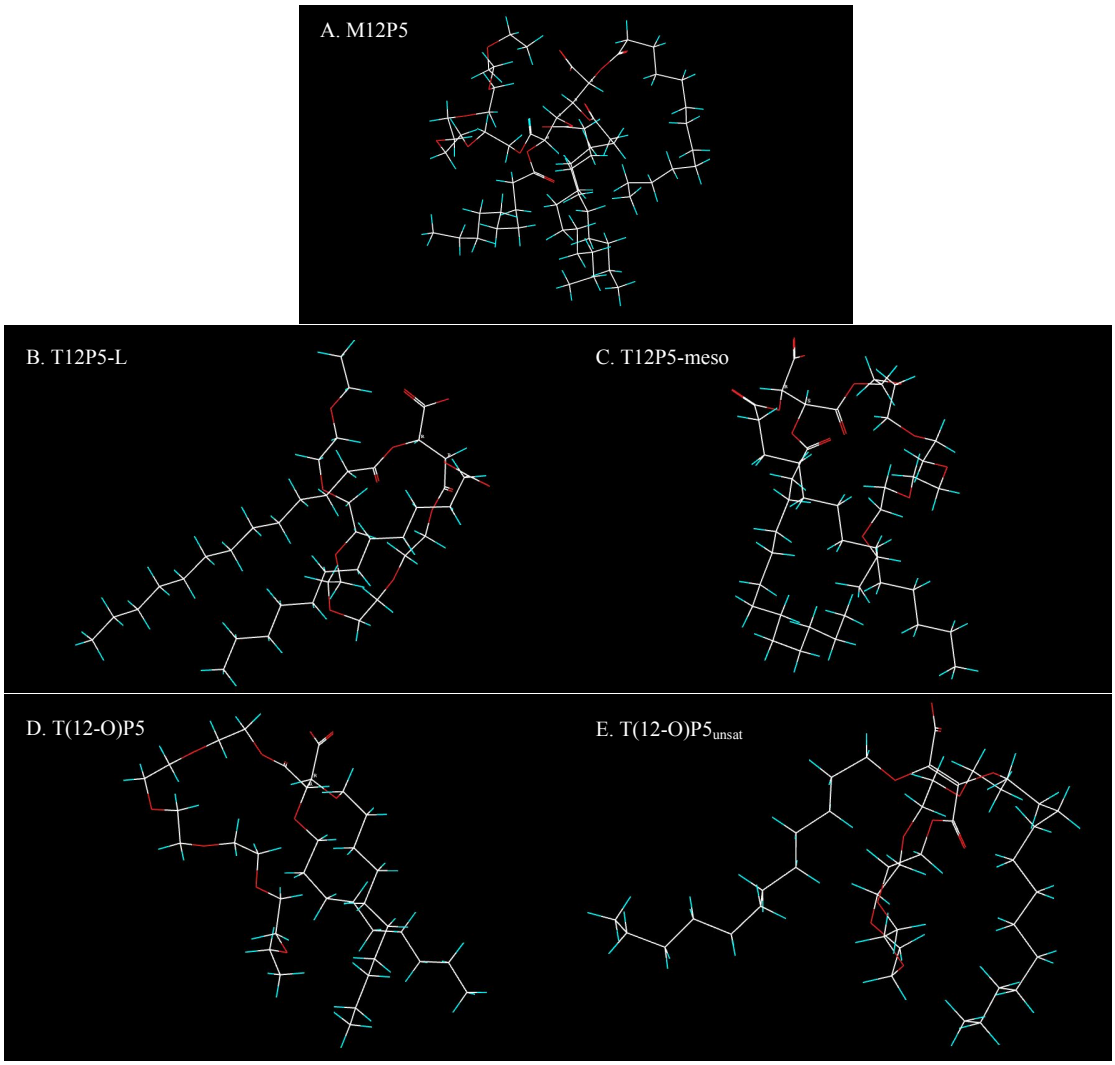

Figure 2.5. Computer snapshots of equilibrium (low-energy) conformer of the AMs as anionic species from MC simulations. Atoms are color-coded: C (white), H (green), O (red). All the structures depicted in the figure are oriented such that their dipole moment is aimed in the vertical direction with the negative pole pointing upward. Inspection of each structure reveals that there is a distinct separation between the hydrophilic groups (carboxyl and PEG) and the hydrophobic arms.

In all cases, except for T(12-O)P5$_{unsat}$, the neighboring alkyl arms are relatively aligned as reflected in the $<C\ldots C>_{avg}$ distance, which ranged from 4.0 Å to 6.2 Å for these

structures. T(12-O)P5$_{unsat}$ did not fit this pattern, with a <C…C>$_{avg}$ distance at 10 – 15 Å. As suggested by the snapshots (**Figure 2.5**E), this high value stems from the *trans* C=C configuration which effectively directs the neighboring alkyl arms in opposite directions. Collectively, the dipole moments of these structures reflect their amphiphilic nature, as the primary driving force for micelle formation.

Table 2.3: Summary of selected AMs' biophysical properties calculated as anionic species.

AMs/Property	Dipole (debye)	Molecular volume (Å^3)	Molecular area (Å^2)	Polar surface area (Å^2) [%]	Non-polar surface area (Å^2) [%]	< C…C>$_{avg}$ (Å)
M12P5	32	1296	1394	147 [10.5]	1247 [89.5]	5.1
T12P5-L	27.2	875	968	122 [12.6]	846 [87.4]	4.0
T12P5-meso	34.2	874	964	122 [12.7]	842 [87.3]	4.5
T(12-O)P5	23.2	742	824	97 [11.8]	727 [88.2]	4.4
T(12-O)P5$_{unsat}$	31.8	829	918	100 [10.9]	818 [89.1]	10.3

The differences in rotational flexibility between the corresponding linkers of the ester-linked T12P5-*L* (27.2 Debye) and the ether-linked T(12-O)P5 (23.2 Debye) result in a clear disparity in dipole moment. The ether linkage is relatively small and flexible, which allows the two alkyl arms to adopt a compact parallel alignment (**Figure 2.5**D), while the ester linkage is rotationally less flexible. Moreover, the ester dipoles adopt an antiparallel orientation that directs the alkyl arms in divergent directions (**Figure 2.5**B). These observations are supported by the CMC values in which better alignment of the ether-linked T(12-O)P5 correlates with a lower CMC value compared to ester-linked T12P5-*L* (**Table 2.1**). As noted above, the low-energy conformer of T(12-O)P5$_{unsat}$ obtained from the molecular simulations features the two alkyl arms pointing in opposite directions. This feature is also quantified by the substantial difference in the <C…C> distance between the

alkyl arms for T(12-O)P5$_{unsat}$ and its flexible analog T(12-O)P5 and as neutral (15 Å vs. 5 Å) or as anionic (10.3 Å vs. 4.4 Å) species. This structural arrangement is not expected to be conducive to micelle stabilization as supported by T(12-O)P5$_{unsat}$'s highest CMC value. M12P5, which has the lowest CMC value among these five AMs (**Table 2.1**), has the highest value of the calculated total surface area and non-polar surface area yet only a moderate dipole moment (32 Debye) as a negatively charged species (**Table 2.3**). The simulation results highlighted the significant influence of minute structural changes of AMs on their corresponding solution properties.

Apart from the aggregation behavior, the 3D molecular modeling also provides invaluable insights into AMs' biological properties. Due to the presence of hydrophobic residues within the SR binding pockets, hydrophobic interaction has been shown to play a crucial role in determining the resultant oxLDL uptake inhibition efficiency. Thus, the superior bioactivity of T(12-O)P5 was likely a result of tightly packed hydrophobic domain as suggested by its small dipole and short $<C\ldots C>_{avg}$ distance. In contrast, T(12-O)P5$_{unat}$ with alkyl arms in opposite directions largely eliminates the potential coordinative effects between arms to enhance binding affinity to SRs, leading to a markedly reduced bioactivity compared to its counterparts.

2.2.4. AM Serum Stability

The integrity of AM micelles upon incubation with serum was examined, providing insights into micelle circulation stability in blood. Here, förster resonance energy transfer (FRET) pair (DiO and DiI) encapsulated micelles were explored to estimate their serum stability. Unlike attaching a fluorophore to polymeric micelles as a marker, which

inevitably alters micelle behavior, using a FRET-based method is a more accurate approach to evaluate micellar integrity without chemically modifying the polymeric structure. When both FRET molecules were loaded inside one micelle and excited at 484 nm, a strong emission of DiI at 565 nm was observed as a result of energy transfer between DiO and DiI. Upon micelle dissociation, the FRET molecules were released and diffused apart, eliminating the energy transfer and leading to a shift of emission peak from 565 (DiI) to 501 nm (DiO). Therefore, micelle disassembly was characterized by the decrease in the FRET ratio ($I_{565}/I_{565}+I_{501}$). Upon complete dissociation, the FRET ratio decreases to approximately 0.6, as a result of background fluorescence. All AM micelles were tested at 0.1 mg/mL, above their respective CMC values.

Phosphate buffered saline (PBS) alone was first added to AM micelles as a control to identify the impact of dilution during the experiment concurrently in addition to protein disruption. Minimal FRET ratio changes were shown for all three AM micelles (**Figure 2.6**), indicating the dilution factor had little, if any, influence on micelle destabilization. This result further validated the benefits of using AMs with low CMC values as carriers. Micelles were then incubated with fetal bovine serum (FBS) at 37 ˚C to represent the physiological conditions. In contrast, a FRET ratio decrease was observed upon incubation with FBS over time in an exponential manner. Due to strong interactions between serum proteins and hydrophobic micellar core, excess serum proteins were determined to be the major factor that led to the micelle disassembly. The FRET ratio underwent a rapid initial decrease, which suggested the fast release of encapsulated FRET molecules from micellar core and finally reached a plateau value as micelles became fully disassembled. The $t_{1/2}$ value is defined as the time required for half of the micelles to disassemble. Because of

the linear correlation between FRET ratio and percentage of disassembled micelles demonstrated by Lu *et al.* previously [21], the $t_{1/2}$ of AM micelles in FBS was estimated as the time required to reach midpoint of the initial FRET ratio and the plateau of the FRET ratio. M12P5 exhibited a $t_{1/2}$ of 30 min, which was much longer than any of the TA-based AMs micelles (≤ 10 min). This effect is likely due to the stronger hydrophobic interaction of M12P5 alkyl arms in the micellar core, withstanding the serum protein-induced micelle destabilization. Although T(12-O)P5 and T12P5-*meso* were similar in hydrophobicity, T(12-O)P5 had a $t_{1/2}$ time slightly longer than T12P5-*meso*.

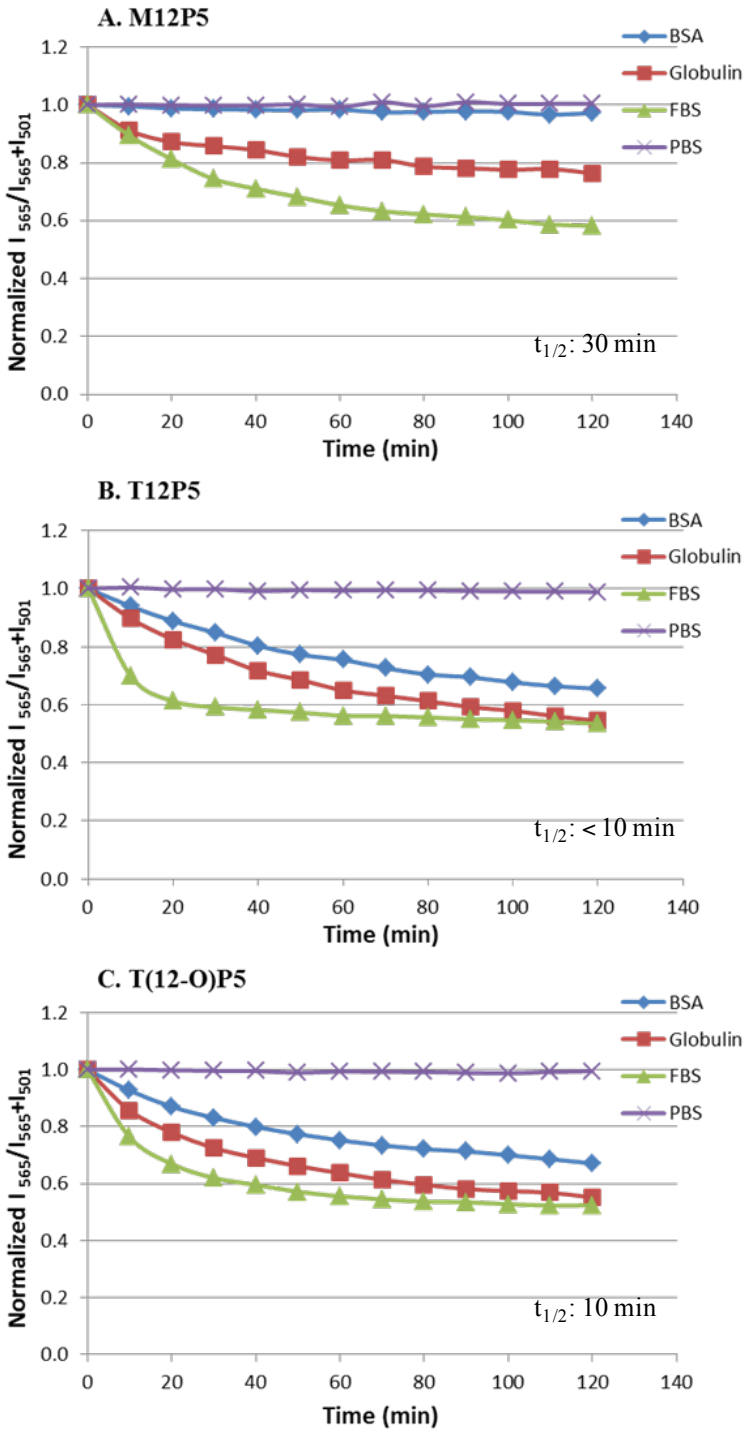

Figure 2.6. Stability of FRET-loaded AM micelles in the presence of FBS is compared to PBS (negative control), BSA, and α and β globulins. Time traces of the FRET ratio,

$I_{565}/(I_{565} + I_{501})$ are normalized to time 0 in solutions. Estimated $t_{1/2}$ is indicated in dashed boxes based on each FBS curve.

To further explore the influence of individual proteins present in serum on micelle integrity, FRET experiments with albumin and α and β globulins were conducted. While albumin was chosen due to its abundance (approximately 60 %) in serum, α and β globulins were chosen based upon their potential to destabilize micelles. The concentrations of serum albumin (45 mg/mL) and α and β globulins (14 mg/mL) in PBS were selected based on average plasma concentrations [35]. M12P5 micelles exhibited robust stability towards albumin disruption during incubation, as only a slight decrease in the FRET ratio was detected. In contrast, the FRET ratio decreased drastically for both T(12-O)P5 and T12P5, suggesting that they were more likely to lose their integrity in the presence of excess albumin (i.e., ~ 40 fold higher molar concentration) compared to M12P5. Incubation with α and β globulins, significantly lowered the FRET ratio of AM micelles to 0.58, 0.53, and 0.52 for M12P5, T12P5, and T(12-O)P5, respectively, over 2 h. The faster FRET ratio decrease compared to albumin conditions indicated that α and β globulins were the primary factors in serum responsible for the rapid compromise of micelle integrity, consistent with observation reported by Diezi *et al* [35].

2.2.5. AM Degradation Stability

Metabolic instability, particularly susceptibility to enzyme-catalyzed degradation, has long been considered a primary factor responsible for the high failure rate of drug candidates translating from *in vitro* work to clinical phase [36]. Previously, we examined

the chemical composition change of AMs upon incubation with lipase solution over 24 h via ^{1}H-NMR. While lauric acid and PEG were detected as degradation products of ester-linked AMs, ether-linked AMs were shown to have intact hydrophobic segment with only PEG cleavage [19]. Herein, we further studied how AM degradation alters their respective bioactivity *in vitro* by treating HMDMs with degraded AMs reconstituted in PBS buffer at predetermined concentrations under serum-free conditions (**Figure 2.7**). Degraded AMs were extracted from degradation media with dichloromethane (DCM) and redissolved in PBS, assuring the complete removal of water soluble lipase, which may influence subsequent oxLDL uptake study.

As shown in **Figure 2.7**, degraded AMs were approximately 3 – 4 fold less efficacious at reducing oxLDL accumulation compared to undegraded AMs at 10^{-6} M. As expected, lipase-catalyzed ester degradation significantly decreased effective AM concentration, leading to compromised efficacy. In fact, minimal residual bioactivity was detected as oxLDL uptake as high as 73% and 88% was observed for the ester-linked AMs, M12P5 and T12P5-*meso*, respectively. It is noteworthy that ether-linked AM T(12-O)P5 was still able to suppress oxLDL uptake levels to as low as 44% after 24 h lipase incubation, which was significantly better than when treated with ester-linked AMs. This phenomenon likely resulted from enhanced metabolic stability conferred by ether linkage as previously discussed [14]. This result further validated the necessity of improving enzymatic degradation stability for enhanced bioactivity *in vivo*. When administered at 10^{-5} M, all AMs remarkably repressed the oxLDL uptake, particularly with T(12-O)P5 to a basal level.

Collectively, these results demonstrate that lipase remarkably compromised AMs' bioactivity and the introduction of ether linkages dramatically improve the degradation

stability of T(12-O)P5, contributing to a potential enhanced anti-atherosclerotic efficacy *in vivo*.

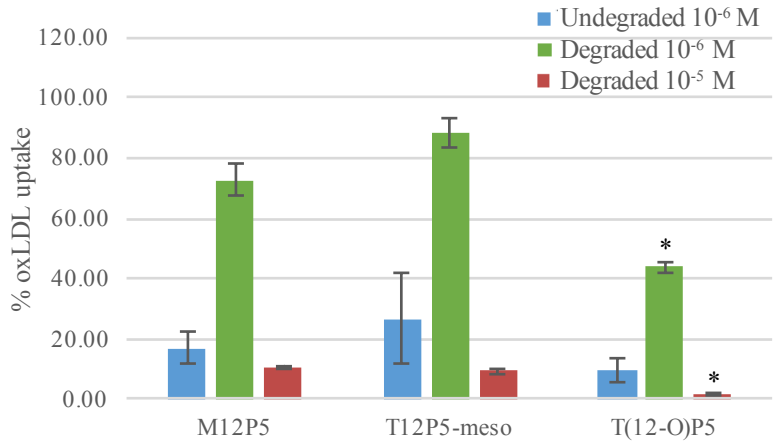

Figure 2.7. OxLDL uptake of HMDMs incubated with lead AMs pretreated with 12 U/mL lipase from porcine pancreas for 24 h in serum-free condition. Single asterisk (*) indicates statistical significance compared to M12P5 and T12P5-*meso* at the same concentration.

2.2.6. AM Storage Stability

Micelle stability at two different storage conditions (25 and 4 ˚C) was evaluated to test the viability of AM micellar assemblies as cardiovascular therapeutic candidates. Despite easy preparation of micellar delivery system compared to other widely used formulations (e.g., liposome, nanoparticle, etc.), micelles are usually prone to aggregation during storage due to their dynamic nature [37].

Upon storage at either room temperature (25 ˚C) or refrigeration (4 ˚C), the colloidal stability of AM micelles was monitored by tracking particle size and size distribution at 10^{-3} M, which is representative of typical storage concentration, by DLS over 2 months (**Figure 2.8**). No precipitation was visually observed for any selected

formulations at either temperature during the monitored period. While T12P5-*meso* and T(12-O)P5 exhibited negligible size changes as well as slight size distribution change, M12P5 maintained a relative constantly size but with large size variations (up to ± 7 nm). Meanwhile, aggregation peaks started to appear above 2000 nm after week 1 and gradually resulted in the reduction of peak intensity (room temperature to 84% and 4 ˚C to 93% by week 8). Overall, these results indicated that both T12P5-*meso* and T(12-O)P5 micelles were physically stable under storage temperatures for at least 2 months.

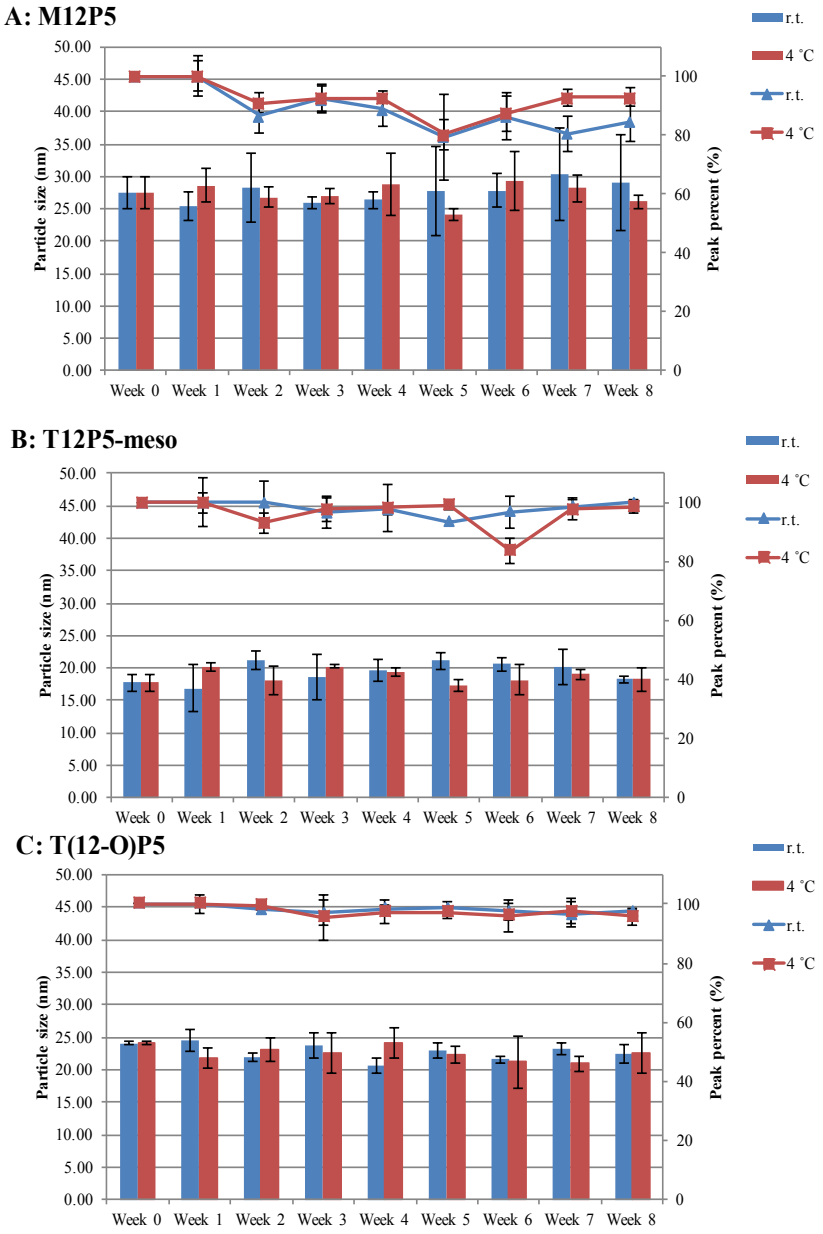

Figure 2.8. Changes in particle size (bar, left y-axis) and size distribution (line, right y-axis) of AM micelles in PBS at room temperature (blue) and 4 ˚C (red) over 2 months.

2.3. Conclusion

Three ester-linked AMs and two ether-linked AMs were synthesized and assessed to reveal their anti-atherosclerotic potency, including oxLDL uptake inhibition, serum

stability, degradation stability, and storage stability. Minor chemical modifications induced significant changes in biological activity as well as physicochemical properties. Specifically, ether linkages between the hydrophobic arms and the sugar backbone dramatically enhanced AM's bioactivity, degradation stability, and storage stability compared to ester linkage. This effect is likely due to the enhanced alignment within the hydrophobic domain, as indicated by 3D modeling results, as well as enhanced metabolic stability. Even though T(12-O)P5 micelles tend to be less stable in the presence of serum, kinetically assembled nanoparticles can be prepared with improved resistance to serum disruption. While lipid-lowering treatments (e.g., statin) are effective when prescribed for treating CVD in the early stages, new therapeutic approaches like targeting SRs may control the progression of the disease. Overall, T(12-O)P5 was synthesized with greatly improved yield and identified as a lead candidate molecule for further *in vivo* evaluation. As enzyme-catalyzed degradation was shown to markedly compromise AM's bioactivity, replacing the ester linkage between the hydrophobic domain and PEG tail with more robust amide linkage, by using amine-terminated PEG, is expected to further improve their efficiency *in vivo*.

2.4. Experimental

2.4.1. Materials

All reagents and solvents were purchased from Sigma-Aldrich (Milwaukee, WI) and were used directly as received unless otherwise noted. Anhydrous dimethylformamide (DMF) was further dried over 4 Å molecular sieves overnight before use. Hydrochloric acid (HCl, 1 N), polytetrafluoroethylene (PTFE) syringe filters, and poly(vinylidene

fluoride) (PVDF) syringe filters were purchased from Fisher Scientific (Fair Lawn, NJ). Di-*tert*-butyl *L*-tartrate [38] and dimethyl amino pyridine p-toluene sulphonate (DPTS) [39] were prepared as previously published. Monomethoxy-poly(ethylene glycol) (PEG, 5 kDa) was azeotropically distilled with toluene (3x 50 mL) prior to use. For cell experiments, reagents include human buffy coats purchased from the Blood Center of New Jersey (East Orange, NJ) and New York Blood Center (Long Island City, NY), 1.077 g/cm^3 Ficoll-Paque Premium purchased from GE Healthcare (Pittsburgh, PA), RPMI 1640 from ATCC (Manassas, VA), macrophage colony stimulating factor (M-CSF) from PeproTech (Rocky Hill, NJ), FBS from Life Technologies (Grand Island, NY), 3,3'-dioctadecyloxacarbocyanine perchlorate (DiO) labeled oxLDL from Kalen Biomedical (Montgomery Village, MD), and unlabeled oxLDL from Biomedical Technologies Inc. (Stoughton, MA).

2.4.2. Characterization

Proton (^{1}H) and carbon (^{13}C) nuclear magnetic resonance (NMR) spectra were acquired on a Varian 400 or 500 MHz spectrophotometer. Samples were dissolved in deuterated chloroform ($CDCl_3$) with trimethylsilane (TMS) as an internal reference. FT-IR spectra were recorded on a Thermo iS 10 FT-IR spectrometer using OMNI software as an average of 32 scans. FT-IR samples were prepared in $CHCl_3$ by solvent casting onto a sodium chloride (NaCl) plate. AMP precursor molecular weights (M_w) were determined by a ThermoQuest Finnigan LCQ-DUO system equipped with a syringe pump, an electrospray ionization (ESI) source, mass spectrometer detector, and the Xcalibur data system. Samples were prepared in spectrophotometric grade methanol (MeOH) at a

concentration of 10 μg/ml. AM weight average M_w and polydispersity indices (PDI) were determined by gel permeation chromatography (GPC) using a Waters LC system (Milford, MA) equipped with a 2414 refractive index detector, 1515 isocratic high performance liquid chromatography (HPLC) pump, 717plus autosampler, and a PLgel MIXED column (Agilent, Santa Clara, CA). Samples were prepared at 10 mg/mL in HPLC grade DCM and filtered through 0.45 μm PTFE syringe filters prior to injection at a flow rate of 1.0 mL/min. Broad molecular weight PEG standards (Waters, Milford, MA) were used for calibration. WaterBreeze v3.20 software was used for data collection and processing.

2.4.3. Synthesis

Amphiphilic polymers M12P5 [18], T12P5-meso [25], and T12P5-(L) [25] were prepared as previously published and discussed. These AM systems are referred to as M12P5 or T12P5, in which M and T denotes mucic acid and tartaric acid, respectively, 12 refers to the number of carbon atoms of each aliphatic chain, P stands for PEG, and 5 indicates molecular weight of the PEG in kDa.

2.4.3.1. Synthesis of T(12-O)P5

DTT(12-O). Di-*tert*-butyl L-tartrate (DTT, 500 mg, 1.91 mmol) was dissolved in 15 mL anhydrous DMF and cooled to 0 ˚C using an ice bath. Sodium hydride (NaH, 160 mg, 4.00 mmol) was added subsequently and the reaction stirred for 20 min. Bromododecane (1.04 mL, 4.19 mmol) was added dropwise to the reaction via syringe pump. The reaction progress was monitored by silica gel thin layer chromatography (hexane: ethyl acetate=85:15). After DTT was completely consumed, the reaction was allowed to stir for an additional 2 h before stopped. The reaction was quenched with

saturated ammonium chloride (NH_4Cl) solution and extracted with ethyl acetate (3x 20 mL). Organic layers were combined, washed with brine (1x 60 mL), and dried over magnesium sulfate ($MgSO_4$) before solvent was removed *in vacuo*. DTT(12-O) was purified on silica gel via column chromatography using a hexane: ethyl acetate gradient (100:0 to 98:2). Yield: 548 mg, 48% (clear, colorless oil). ^{1}H-NMR (400 MHz, $CDCl_3$): 4.16 (s, 2H), 3.72 (m, 2H), 3.30 (m, 2H), 1.60 (m, 4H), 1.49 (s, 18H), 1.24 (b, 36H), 0.88 (t, 6H). ^{13}C-NMR (500 MHz, $CDCl_3$): 169.18, 81.93, 80.69, 72.68, 32.15, 29.87, 29.57, 28.37, 26.25, 22.91, 14.34. IR (cm^{-1}, thin film from $CHCl_3$): 1751 (C=O, ester), 1113 (C-O, ether). ESI-MS m/z: 621.4 $[M+Na]^+$.

T(12-O): DTT(12-O) (247 mg, 0.41 mmol) was dissolved in DCM under argon and cooled to 0 ˚C using an ice bath. TFA (1.26 mL, 16.48 mmol) was then added dropwise via syringe and the reaction was stirred overnight. The reaction mixture was concentrated *in vacuo* and the pure product was precipitated in chilled hexane and collected via vacuum filtration. Yield: 182 mg, 91% (white powder). ^{1}H-NMR (400 MHz, $CDCl_3$): 4.38 (s, 2H), 3.69 (m, 2H), 3.53 (m, 2H), 1.60 (m, 4H), 1.25 (b, 36H), 0.88 (t, 6H). ^{13}C-NMR (500 MHz, $CDCl_3$): 172.49, 79.40, 73.64, 34.20, 31.90, 29.63, 29.61, 29.57, 29.49, 29.35, 29.33, 29.27, 25.72, 22.67, 14.10. IR (cm^{-1}, thin film from $CHCl_3$): 3500-3300 (OH, COOH), 1744 (C=O, COOH), 1165 (C-O, ether). ESI-MS m/z: 485.7 $[M-H]^-$.

T(12-O)P5. Following a published method, T(12-O) (136 mg, 0.28 mmol) and DPTS (24.5 mg, 0.25 mmol) were dissolved in 3 mL anhydrous DCM and 0.2 mL DMF. This solution was added to PEG (467 mg, 0.09 mmol). Once PEG was completely dissolved, *N, N*'-dicyclohexylcarbodiimide (DCC, 1 M in DCM, 0.29 mmol) was added dropwise via syringe and the reaction was stirred under argon. After 48 h, the reaction

mixture was cooled to -20 ˚C to precipitate dicyclohexylurea (DCU) side product which was removed by vacuum filtration. The filtrate was washed with 0.1 N HCl (1x 25 mL) and brine (2x 25 mL). The combined organic layer was dried over $MgSO_4$, and concentrated *in vacuo*. The crude product was purified by precipitation into chilled diethyl ether and isolated via centrifugation (Hettich EBA 12, Beverly, MA; 3500 rpm, 3x 5 min). Yield: 356 mg, 72% (white powder). ^{1}H-NMR (400 MHz, $CDCl_3$): 4.33 (b, 2H), 3.64 (b, ~ 500H), 1.64 (m, 4H), 1.25 (b, 36H), 0.88 (t, 6H). M_w, 5.2 kDa; PDI, 1.1.

2.4.3.2. Synthesis of T(12-O)P5$_{unsat}$

DBT(12-O)$_{unsat}$. Following a modified published procedure [27], a solution of dibenzyl L-tartrate (DBT, 661 mg, 2.00 mmol) and bromododecane (0.99 mL, 4.00 mmol) were dissolved in 10 mL anhydrous diethyl ether. Upon complete dissolution, silver (I) oxide (Ag_2O, 1.07 g, 4.60 mmol) was added and the reaction was refluxed in the dark at 47 ˚C for 72 h. The reaction mixture was filtered through a celite column and washed repeatedly with diethyl ether (3x 10 mL). The combined filtrate was dried over $MgSO_4$, filtered, and pure product was precipitated from chilled hexane and isolated via vacuum filtration. Yield: 611 mg, 46%. ^{1}H-NMR (400 MHz, $CDCl_3$): 7.29 (b, 10H), 5.31 (s, 2H), 4.27 (t, 4H), 1.72 (m, 4H), 1.32 (b, 36H), 0.88 (t, 6H). ^{13}C-NMR (400 MHz, $CDCl_3$): 158.02, 134.46, 129.08, 128.93, 68.70, 67.55, 32.14, 29.83, 29.75, 29.66, 29.56, 29.36, 28.47, 25.90, 22.91, 14.60. IR (cm^{-1}, thin film from $CHCl_3$): 3034 (C-H, Ar), 1743 (C=O, ester), 1260 (C-O, ether). ESI-MS m/z: 687.4 $[M+Na]^+$.

T(12-O)$_{unsat}$. *DBT(12-O)$_{unsat}$* (481 mg, 0.72 mmol) was deprotected in the presence of H_2(g) and 10 wt% palladium on carbon catalyst in anhydrous DCM (8 mL). The reaction was stirred overnight and filtered through a celite column to remove catalyst. The filtrate

was concentrated *in vacuo* and dried over $MgSO_4$. Pure product was precipitated from chilled hexane and collected via vacuum filtration. Yield: 297 mg, 85%. ^{1}H-NMR (500 MHz, $CDCl_3$): 4.28 (t, 4H), 1.75 (m, 4H), 1.38 (m, 4H), 1.26 (b, 32H), 0.88 (t, 6H). ^{13}C-NMR (500 MHz, $CDCl_3$): 157.84, 157.1, 66.29, 30.91, 28.61, 28.54, 28.45, 28.33, 28.14, 27.21, 24.96, 24.65, 21.68, 13.09. IR (cm^{-1}, thin film from $CHCl_3$): IR (cm^{-1}, thin film from $CHCl_3$): 3500-3100 (OH, COOH), 1743 (C=O, COOH), 1260 (C-O, ether). ESI-MS m/z: 483.0 $[M-H]^-$.

T(12-O)P5$_{unsat}$. T(12-O)P5$_{unsat}$ was prepared in a similar manner as previously discussed T(12-O)P5, using T(12-O)$_{unsat}$. Yield: 866mg, 72%. ^{1}H-NMR (400 MHz, $CDCl_3$): 4.43 (t, 2H), 4.28 (t, 2H), 3.64 (b, ~ 500H), 1.73 (m, 4H), 1.26 (b, 36H), 0.88 (t, 6H). M_w, 5.4 kDa; PDI, 1.1.

2.4.4. CMC Measurements

The CMC values of AMs were determined by a pyrene assay as previously described [19]. A stock solution of pyrene was prepared in acetone at $1x10^{-7}$ M, and 0.5 mL of the solution was transferred to a series of vials that were air dried overnight to evaporate the acetone. AMs were dissolved in HPLC grade water at $1x10^{-3}$ M and serial diluted to $1x\ 10^{-4} – 1x10^{-10}$ M concentrations. For each concentration, 5 mL AM solutions was added to the vials with dried pyrene films. Pyrene was allowed to partition into AM micelles by incubation for 48 h at 37 ˚C with gentle agitation (60 RPM). Excitation measurements were performed on a RF-5301PC spectrofluorometer (Shimadzu Scientific Instruments, Columbia, MD) from 300 – 360 nm with 390 nm as the excitation wavelength. The maximum emission wavelength of pyrene shifts from 332 nm to 334.5 nm upon its

partition into micelle's hydrophobic core in the excitation spectrum. The ratio of absorption of pyrene in micelles (334.5 nm) to pyrene alone (332 nm) was plotted against the logarithm of AM concentrations and the inflection of the curve was taken as the CMC.

2.4.5. DLS and Zeta Potential Measurements

DLS and zeta potential analysis were performed using a NanoZS90 instrument (Malvern Instruments, Southboro, MA). Samples were dissolved in HPLC grade water at 2 mg/mL and filtered using 0.45 μm PTFE syringe filters before each measurement. Each sample was run at a 90° scattering angle in triplicate with 30 measurements per run at 25 ˚C. For micelle stability stored at different conditions (4 ˚C and room temperature), AMs were prepared at 10^{-3} M in PBS and sterilized by filtering through a 0.22 μm PVDF sterile syringe filters. The micelle size and distribution were monitored by DLS over 2 months at predetermined time points. All results were presented as mean ± standard deviation around the mean.

2.4.6. Isolation and Culture of Peripheral Blood Mononuclear Cells (PBMCs)

(Performed and written by Qi Li, Rutgers university)

PBMCs were isolated from human buffy coats by Ficoll-Paque (1.077g/cm^3) density gradient. The red blood cell debris of red blood cells after lysing with ammonium-chloride-potassium (ACK) buffer and platelets were removed by centrifugation for 10 min. PBMCs were then washed with PBS and transferred into T175 flasks (BD Falcon, Franklin lakes, NJ) containing 35 mL of base media (RPMI 1640 supplemented with 10% FBS and 1% penicillin/streptomycin). After 24 h incubation at 37 ˚C, adherent monocytes were

selected and differentiated into HMDMs by incubation in base media containing 50 ng/mL M-CSF for 7 days at 37 ˚C. The HMDMs were further plated at a concentration of 50,000 cells/well in 48-well plate for oxLDL uptake experiments.

2.4.7. OxLDL Uptake by Macrophages *(Performed and written by Qi Li, Rutgers university)*

The bioefficacy of AMs (before or after enzyme degradation) was quantified by the inhibition of oxLDL uptake by HMDMs. HMDMs were incubated with unlabeled oxLDL (4 μg/mL) and fluorescent DiO labeled oxLDL (1 μg/mL) with or without AMs (10^{-6} M and 10^{-7} M) in serum-free RPMI 1640 supplemented with 1% penicillin/streptomycin or RPMI 1640 supplemented with 10% FBS, 1% penicillin/streptomycin for 24 h. Treatments were then removed, replaced with cold PBS containing 2mM ethylenediaminetetraacetic acid (EDTA), and placed on ice packs. HMDMs were removed from plates by vigorous pipetting, transferred to 5 mL tubes, centrifuged at 1000 rpm for 10 min, and fixed in 1% paraformaldehyde (150 μL). Uptake of fluorescently labeled oxLDL was quantified using a FACScalibur flow cytometer (Becton Dickinson, Franklin Lakes, NJ) by collecting 10,000 events per sample and analyzed with FlowJo software (Tree Star Inc., Ashland, OR). The quantification of DiO fluorescence is represented by geometric mean fluorescence intensity (MFI). Results represented at least three independent experimental replicates. The bioefficacy of AMs is presented by % oxLDL uptake, which was calculated using the following formula:

$$\%\ \text{oxLDL uptake} = 100 * \frac{MFI\ of\ AM\ containing\ condition}{MFI\ of\ oxLDL\ control}$$

2.4.8. Molecular Simulations *(Performed and written by Prof. William Welsh, Rutgers university)*

Molecular modeling calculations were performed on ester- and ether-linked AMP model compounds to evaluate similarities and differences in conformational preferences. All operations were conducted using the Spartan'08 *molecular modeling software suite (Version 4.0.0, Wavefunction, Inc., Irvine, CA). A total of five structures were constructed and explored, representing model compounds for the respective ester- and ether-based AMs. For each model compound, simulations were performed on the neutral (-COOH) and anionic ($-COO^-$) species. The anionic form depicts the putative state that would exist under physiological pH conditions (pH 7.4). The only structural modification for each compound was a truncated PEG domain to five ethylene oxide [$-O-CH_2-CH_2-$] units capped by an ethoxy [$-O-CH_2-CH_3$] terminal group. Preliminary calculations in which more PEG repeat units were added revealed insignificant impact on our findings (not shown) and, conversely, limited the number of physically meaningful conformers generated in conformational searches. Molecular mechanics calculations were carried out using the Merck Molecular Force Field (MMFF) in an aqueous environment represented by the SM5.4 solvent model (MMFFaq). A stochastic search of conformational space was implemented on each molecule using a MC procedure that generated 20,000 independent conformers, from which the equilibrium (lowest energy) conformers were selected for subsequent visual inspection. This MC scheme employed a simulated annealing algorithm that searched for the global low-energy conformer by biased sampling of low-energy conformers and high-energy conformers over the course of a step-wise descending temperature gradient.*

2.4.9. FRET Pair Molecules Encapsulation

FRET pair containing micelles were prepared by the precipitation and membrane dialysis method [21]. AMPs (5 mg), 1,1'-dioctadecyl-3,3,3',3'-tetramethylindocarbocyanine perchlorate (DiI, 25 μg), and DiO (25 μg) were dissolved in 0.5 mL DMF and then diluted with 0.5 mL HPLC grade water. The solution was then dialyzed (Spectra/Por MWCO 3500) against 2 L distilled water for 2 days, where the water was changed every 2 h for the first 6 h. The micelle solution was filtered through a 0.45 μm PTFE syringe filters before use to remove minimal amount of unloaded FRET molecules.

2.4.10. FRET Fluorescence Spectroscopy

The fluorescence spectra of FRET experiments were performed on a RF-5301PC spectrofluorometer (Shimadzu Scientific Instruments, Columbia, MD) at an excitation wavelength of 484 nm, and the slit widths of excitation and emission were all fixed at 1.5 nm. Emission spectra were recorded from 490 to 590 nm.

The stability of AM micelles (0.1 mg/mL) was studied in the presence of individual serum proteins and FBS at 37 °C. The concentrations of serum proteins tested were 45 mg/mL for albumin and 14 mg/mL for α and β globulins in PBS. Micelles were also diluted with PBS as a control to study the influence of dilution on micelle integrity. Time-resolved spectra were collected with an excitation wavelength at 484 nm and FRET ratio ($I_{565}/I_{565}+I_{501}$), where I_{565} and I_{501} are the fluorescence wavelength intensities of DiI and

DiO, respectively, was calculated to monitor the disassociation of micelles every 10 min for 120 min [21].

2.4.11. Lipase Degradation of AMs

AMs were dissolved in PBS (pH=7.4) at $1x10^{-3}$ M and mixed with suspension of porcine pancreatic lipase at a final concentration of 12 U/mL. The solutions were then incubated at 37 °C with gentle agitation (60 rpm) for 24 h. The degradation media was extracted with DCM (3x 10 mL) and solvent was removed *in vacuo*. AM degradation products were redissolved in PBS for subsequent studies of oxLDL uptake in cells.

2.4.12. Statistical Analysis

All experiments were repeated in triplicate. OxLDL uptake results were analyzed by pairwise comparison with Dunnett's post hoc test using JMP® statistical software (SAS Institute Inc., Cary, NC). Significance criteria assumed a 95% confidence level ($p < 0.05$). Standard deviation is reported in the form of error bars.

2.5. References

[1] Mozaffarian D, Benjamin EJ, Go AS, Arnett DK, Blaha MJ, Cushman M, et al. Heart disease and stroke statistics-2015 update: a report from the american heart association. Circulation. 2015;131:e29.

[2] Chnari E, Lari HB, Tian L, Uhrich KE, Moghe PV. Nanoscale anionic macromolecules for selective retention of low-density lipoproteins. Biomaterials. 2005;26:3749-58.

[3] Patel RP, Moellering D, Murphy-Ullrich J, Jo H, Beckman JS, Darley-Usmar VM. Cell signaling by reactive nitrogen and oxygen species in atherosclerosis. Free Radical Biology and Medicine. 2000;28:1780-94.

[4] Chnari E, Nikitczuk JS, Uhrich KE, Moghe PV. Nanoscale Anionic Macromolecules Can Inhibit Cellular Uptake of Differentially Oxidized LDL. Biomacromolecules. 2006;7:597-603.

[5] Stroes E. Statins and LDL‐cholesterol lowering: an overview. Current Medical Research and Opinion. 2005;21:S9-S16.

[6] Staels B, Dallongeville J, Auwerx J, Schoonjans K, Leitersdorf E, Fruchart J-C. Mechanism of Action of Fibrates on Lipid and Lipoprotein Metabolism. Circulation. 1998;98:2088-93.

[7] Golomb BA, Evans MA. Statin Adverse Effects: A Review of the Literature and Evidence for a Mitochondrial Mechanism. American journal of cardiovascular drugs : drugs, devices, and other interventions. 2008;8:373-418.

[8] Elisaf M, Florentin M, Liberopoulos E, Mikhailidis D. Fibrate-associated adverse effects beyond muscle and liver toxicity. Current pharmaceutical design. 2008;14:574-87.

[9] Jamkhande PG, Chandak PG, Dhawale SC, Barde SR, Tidke PS, Sakhare RS. Therapeutic approaches to drug targets in atherosclerosis. Saudi Pharmaceutical Journal. 2014;22:179-90.

[10] Moore KJ, Freeman MW. Scavenger Receptors in Atherosclerosis: Beyond Lipid Uptake. Arteriosclerosis, Thrombosis, and Vascular Biology. 2006;26:1702-11.

[11] Boullier A, Bird DA, Chang M-K, Dennis EA, Friedman P, Gillotte-Taylor K, et al. Scavenger Receptors, Oxidized LDL, and Atherosclerosis. Annals of the New York Academy of Sciences. 2001;947:214-23.

[12] Babaev VR, Gleaves LA, Carter KJ, Suzuki H, Kodama T, Fazio S, et al. Reduced Atherosclerotic Lesions in Mice Deficient for Total or Macrophage-Specific Expression of Scavenger Receptor-A. Arteriosclerosis, Thrombosis, and Vascular Biology. 2000;20:2593-9.

[13] Febbraio M, Podrez EA, Smith JD, Hajjar DP, Hazen SL, Hoff HF, et al. Targeted disruption of the class B scavenger receptor CD36 protects against atherosclerotic lesion development in mice. The Journal of Clinical Investigation. 2000;105:1049-56.

[14] Abdelhamid DS, Zhang Y, Lewis DR, Moghe PV, Welsh WJ, Uhrich KE. Tartaric acid-based amphiphilic macromolecules with ether linkages exhibit enhanced repression of oxidized low density lipoprotein uptake. Biomaterials. 2015;53:32-9.

[15] Gu L, Faig A, Abdelhamid D, Uhrich K. Sugar-Based Amphiphilic Polymers for Biomedical Applications: From Nanocarriers to Therapeutics. Accounts of chemical research. 2014;47:2867-77.

[16] Wang J, Plourde NM, Iverson N, Moghe PV, Uhrich KE. Nanoscale amphiphilic macromolecules as lipoprotein inhibitors: the role of charge and architecture. International Journal of Nanomedicine. 2007;2:697-705.

[17] Chnari E, Nikitczuk JS, Wang J, Uhrich KE, Moghe PV. Engineered Polymeric Nanoparticles for Receptor-Targeted Blockage of Oxidized Low Density Lipoprotein Uptake and Atherogenesis in Macrophages. Biomacromolecules. 2006;7:1796-805.

[18] Tian L, Yam L, Zhou N, Tat H, Uhrich KE. Amphiphilic Scorpion-like Macromolecules: Design, Synthesis, and Characterization. Macromolecules. 2004;37:538-43.

[19] Abdelhamid D, Arslan H, Zhang Y, Uhrich KE. Role of branching of hydrophilic domain on physicochemical properties of amphiphilic macromolecules. Polymer Chemistry. 2014;5:1457-62.

[20] Miller T, Rachel R, Besheer A, Uezguen S, Weigandt M, Goepferich A. Comparative Investigations on In Vitro Serum Stability of Polymeric Micelle Formulations. Pharm Res. 2012;29:448-59.

[21] Lu J, Owen SC, Shoichet MS. Stability of Self-Assembled Polymeric Micelles in Serum. Macromolecules. 2011;44:6002-8.

[22] Kim S, Shi Y, Kim JY, Park K, Cheng J-X. Overcoming the barriers in micellar drug delivery: loading efficiency, in vivo stability, and micelle–cell interaction. Expert Opinion on Drug Delivery. 2009;7:49-62.

[23] Iverson NM, Sparks SM, Demirdirek B, Uhrich KE, Moghe PV. Controllable inhibition of cellular uptake of oxidized low-density lipoprotein: Structure–function relationships for nanoscale amphiphilic polymers. Acta Biomaterialia. 2010;6:3081-91.

[24] Azevedo HS, Reis RL. Understanding the enzymatic degradation of biodegradable polymers and strategies to control their degradation rate. Biodegradable systems in tissue engineering and regenerative medicine Boca Raton, FL: CRC Press. 2005;177201.

[25] Poree DE, Zablocki K, Faig A, Moghe PV, Uhrich KE. Nanoscale Amphiphilic Macromolecules with Variable Lipophilicity and Stereochemistry Modulate Inhibition of Oxidized Low-Density Lipoprotein Uptake. Biomacromolecules. 2013;14:2463-9.

[26] Hehir S, Plourde NM, Gu L, Poree DE, Welsh WJ, Moghe PV, et al. Carbohydrate composition of amphiphilic macromolecules influences physicochemical properties and binding to atherogenic scavenger receptor A. Acta Biomaterialia. 2012;8:3956-62.

[27] Aurich HG, Biesemeier F. Intramolecular 1, 3-Dipolar cycloaddition of transient enantiomerically pure oxaalkenyl nitrones. Synthesis. 1995:1171-8.

[28] Iyer MR, Trivedi GK. Silver(I) Oxide Catalyzed Oxidation of o-Allyl- and o-(1-Propenyl)phenols. Bulletin of the Chemical Society of Japan. 1992;65:1662-4.

[29] Olsen SN, Andersen KB, Randolph TW, Carpenter JF, Westh P. Role of electrostatic repulsion on colloidal stability of Bacillus halmapalus alpha-amylase. Biochimica et Biophysica Acta (BBA) - Proteins and Proteomics. 2009;1794:1058-65.

[30] Israelachvili J, Pashley R. The hydrophobic interaction is long range, decaying exponentially with distance. Nature. 1982;300:341-2.

[31] Samith VD, Miño G, Ramos-Moore E, Arancibia-Miranda N. Effects of pluronic F68 micellization on the viability of neuronal cells in culture. Journal of Applied Polymer Science. 2013;130:2159-64.

[32] Alexandridis P, Holzwarth JF, Hatton TA. Micellization of Poly(ethylene oxide)-Poly(propylene oxide)-Poly(ethylene oxide) Triblock Copolymers in Aqueous Solutions: Thermodynamics of Copolymer Association. Macromolecules. 1994;27:2414-25.

[33] Faig A, Petersen LK, Moghe PV, Uhrich KE. Impact of Hydrophobic Chain Composition on Amphiphilic Macromolecule Antiatherogenic Bioactivity. Biomacromolecules. 2014;15:3328-37.

[34] Gao JY, Dubin PL. Binding of proteins to copolymers of varying hydrophobicity. Biopolymers. 1999;49:185-93.

[35] Diezi TA, Bae Y, Kwon GS. Enhanced Stability of PEG-block-poly(N-hexyl stearate l-aspartamide) Micelles in the Presence of Serum Proteins. Molecular Pharmaceutics. 2010;7:1355-60.

[36] Nassar A-EF, Kamel AM, Clarimont C. Improving the decision-making process in the structural modification of drug candidates: enhancing metabolic stability. Drug Discovery Today. 2004;9:1020-8.

[37] Musacchio T, Laquintana V, Latrofa A, Trapani G, Torchilin VP. PEG-PE micelles loaded with paclitaxel and surface-modified by a PBR-ligand: synergistic anticancer effect. Molecular pharmaceutics. 2009;6:468-79.

[38] Uray G, Lindner W. tert-butyl esters and ethers of (R,R)-tartaric acid. Tetrahedron. 1988;44:4357-62.

[39] Moore JS, Stupp SI. Room temperature polyesterification. Macromolecules. 1990;23:65-70.

3. Cationic Amphiphiles as Antimicrobial Peptide Mimics

[This work in under review for publication in Nanomedicine: Nanotechnology, Biology and Medicine under the title "Self-assembled Cationic Amphiphiles as Antimicrobial Peptides Mimics: Role of Hydrophobicity, Linkage Type, and Assembly State". Ammar Algburi, Ning Wang, Vladyslav Kholodovych, Drym O. Oh, Michael Chikindas, and Kathryn E. Uhrich are co-authors for this work.]

3.1. Introduction

Using antimicrobials for control of infectious diseases has been a common practice since the 1940s [1]. However, the emergence of multidrug-resistant bacteria due to overuse and misuse of antimicrobial agents has become a severe threat to public health [2]. Compared to conventional antibiotics which target a specific biochemical process (e.g., DNA synthesis, protein synthesis) or molecule (e.g., enzyme), naturally occurring antimicrobial peptides (AMPs), as part of innate immune defense, have received substantial interest owing to their broad-spectrum activities, minimum cytotoxicity, and unique cellular membrane targeting mechanism [3]. This mode of action reduces the tendency of resistance development from genetic mutation; thus, AMPs hold great potential for treating microbial infections as antibiotics alternatives [4-6].

Despite diverse primary peptide sequences and secondary structures displayed by AMPs, many share two characteristics that result in their amphiphilic topology: cationic residues and hydrophobic domains [4]. Recent literature results suggest that the biological activities of AMPs mainly depend on their physicochemical properties rather than specific amino acid sequences [4, 7]. The cationic charges are essential to promote electrostatic interactions with negatively charged bacterial membranes [8], while

hydrophobic residues aid in subsequent insertion into the hydrophobic core of the membranes, leading to membrane disruption, leakage of the cytoplasm, and eventual cell death [9]. However, intrinsic drawbacks are associated with AMPs, including low metabolic stability (i.e., susceptibility to proteolysis) [10], high manufacture cost, and formulation difficulties; these limitations have precluded their translational into clinical settings [4].

Inspired by natural AMPs, a variety of structurally diverse synthetic mimics with key physicochemical natures (i.e., cationic charges and amphiphilicity) have been synthesized and investigated, such as peptidomimetics [11, 12], polymers (e.g., cationic derivatives of polyacrylate [13], polynorbornene [14], polyarylamide [15]), and oligomers [16]. Although these synthetic analogues are relatively facile and inexpensive to prepare in large quantities, obtaining potent antimicrobial activity while retaining high selectivity towards microbes (i.e., minimum toxicity towards mammalian cells) remains a challenge [15].

As the facially amphiphilic conformation has been demonstrated to be a key factor in AMPs' selective potent antimicrobial activity towards bacterial cells with minimal toxicity towards mammalian cells [17-19], we designed cationic amphiphiles (CAms) with similar spatial arrangements in which hydrophilic and hydrophobic residues of AMPs segregate to opposing domains [13]. Two series of biscationic compounds, ether- and ester-linked CAms, were synthesized with tartaric acid backbones and flexible spacers between the cationic charges and the backbone (**Figure 3.1**), which allowed the hydrophilic ammonium moieties and hydrophobic alkyl arms to be folded on opposite faces of the backbone. The hydrocarbon arms were conjugated to the backbone via ether

or ester linkages, enabling the exploration of side chain orientation influence on CAms' biophysical properties, which has not been fully established. We hypothesized that the variation in linkage flexibility would affect the conformation of CAms, leading to differential membrane-CAm interactions [20]. While increasing hydrophobicity may elicit an increase in antimicrobial potency [21], undesirable increases in hemolytic and cytotoxic activities have also been reported [16, 22]. Thus, the hydrophobicity of CAms was systematically tuned by varying hydrocarbon arm lengths to achieve potent bacterial membrane-lysing activity while mitigating adverse effects.

Upon successful synthesis, CAms were observed to readily self-assemble into different nanostructures in aqueous solutions. Their antimicrobial activity was then evaluated against a panel of microbes, including both Gram-positive and Gram-negative bacteria. The observed structure-activity relationship correlated specific design parameters with antimicrobial efficacy as well as toxicity towards mammalian cells. Their postulated membrane-lytic mechanism was examined via microscopy techniques and molecular dynamics (MD) simulations were employed to ascertain CAm-membrane interactions on molecular level.

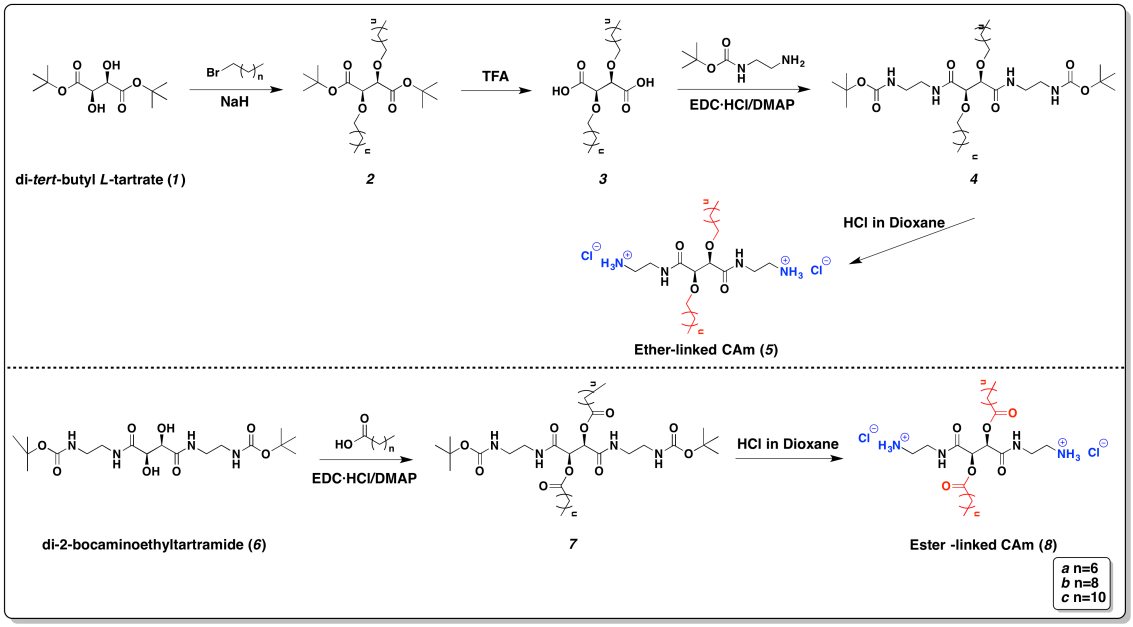

Figure 3.1. Syntheses of ether- and ester-linked CAms ***5*** and ***8***.

3.2. Results and Discussion

3.2.1. Synthesis and Characterization of CAms

As hydrophobicity is a key design parameter that can be tuned to obtain balance between antimicrobial activity and selectivity [22, 23], two series of CAms with ester and ether linkages were synthesized with different hydrocarbon lengths (**Figure 3.1**). In previous work (Chapter 2), we demonstrated that the replacement of ester linkages with more flexible ether linkages in amphiphilic polymers dramatically affected their self-assembling behavior and molecular conformation, and ultimately changed their biological activities [24]. Thus the linkage type was also varied in this study, presumably altering physicochemical and biological activities of CAms.

Ether-linked CAms were first synthesized by alkylating di-*tert*-butyl *L*-tartrate (***1***) with bromoalkane through a nucleophilic substitution reaction and subsequently using

trifluoroacetic acid (TFA) to deprotect the *tert*-butyl groups. The robust stability of *tert*-butyl groups of in the presence of base allowed high alkylation yields (~ 50 – 60%) compared to other protecting groups such as benzyl groups (~ 10%) [20]. *N-Boc*-ethylenediamine was then incorporated to the resulting diacid (***3***) via carbodiimide coupling to generate CAm precursors (***4***). Following successful conjugation, ***4*** was deprotected using HCl in dioxane to afford the final product (***5***) as chloride salt with quantitative yields. The successful synthesis of all intermediates and *CAms* was confirmed by nuclear magnetic resonance (NMR), fourier transform infrared (FT-IR) spectroscopies, and mass spectrometry.

Similarly, a series of CAms with ester linkages between the hydrophobic arms and tartaric acid backbone was synthesized with analogous molecular weights, cationic net charge, and hydrophobicity (i.e., carbon numbers). Instead of alkylation, carbodiimide coupling was carried out with di-2-bocaminoethyltartramide and alkanoic acids followed by acid-catalyzed deprotection to afford ***8***. The chemical structures of all amphiphiles and intermediates were confirmed as described above for the ether-linked CAms.

3.2.2. Self-assembly of CAms

Dong *et al.* reported substantially different biological profiles for fibrous cationic peptides and monomeric peptides, indicating the potential influence of assembling state on bioactivity [11, 25]. To establish the relationship between supramolecular structures and antimicrobial potency, the aggregation behavior of CAms was carefully evaluated (**Table 3.1**). In water, all CAms (with the exception of ***5a*** and ***8a***) readily self-assembled into supramolecular nanostructures at their respective critical micelle concentrations

(CMCs), ranging from 4 to 110 μg/mL. No stable self-assembled structures were observed for ***5a*** or ***8a***, which had hydrophobic arms of only eight carbons, even at concentrations as high as 1 mg/mL; thus, these two compounds were not further investigated. This significant CMC increase is likely caused by the relatively weak hydrophobic interactions imposed by the short alkyl arms which can no longer effectively overcome the strong electrostatic repulsion from the cationic head groups [26]. As expected, CMC values are dependent on the hydrophobicity of the alkyl arms, with increased hydrophobicity (from alkyl arm ***c*** to ***a***) giving sequentially lower CMC values [27]. The CMC discrepancy between the ether- and ester-linked series was appreciable, despite differing only by the linkage type. In comparing ***8*** to their respective ether counterparts (***5)***, all ester-linked CAms exhibited CMC values approximately 4 – 5 fold lower than their analogous ether-linked CAms, indicating their higher propensity to remain in an assembled state upon dilution.

Table 3.1. Physicochemical and self-assembly properties of CAms.

CAm	CMC[a]		Hydrodynamic Size[a]	Zeta Potential[a]
	(μg/mL)	(mmol/L)	(nm)	(mV)
5a	> 1000	> 1.88	n.a.	n.a.
5b	110	0.187	53.7 ± 3.0	21.3 ± 1.3
5c	14	0.022	71.4 ± 1.8	36.1 ± 1.6
8a	> 1000	> 1.78	n.a.	n.a.
8b	22	0.035	73.2 ± 0.2	32.6 ± 0.8
8c	4	0.006	104.9 ± 0.4	44.8 ± 2.7

[a] Measured at 1 mg/mL in deionized (DI) water at 25 ˚C.

The micelle sizes were then determined by dynamic light scattering (DLS) at 1 mg/mL while overall net charges characterized by zeta potential. All materials were

observed to self-assemble into micelles with sizes between 50 – 100 nm with positive potentials ranging from 21 to 45 mV, allowing efficient electrostatic interactions with anionic bacterial cell membranes. The morphology of micelles was examined via TEM, and indicated that spherical micelles were spontaneously formed (**Figure 3.1**).

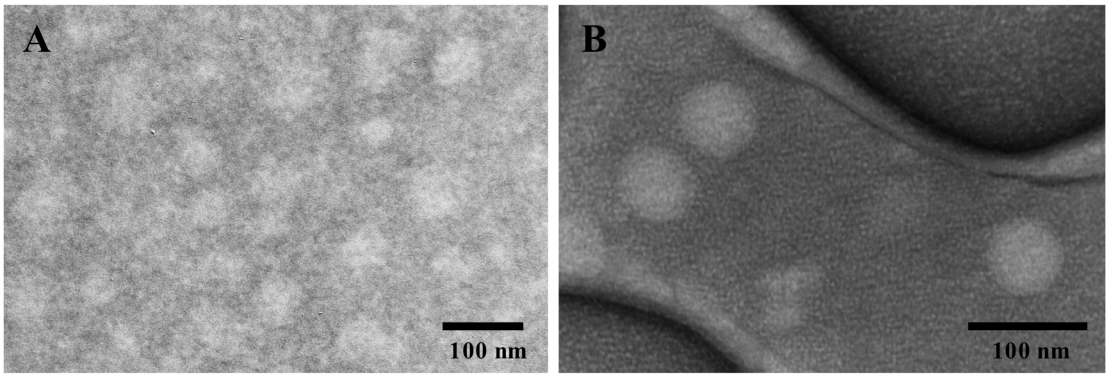

Figure 3.2. TEM images of representative supramolecular nanostructures formed by CAms ***5b*** (A) and ***8b*** (B) upon direct dissolution in water.

3.2.3. Antimicrobial Activity

CAms were subsequently evaluated against five selected pathogenic microorganisms, including Gram-positive bacteria (i.e., *S. aureus* and *L. monocytogenes*) and Gram-negative bacteria (i.e., *E. coli*, *S. typhimurium*, and *P. aeruginosa*), using a turbidity-based microdilution method. Minimum inhibitory concentrations (MICs) were taken as the lowest concentrations that completely inhibited bacteria growth. As shown in **Table 3.2**, CAms showed antimicrobial activity against a panel of Gram-positive and Gram-negative bacteria, similar to the broad-spectrum properties of AMPs. In addition, the CAms were biologically more active against Gram-positive bacteria than Gram-negative bacteria with the MIC values being 2 to 4-fold lower. Higher MIC values of

Gram-negative bacteria could be attributed to the presence of an additional lipopolysaccharide layer, which forms a hydrophilic barrier preventing highly hydrophobic CAms from penetrating the membrane.

In comparing amphiphiles' antibacterial activity, it became apparent that hydrophobicity, varied by alkyl chain length, significantly modulated their potency. Notably, the most hydrophobic CAms with longest alkyl chains (***5c*** and ***8c***), did not show appreciable antimicrobial activity at even the highest concentration (250 μg/mL) tested. However, CAms with shorter alkyl lengths demonstrated remarkably enhanced antimicrobial efficiency. In particular, ***5b*** and ***8b***, with intermediate arm length, demonstrated the most superior antimicrobial activity with MIC values as low as 0.95 and 3.9 μg/mL for Gram-positive and Gram-negative bacteria, respectively. These values are amongst the lowest reported MIC values in the literature. Given that a sufficient degree of hydrophobicity in the arms is likely required to promote intercalation and disruption of the bacterial membranes, these results indicated that a "sweet spot" in hydrophobicity was attained and conferred optimal bioactivity [16, 22]. Notably, the MICs of all CAms are far below their respective CMC values, suggesting that it is the monomeric CAms rather than the corresponding self-assembled, micellar structures that enable the bioactivity. It is plausible that the stable nanostructures formed by ***5c*** and ***8c*** largely limit the interaction between the individual molecules and bacteria, which remarkably diminishes their affinity to bacterial membranes [22, 28, 29]. This observation is consistent with the findings by Dong *et al.* whereby increased supramolecular order compromised the antimicrobial activity of multidomain peptides [25].

Overall, CAms with ether linkages (***5***) exhibited greater antimicrobial efficacy than ester-linked counterparts (***8***). The disparity in antimicrobial activity between the two series likely stems from the presence of the carbonyl functionality in the hydrophobic domains of ***8***, which limits the rotational flexibility of alkyl arms, and potentially leads to a more rigid molecular conformation/folding. We speculate that the flexible conformation increases the propensity of the hydrophobic chains to embed into and disintegrate the hydrophobic regions of lipid membranes; this speculation was studied further via MD simulation and will be discussed in section **3.2.6** below.

Table 3.2. Antimicrobial and hemolytic activities of CAms.

CAm	MIC (μg/mL)					HC_{50}[a] (μg/mL)	SI[b]	
	S. aureus (G+)	*L. monocytogenes* (G+)	*E. coli* (G-)	*S. typhimurium* (G-)	*P. aeruginosa* (G-)		G+	G-
5a	3.9	3.9	15.6	7.8	3.9	47	12	3
5b	0.95	0.95	3.9	3.9	3.9	65	68	17
5c	3.9	125	> 250	> 250	> 250	> 250	> 64	n.a.
8a	31.2	31.2	62.5	62.5	31.2	139	4	2
8b	1.9	1.9	3.9	3.9	3.9	81	43	11
8c	15.6	> 250	> 250	> 250	> 250	> 250	> 16	n.a.

[a] Concentration required to induce 50% leakage of hemoglobin from human red blood cells (hRBCs). [b] Selectivity index (SI) was determined as HC_{50}/MIC using *S. aureus* and *E. coli* as representatives for SI of G+ and G- calculations respectively.

Taken together, the two lead antimicrobials ***5b*** and ***8b*** displayed broad-spectrum and potent antimicrobial activity. Hydrophobicity is necessary but not sufficient to dictate CAm's biological activity, as molecular conformation and assembly state also play important roles in their behaviors.

3.2.4. Cell Compatibility

Hemolytic activity is an important factor to be considered for antimicrobial therapy development. A hemolysis assay was conducted by incubating hRBC with CAms at various concentrations and the leakage of hemoglobin was quantified by UV spectroscopy at 541 nm. In general, all CAms induced negligible hemolysis at their respective MICs (**Figure 3.2**), though the ether series displayed higher selectivity indices (SI) towards bacterial cells over mammalian cells. The primary phospholipids in the outer leaflet of mammalian cell membranes are zwitterionic PC (phosphatidylcholine) lipids while anionic PG (phosphatidylglycerol) lipids are rich in bacterial membranes [30]. The difference in membrane composition between bacteria and mammalian cells may account for the specificity and selectivity, which was supported by MD simulation results discussed further in section **3.2.6**.

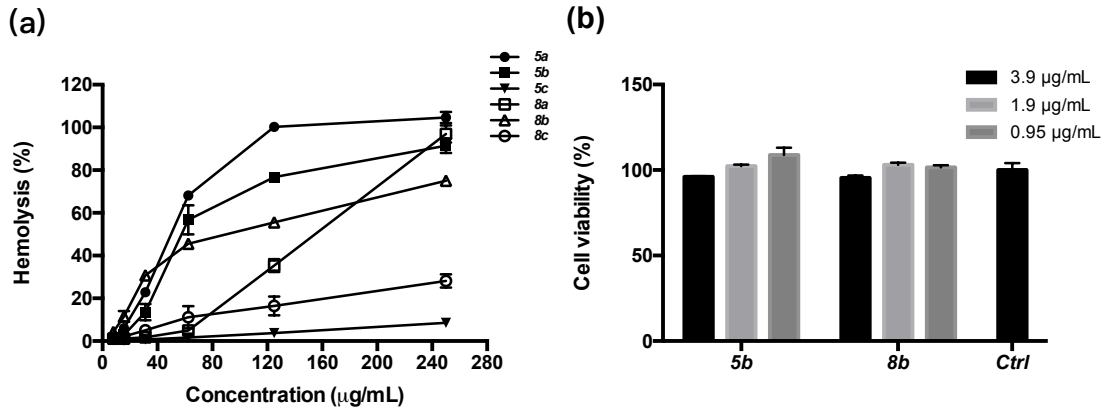

Figure 3.3. Hemolytic activities of CAms at varied concentrations (a), and cytotoxicity of leading compounds ***5b*** and ***8b*** assessed by (3-(4,5-dimethylthiazol-2-yl)-2,5-diphenyltetrazolium bromide) (MTT) assay (b) compared to medium only controls.

No linear dependence on hydrophobicity was observed for HC_{50} of CAms. This result is surprising, considering that increased hydrophobicity has been correlated to stronger hemolytic activity [21]. On the contrary, similarities in relation to the measured MICs were observed for the results (**Table 3.2**). For example, while ***5c*** and ***8c*** induced the lowest hemolytic response (HC_{50} >250 μg/mL), they are weak antimicrobials, revealing low overall membrane activity. The trend again suggests that the molecular conformation and self-assembled state are key factors in determining the CAm-membrane interactions in addition to the hydrophobicity. The CAms ***5a*** and ***8a*** with a side-chain length of eight carbons demonstrated sufficiently high HC_{50} values (47 and 139 μg/mL) but with moderate selectivity (i.e., 2-12 fold). In particular, the lead antimicrobial agents ***5b*** and ***8b*** preferentially interacted with bacterial cells and exhibited the highest selectivity, indicating their promise as AMP mimics. Compound ***5b*** showed slightly better performance compared to its ester analog ***8b***, with SI as high as 68 for Gram-positive bacteria and 17 for Gram-negative bacteria as opposed to SI values of 43 and 11, which is highly desirable for practical infection treatment.

To further examine the cytocompatibility of lead CAms, cytotoxicity was determined after co-incubation with human fibroblasts cells for prolonged time (24 h) at MICs, followed by quantification of cell viability with the MTT assay. Compounds ***5b*** and ***8b*** did not induce any pronounced cytotoxicity to cells at concentrations sufficient to inhibit microbial growth.

The lead antimicrobial ***5b***, which exerted the most potent antimicrobial activity while having the highest selectivity, was selected for further mechanistic study.

3.2.5. Mechanism of Action

The bacterial cell membrane is involved in many essential functions: protection, transport, osmoregulation, respiration processes, biosynthesis, and so on [31]. For these functions, membrane integrity is clearly a prerequisite such that its disturbance can cause various devastating and irreversible processes such as loss of cytoplasm, metabolic dysfunction, and eventual cell death [32]. To validate the proposed membrane-targeting mechanism of CAms, *S. aureus* and *E. coli* were selected from Gram-positive and Gram-negative bacterial strains, respectively. Bacteria were treated with the leading antimicrobial ***5b*** aforementioned at its MIC levels. Significant morphological and ultrastructural alternations in comparison to the control (untreated bacterial cells) were observed with scanning electron microscopy (SEM) and transmission electron microscopy (TEM).

Control cells (**Figure 3.4**A and C) in SEM images appeared intact with smooth and well-defined surfaces, whereas treated cells showed severe membrane disruption and deformation. Open holes, deep craters, and protruding bumps (**Figure 3.4**B) were observed with *S. aureus* treated with ***5b***, which would likely cause subsequent loss of cytoplasmic contents from the bacterial cells. Furthermore, burst cells and cellular debris of *S. aureus*, as a result of complete lysis, were also seen. Similarly, for treated *E. coli* cells (**Figure 3.5**D), blisters and bumps formed on the surface, indicating the disruption and alteration of cell membranes.

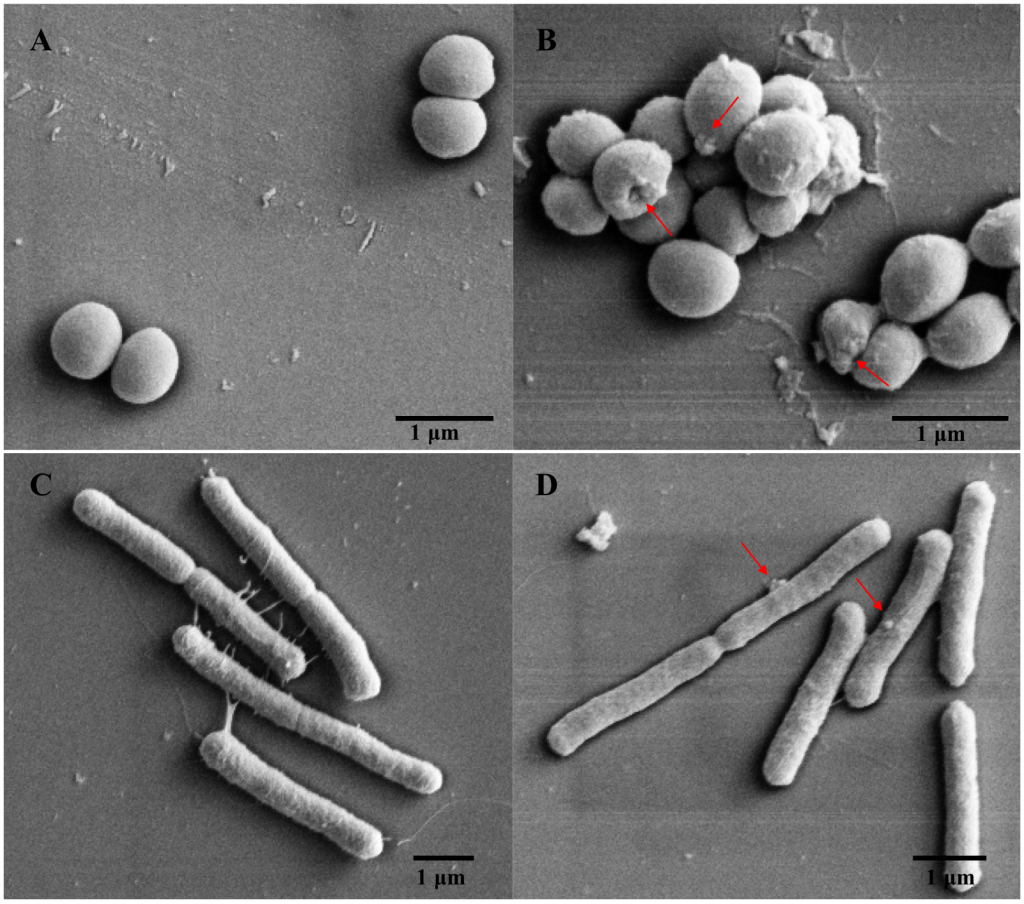

Figure 3.4. SEM micrographs of *S. aureus* and *E. coli* before (A, C) and after (B, D) incubation with ***5b*** at their respective MICs. Varied morphology changes of cell membranes were indicated by red arrows.

Using TEM, the ultrastructural changes in bacteria induced by CAms were examined. Prior to treatment, *S. aureus* showed regular round, proliferating cells with intact and smooth surfaces (**Figure 3.5**A). In addition, the intracellular DNA region displayed a heterogeneous electron density. However, upon treatment with ***5b***, the bacteria showed profound internal damage, aside from cell membranes disruption (**Figure 3.5**B) [32]. Multiple spherical void structures were observed, as well as cytoplasm with a more uniform electron density. Initially, *E. coli* displayed normal rod

shape and undamaged cell membrane structure (**Figure 3.5**C). On the contrary, treated *E. coli* experienced extensive ultrastructural damage and showed strong evidence of membrane disruption and rupture (**Figure 3.5**D). Periplasmic space was expanded and had an irregular course, suggestive of increased membrane permeability. The polar regions of the cells were especially susceptible to the CAm treatment and experienced fragmentation; this effect may be explained by the preferential interaction of cationic amphiphiles with negatively charged cardiolipin microdomains, which are mostly located at the poles [33].

From the combined evidence of SEM and TEM, it can be inferred that CAms possess antimicrobial activity with cell membrane disruption being the mode of action. To fully understand the interaction between CAm and membranes, full atomistic MD simulations was employed.

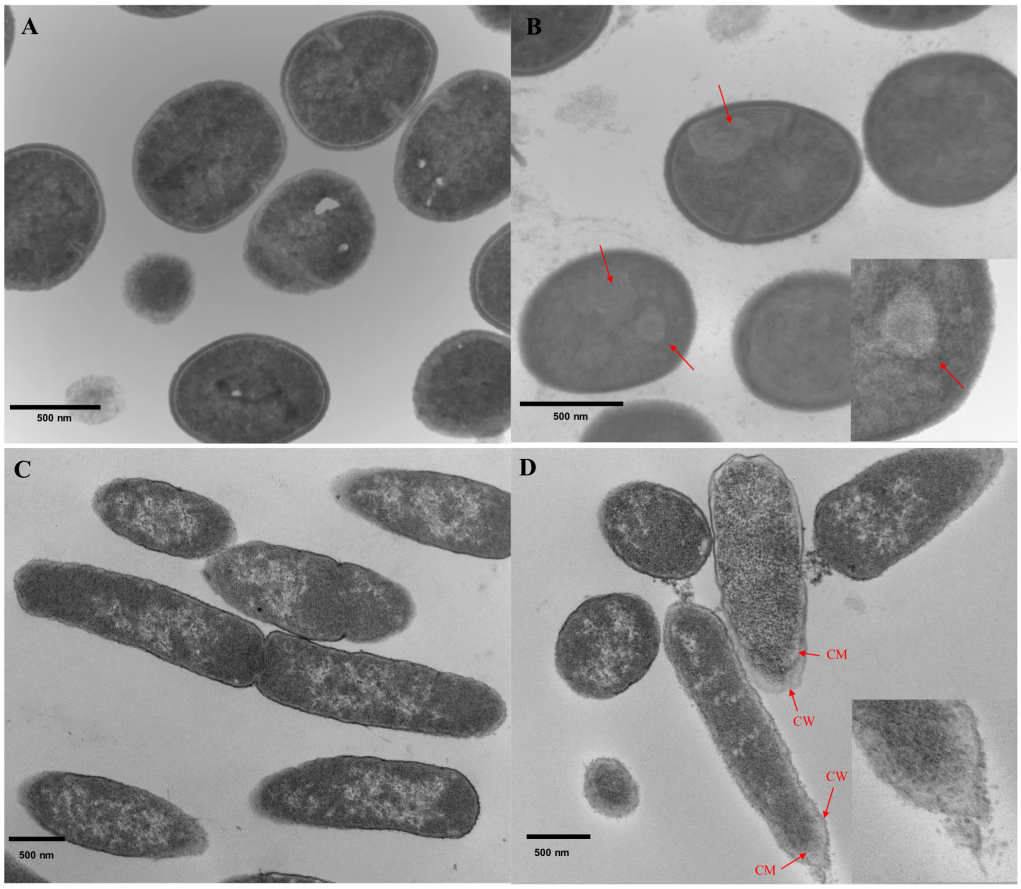

Figure 3.5. TEM micrographs of *S. aureus* and *E. coli* before (A, C) and after (B, D) incubation with ***5b*** at their respective MICs. CW (cell wall or outer membrane), CM (cell inner membrane).

3.2.6. MD Simulation

All-atom MD simulation was applied to elucidate the interaction between CAms and membranes, to shed light on the underlying mechanism of potent antimicrobial efficacy as well as selectivity towards bacteria over mammalian cells. We constructed a neutral bilayer to mimic a mammalian cell membrane with POPC as the top leaflet and mixture of POPE/POPG (1:1) as the bottom leaflet [34]. A mixture of anionic lipids

POPE/POPG (3:1) in both leaflets was used to mimic the main components of a bacterial cell membrane [35].

Lead compound ***5b*** was selected and rigidly docked on the surface of membranes; followed by MD simulation for up to 50 ns. MD trajectories were collected and averaged structures of CAm-membrane ensembles were calculated for every 1 ns. Preferable interaction patterns for ***5b*** were clearly observed with negative charge bearing bacterial membrane (**Figure 3.6** and **Figure 3.7**). The insertion of one alkyl arm of ***5b*** into bacterial membrane happened within 1 ns of simulation, compared to 10 ns for the mammalian membrane, and retained with much deeper penetration throughout the entire simulation (**Figure 3.6**A). An even more striking difference was observed at the more advanced stages of MD simulation; around 42 ns, the second alkyl arm of ***5b*** got penetrated into the bacterial membrane (**Figure 3.6**B). Contrarily, ***5b*** adopted a more extended conformation on the surface of the mammalian membrane within one hydrophobic arm remained in the water phase throughout the time period, implying weak CAm-mammalian membrane interaction, and corroborating with the hemolysis data.

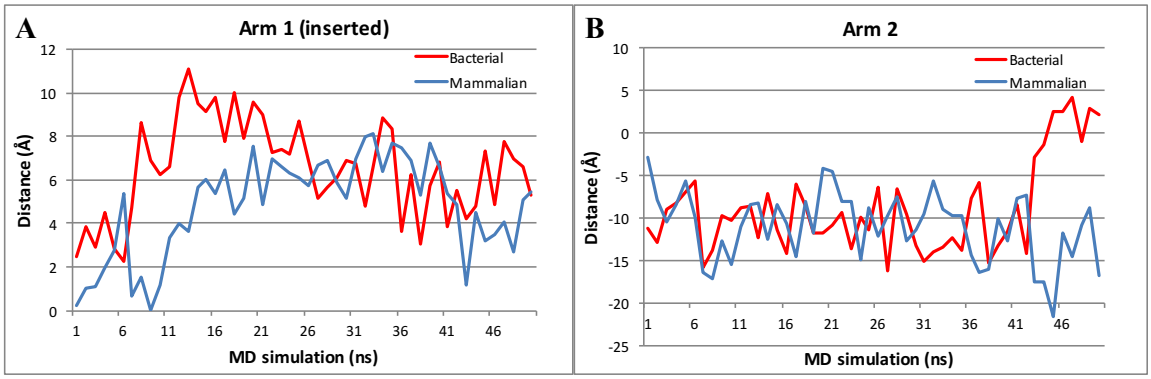

Figure 3.6. Distance of Arm 1 (A) and Arm 2 (B) to bacterial and mammalian membranes determined via MD simulation. Positive values for penetration into membrane while negative values for above the membrane.

Notably, ***5b*** adopted a facially amphiphilic conformation in the membrane-bound state with the bacterial membrane (**Figure 3.7**B, t=50 ns). At 20 ns, the tartaric acid backbone was parallel to the membrane surface, with ammonium groups localized at the water-membrane interface and one alkyl arm buried into the membrane hydrophobic core. With longer simulation times, the cooperative electrostatic and hydrophobic interactions facilitated the other hydrophobic arm of ***5b*** to rearrange then project into the hydrophobic membrane environment, leading to efficient disruption of the bacterial membrane. The flexible ether linkage allows this conformational reorientation, likely contributing to the potent bioactivity of ether-linked CAms. During this process, ammonium groups likely form a complex with negatively charged lipid head groups by a combination of electrostatic and hydrogen bonding effects, which has been previously observed [13].

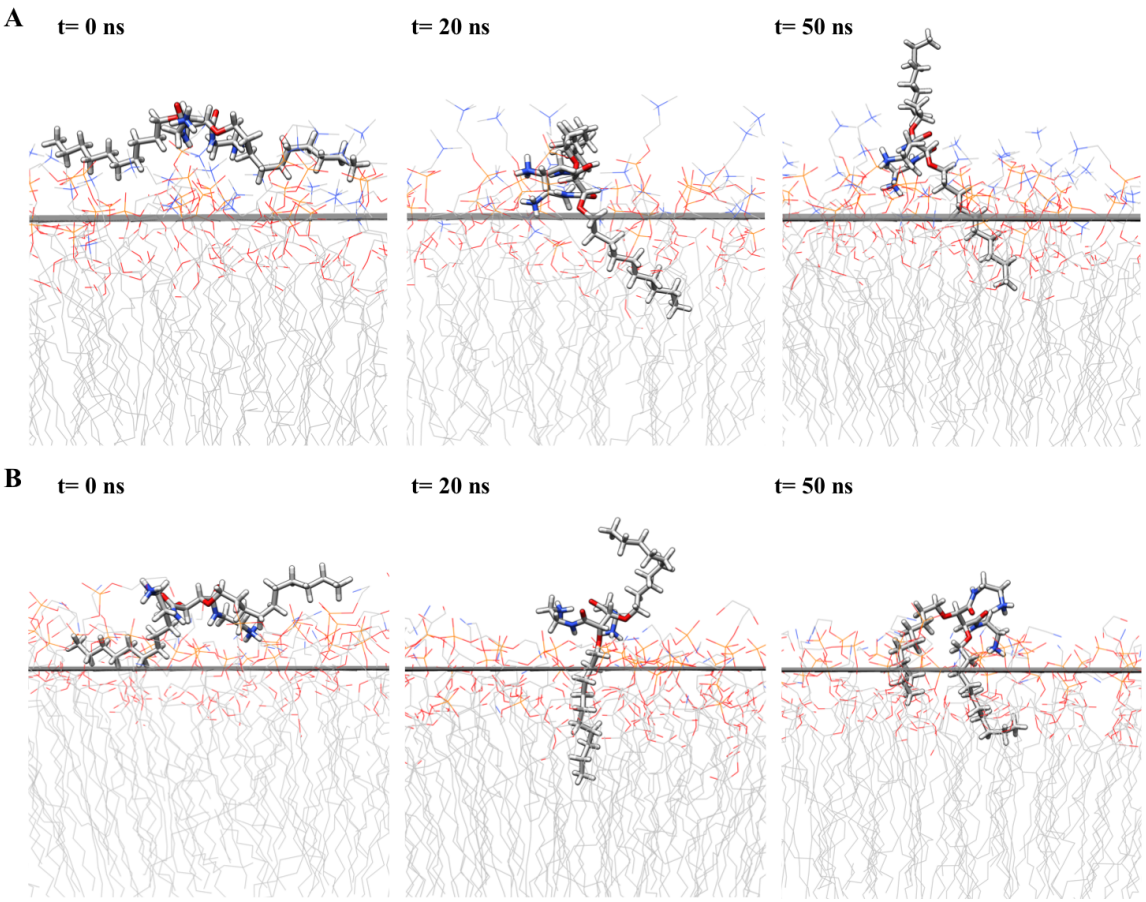

Figure 3.7. Snapshots along the simulation trajectory for mammalian membrane (A) and bacterial membrane (B) at time steps. Water and ions are not shown for clarity. Atoms are color-coded: C (grey), H (white), O (red), N (blue).

Several prevailing models for the interaction of AMPs with the membranes, such as “barrel stave”, “toroidal pore”, “carpet model”, and detergent model have been postulated [36]. While barrel-stave and toroidal pores models involved the formation of pores or channels through the membrane, AMPs can also intensively adsorb onto the surface and insert into the membrane to induce change in membrane permeability and integrity (carpet model) or act as detergents to extract lipids from the membrane [37].

The average thickness of the solvated and equilibrated POPE/POPG bilayer prior to CAm docking was found to be 43 – 45 Å. In comparison, the theoretical length for the fully stretched conformation of ***5b*** is about 24 Å, with a single hydrophobic arm being around 10 – 12 Å, which is unlikely to span the lipid bilayer and damage bacterial cell membrane through the pore formation models. We speculate the antimicrobial mechanism of CAms is more likely the "carpet model" in which AMPs are attracted to membrane surface via electrostatic effects followed by insertion into the membrane.

3.3. Conclusion

Taking a biomimetic approach, we designed and synthesized two series of biscationic amphiphiles as AMP mimics that self-assembled into spherical nanostructures in aqueous solutions. By fine-tuning the hydrophobicity, leading CAms with broad-spectrum antimicrobial activity and desirable safety profiles were identified. Additionally, molecular conformation and assembly state were identified as key determinants for optimal antimicrobial efficacy. Ether-linked CAms are expected to exhibit better performance than ester-linked counterparts *in vivo* due to enhanced enzymatic stability. These molecules hold great promise to combat drug-resistance pathogens and are currently under investigation to eradicate biofilms; this information will be reported in future works.

3.4. Experimental

3.4.1. Materials

All reagents and solvents were purchased from Sigma-Aldrich (Milwaukee, WI) and used as received unless otherwise mentioned. Di-*tert*-butyl *L*-tartrate [20] and di-2-bocaminoethyltartramide [38] were prepared as previously published. Anhydrous dimethylformamide (DMF) was dried over 4 Å molecular sieves at room temperature at least overnight prior to use. 1 N hydrochloric acid (HCl) was purchased from Fisher Scientific (Fair Lawn, NJ). *N*-Boc-ethylenediamine was purchased from Alfa Aesar (Ward Hill, MA). 1-(3-Dimethylaminopropyl)-2-ethylcarbodiimide hydrochloride (EDC·HCl) was purchased from AK Scientific (Union City, CA). Silicon wafers were purchased from Ted Pella, Inc. (Redding, CA). For cell experiments, reagents include human buffy coats purchased from the New York Blood Center (Long Island City, NY), penicillin/streptomycin purchased from Lonza (Basel, Switzerland), Dulbecco's modified eagle medium (DMEM) and Vybrant® MTT cell proliferation assay kit purchased from ThermoFisher Scientific (Waltham, MA).

3.4.2. Characterization

Proton (^{1}H) and carbon (^{13}C) NMR were recorded on a Varian 400 or 500 MHz spectrophotometer. Samples (~ 2 – 10 mg/mL) were dissolved in deuterated chloroform ($CDCl_3$) or deuterated CD_3OD with trimethylsilane (TMS) or deuterated solvent (CD_3OH) as an internal reference. FT-IR spectra were acquired using a Thermo Scientific Nicolet iS10 spectrophotometer by solvent-casting onto sodium chloride (NaCl) plates; each spectrum was an average of 32 scans. Molecular weights were determined by a ThermoQuest Finnigan LCQ-DUO system (Thermo Scientific, Waltham, MA) equipped with an electrospray ionization (ESI) source, mass spectrometer (MS) detector, a syringe

pump and the Xcalibur data system. Samples were dissolved in spectrophotometric grade methanol (MeOH) at a concentration of 10 μg/mL.

3.4.3. Synthesis of Ether-linked Cationic Amphiphiles

3.4.3.1. Synthesis of alkylated di-*tert*-butyl *L*-tartrate (**2**)

The alkylation of di-*tert*-butyl *L*-tartrate with 1-bromooctane to prepare ***2a*** is presented as an example. Following a modified literature procedure [24], di-*tert*-butyl *L*-tartrate (600 mg, 2.29 mmol) was dissolved in 20 mL anhydrous DMF under argon, and the solution was then cooled to 0 ˚C using an ice bath. Sodium hydride (NaH, 192 mg, 4.80 mmol) was added and the reaction stirred for 20 min. 1-Bromododecane (0.88 mL, 5.03 mmol) was added dropwise and the reaction mixture was allowed to stir overnight and warmed to room temperature. The reaction was quenched with 20 mL saturated ammonium chloride (NH_4Cl) solution and extracted with ethyl acetate (3x 20 mL). Organic layers were combined, washed with brine (1x 60 mL), and dried over magnesium sulfate ($MgSO_4$) before solvent was removed *in vacuo*. ***2a*** was purified on silica gel via column chromatography using a hexane: ethyl acetate gradient (100:0 to 98:2).

2a. Yield: 353 mg, 48% (colorless oil). ^{1}H-NMR (500 MHz, $CDCl_3$): 4.16 (s, 2H), 3.72 (m, 2H), 3.30 (m, 2H), 1.57 (m, 4H), 1.49 (s, 18H), 1.25 (br, 20H), 0.86 (t, 6H). ^{13}C-NMR (500 MHz, $CDCl_3$): 169.17, 81.92, 80.67, 72.68, 32.04, 29.68, 29.43, 28.36, 26.24, 22.86, 14.29. IR (cm^{-1}, thin film from $CHCl_3$): 1748 (C=O, ester), 1109 (C-O). ESI-MS m/z: 509.2 $[M+Na]^+$.

2b. Yield: 435 mg, 60% (colorless oil). ^{1}H-NMR (500 MHz, $CDCl_3$): δ 4.15 (s, 2H), 3.72 (m, 2H), 3.29 (m, 2H), 1.57 (m, 4H), 1.49 (t, 18H), 1.24 (br, 28H), 0.87 (t, 6H).

^{13}C-NMR (400 MHz, $CDCl_3$): δ 169.12, 81.87, 80.65, 72.65, 32.09, 29.85, 29.76, 29.71, 29.51, 28.33, 26.23, 22.87, 14.29. IR (cm^{-1}, thin film from $CHCl_3$): 1755 (C=O, ester), 1116 (C-O). ESI-MS m/z: 565.3 $[M+Na]^+$.

2c. Yield: 275 mg, 60 % (colorless oil). ^{1}H-NMR (400 MHz, $CDCl_3$): δ 4.16 (s, 2H), 3.72 (m, 2H), 3.30 (m, 2H), 1.60 (br, 4H), 1.49 (s, 18H), 1.24 (b, 36H), 0.88 (t, 6H). ^{13}C-NMR (500 MHz, $CDCl_3$): δ 169.18, 81.93, 80.69, 72.68, 32.15, 29.87, 29.57, 28.37, 26.25, 22.91, 14.34. IR (cm^{-1}, thin film from $CHCl_3$): 1751 (C=O, ester), 1112 (C-O). ESI-MS m/z: 621.4 $[M+Na]^+$.

3.4.3.2. Synthesis of alkylated *L*-tartaric acid (**3**)

The deprotection of ***2*** to afford ***3*** is presented using ***3a*** as an example. Following a modified literature procedure [38], ***2a*** (397 mg, 0.82 mmol) was dissolved in 13 mL anhydrous dichloromethane (DCM) under argon and the solution was cooled to 0 ˚C using an ice bath. TFA (2.5 mL, 32.64 mmol) was added dropwise via a syringe, and the reaction mixture was allowed to stir overnight and warmed up to room temperature. The crude mixture was concentrated in *vacuo* to remove solvent and TFA, and then precipitated in chilled hexane (100 mL). The pure product was isolated via vacuum filtration.

3a. Yield: 296 mg, 97 % (white solid). ^{1}H-NMR (400 MHz, CDCl3): 4.39 (s, 2H), 3.73 (m, 2H), 3.49 (m, 2H), 1.60 (m, 4H), 1.26 (br, 20H), 0.88 (t, 6H). ^{13}C-NMR (500 MHz, $CDCl_3$): 173.13, 79.65, 73.68, 32.00, 29.50, 29.47, 29.39, 25.94, 22.84, 14.28. IR (cm^{-1}, thin film from $CHCl_3$): 3350 – 3600 (COOH), 1731 (C=O), 1100 (C-O). ESI-MS m/z: 373.3 $[M-H]^-$.

3b. Yield: 205 mg, 97 % (white solid). ^{1}H-NMR (400 MHz, $CDCl_3$): δ 4.38 (s, 2H), 3.71 (m, 2H), 3.50 (m, 2H), 1.60 (m, 4H), 1.26 (br, 28H), 0.88 (t, 6H). ^{13}C-NMR (400 MHz, $CDCl_3$): δ 172.09, 79.63, 73.81, 32.11, 29.77, 29.74, 29.56, 29.53, 25.96, 22.90, 14.33. IR (cm^{-1}, thin film from $CHCl_3$): 3300 – 3600 (COOH), 1735 (C=O), 1097 (C-O). ESI-MS m/z: 429.3 $[M-H]^-$.

3c. Yield: 200 mg, 89% (white solid). ^{1}H-NMR (400 MHz, $CDCl_3$): 4.38 (s, 2H), 3.69 (m, 2H), 3.53 (m, 2H), 1.60 (m, 4H), 1.25 (br, 36H), 0.88 (t, 6H). ^{13}C-NMR (500 MHz, $CDCl_3$): 172.49, 79.40, 73.64, 34.20, 31.90, 29.63, 29.61, 29.57, 29.49, 29.35, 29.33, 29.27, 25.72, 22.67, 14.10. IR (cm^{-1}, thin film from $CHCl_3$): 3100 – 3600 (COOH), 1744 (C=O), 1109 (C-O). ESI-MS m/z: 485.7 $[M-1]^-$.

3.4.3.3. Synthesis of *N*-Boc alkylated tartaric acid (**4**)

The conjugation of *N*-Boc ethylendiamine to ***3*** to prepare ***4*** is presented using ***4a*** as an example. Following a previously published procedure [38], ***3a*** (296 mg, 0.79 mmol), EDC·HCl (637 mg, 3.32 mmol), and 4-dimethylaminopyridine (DMAP, 193 mg, 1.58 mmol) were dissolved in 7 mL anhydrous DCM under argon. Upon complete dissolution, *N*-Boc-ethylenediamine (0.31 mL, 1.98 mmol) was added via syringe and the reaction stirred overnight at room temperature. The reaction mixture was washed with 10% potassium bisulfate ($KHSO_4$, 2x 15mL) and brine (1x 15mL). The crude mixture was then dried over $MgSO_4$, filtered, and concentrated *in vacuo*. The crude product was then precipitated in chilled hexane (100 mL) and isolated via vacuum filtration.

4a. Yield: 316 mg, 61% (white powder). ^{1}H-NMR (400 MHz, $CDCl_3$): δ 7.03 (s, 2H), 4.95 (s, 2H), 4.23 (s, 2H), 3.52 (m, 8H), 3.28 (m, 4H), 1.55 (m, 4H), 1.44 (s, 18H), 1.26 (br, 20H), 0.88 (t, 6H). ^{13}C-NMR (500 MHz, $CDCl_3$): δ 171.11, 156.35, 81.44, 73.53,

40.73, 39.88, 32.03, 29.91, 29.58. 29.46, 28.60, 26.19, 22.84, 14.30. IR (cm^{-1}, thin film from $CHCl_3$): 3373 (NH), 1690 (C=O, carbamide), 1654 (C=O, amide). ESI-MS m/z: 681.2 $[M+Na]^+$.

4b. Yield: 300 mg, 68 % (white powder). ^{1}H-NMR (400 MHz, $CDCl_3$): δ 7.05 (s, 2H), 4.97 (s, 2H), 4.22 (s, 2H), 3.52 (m, 8H), 3.28 (m, 4H), 1.54 (m, 4H), 1.43 (s, 18H), 1.25 (br, 28H), 0.87 (t, 6H). ^{13}C-NMR (500 MHz, $CDCl_3$): δ 170.96, 156.45, 81.44, 79.75, 73.53, 40.73, 39.87, 32.11, 29.91, 29.52, 29.66, 29.81, 29.91, 28.61, 26.20, 22.89, 14.33. IR (cm^{-1}, thin film from $CHCl_3$): 3349 (NH), 1702 (C=O, carbamide), 1677 (C=O, amide). ESI-MS m/z: 738.1 $[M+Na]^+$.

4c. Yield: 300 mg, 70 % (white powder). ^{1}H-NMR (400 MHz, $CDCl_3$): δ 7.04 (s, 2H), 4.96 (s, 2H), 4.22 (s, 2H), 3.52 (m, 8H), 3.28 (m, 4H), 1.54 (m, 4H), 1.44 (s, 36H), 1.25 (br, 28H), 0.87 (t, 6H). ^{13}C-NMR (500 MHz, $CDCl_3$): ^{13}C-NMR (400 MHz, $CDCl_3$): 170.94, 98.92, 81.46, 77.97, 73.51, 32.12, 29.91, 29.85, 29.63, 29.55, 28.60, 26.20, 22.89, 14.31. IR (cm^{-1}, thin film from $CHCl_3$): 3340 (NH), 1693 (C=O, carbamide), 1655 (C=O, amide). ESI-MS m/z: 793.7 $[M+Na]^+$.

3.4.3.4. Synthesis of ether-linked cationic amphiphiles (CAm, **5**)

The deprotection of ***4a*** to afford ***5a*** is presented as an example. Briefly, ***4a*** (305 mg, 0.463 mmol) was dissolved in 4.7 mL HCl (4M in dioxane, 18.52 mmol) and then cooled to 0 ˚C under argon using an ice bath. The reaction mixture was allowed to stir overnight and warmed to room temperature before work-up. The crude product was concentrated *in vacuo* and re-dissolved in minimal methanol (1 mL), followed by precipitation into a 50 mL centrifuge tube containing chilled diethyl ether (45 mL). ***5a***

was then isolated via centrifugation (Hettich EBA 12, Beverly, MA; 3500 rpm, 3x 5 min) and the supernatant decanted.

5a. Yield: 255 mg, quantitative yield (off-white solid). ^{1}H-NMR (400 MHz, CD_3OD): δ 8.40 (br, 2H), 4.03 (s, 2H), 3.64 (m, 4H), 3.47 (m, 4H), 3.10 (m, 4H), 1.62 (m, 4H), 1.31 (br, 20H), 0.90 (t, 6H). ^{13}C-NMR (400 MHz, CD_3OD): δ 172.49, 82.77, 72.34, 36.56, 31.88, 29.56, 29.42, 29.29, 25.96, 22.56, 13.26. IR (cm^{-1}, thin film from $CHCl_3$): 3419 (NH), 1644 (C=O, amide). ESI-MS m/z: 460.5 $[M+H]^+$.

5b. Yield: 188 mg, 92 % (off-white solid). ^{1}H-NMR (400 MHz, CD_3OD): 8. 40 (br. 2H), 4.01 (s, 2H), 3.64 (m, 4H), 3.45 (m, 4H), 3.10 (t, 4H), 1.62 (m, 4H), 1.30 (s, 28H), 0.90 (t, 6H). ^{13}C-NMR (400 MHz, $CDCl_3$): 172.47, 82.84, 72.31, 39.93, 36.55, 31.91, 29.65, 29.61, 29.57, 29.47, 29.33, 25.98, 22.57, 13.27. IR (cm^{-1}, thin film from $CHCl_3$) 3424 (NH), 1648 (C=O, amide). ESI-MS m/z: 515.4 $[M+H]^+$.

5c. Yield: 220 mg, quantitative yield (off-white solid). ^{1}H-NMR (500 MHz, $CDCl_3$): δ 8.42 (br, 2H), 4.00 (s, 2H), 3.66 (m, 4H), 3.46 (m, 4H), (s, 4H), 1.63 (m, 4H), 1.29 (s, 38H), 0.90 (t, 6H). ^{13}C-NMR (500 MHz, $CDCl_3$): δ 172.47, 82.91, 72.29, 29.65, 29.62, 29.57, 29.49, 29.33, 25.99, 22.56, 13.27. IR (cm^{-1}, thin film from $CHCl_3$) 3424 (NH), 1656 (C=O, ester). ESI-MS m/z: 571.9 $[M+1]^+$.

3.4.4. Synthesis of Ester-linked Cationic Amphiphiles

3.4.4.1. Synthesis of acylated di-2-bocaminoethyltartramide (**7**)

The acylation of di-2-bocaminoethyltartramide (***6***) to prepare ***7*** is presented using ***7a*** as an example. Following a published procedure [38], octanoic acid (146 mg, 1.01 mmol), di-2-bocaminoethyltartramide (200 mg, 0.46 mmol), and DMAP (23 mg, 0.19

mmol) were dissolved in 16 mL anhydrous DCM and 7 mL anhydrous DMF under nitrogen. EDC·HCl (370 mg, 1.93 mmol) was added, and the reaction stirred overnight at room temperature. The reaction mixture was concentrated *in vacuo* and then reconstituted in DCM, washed with aqueous solutions of 10% $KHSO_4$ (3x 40 mL), saturated sodium bicarbonate ($NaHCO_3$, 3x 40 mL) solution, and brine (1x 50 mL). The combined organic layer was dried over $MgSO_4$, concentrated *in vacuo*, and then triturated in 100 mL hexanes for 4 h, and the pure product was isolated via vacuum filtration.

7a. Yield: 280 mg, 89% (white solid). ^{1}H-NMR (MHz, $CDCl_3$): δ 6.97 (s, 2H), 5.57 (s, 2H), 5.13 (s, 2H), 3.28 (m, 8H), 2.46 (m, 4H), 1.62 (m, 4H), 1.45 (s, 18H), 1.29 (br, 16H), 0.88 (t, 6H). ^{13}C-NMR (MHz, $CDCl_3$): δ 172.32, 167.01, 79.96, 72.42, 41.23, 39.94, 34.04, 31.88, 29.25, 28.60, 24.89, 22.81, 14.27. IR (cm^{-1}, thin film from $CHCl_3$): 3454 (NH), 1793 (C=O, ester), 1751 (C=O, carbamide), 1694 (C=O, amide). ESI-MS m/z: 709.5 $[M+Na]^+$.

7b. Yield: 290 mg, 85% (white solid). ^{1}H-NMR (MHz, $CDCl_3$): δ 7.04 (s, 2H), 5.58 (s, 2H), 5.17 (s, 2H), 3.29 (m, 8H), 2.44 (m, 4H), 1.63 (m, 4H), 1.45 (s, 18H), 1.26 (br, 24H), 0.88 (t, 6H). ^{13}C-NMR (MHz, $CDCl_3$): δ 172.33, 167.04, 79.96, 72.41, 41.23, 39.95, 34.04, 32.07, 29.66, 29.49, 29.31, 28.61, 24.89, 22.88, 14.31. IR (cm^{-1}, thin film from $CHCl_3$): 3454 (NH), 1794 (C=O, ester), 1752 (C=O, carbamide), 1694 (C=O, amide). ESI-MS m/z: 765.5 $[M+Na]^+$.

7c. Yield: 350 mg, 95% (white solid). ^{1}H-NMR (MHz, $CDCl_3$): δ 6.96 (s, 2H), 5.56 (s, 2H), 5.12 (s, 2H), 3.28 (m, 8H), 2.43 (m, 4H), 1.63 (m, 4H), 1.45 (s, 18H), 1.26 (br, 32H), 0.89 (t, 6H). ^{13}C-NMR (MHz, $CDCl_3$): δ 172.32, 167.02, 79.95, 72.44, 41.21, 39.94, 34.05, 32.12, 29.84, 29.72, 29.54, 29.32, 28.61, 24.90, 22.90, 14.33. IR (cm^{-1}, thin

film from $CHCl_3$): 3454 (NH), 1794 (C=O, ester), 1752 (C=O, carbamide), 1694 (C=O, amide). ESI-MS m/z: 821.5 $[M+Na]^+$.

3.4.4.2. Synthesis of ester-linked CAm (**8**)

The deprotection of ***7*** to afford ***8*** is presented using ***8a*** as an example. The deprotection was carried out in a similar manner as was the ether-linked CAms, using ***7a*** (275 mg, 0.40 mmol) and HCl (4M in dioxane, 16 mmol, 4 mL). If necessary, additional anhydrous dioxane (0.5 – 1mL) was added to improve stirring.

8a. Yield: 210 mg, 94% (off-white solid). ^{1}H-NMR (MHz, CD_3OD): δ 8.62 (s, 2H), 5.57 (s, 2H), 3.50 (m, 4H), 3.07 (m, 4H), 2.50 (m, 4H), 1.62 (m, 4H), 1.33 (br, 16H), 0.91 (t, 6H). ^{13}C-NMR (MHz, CD_3OD): δ 172.90, 168.96, 72.42, 39.44, 36.93, 33.35, 31.68, 28.93, 28.93, 24.59, 22.50, 13.22. IR (cm^{-1}, KBr): 3452 (NH), 1740 (C=O, ester), 1656 (C=O, amide). ESI-MS m/z: 487.4 $[M+H]^+$.

8b. Yield: 230 mg, 93% (white solid). ^{1}H-NMR (MHz, CD_3OD): δ 8.62 (s, 2H), 5.57 (s, 2H), 3.49 (m, 4H), 3.07 (m, 4H), 2.49 (m, 4H), 1.62 (m, 4H), 1.32 (br, 24H), 0.90 (t, 6H). ^{13}C-NMR (MHz, CD_3OD): δ 172.89, 168.96, 72.43, 39.45, 36.95, 33.37, 31.87, 29.42, 29.28, 29.26, 28.99, 24.60, 22.55, 13.25. IR (cm^{-1}, KBr): 3447 (NH), 1744 (C=O, ester), 1666 (C=O, amide). ESI-MS m/z: 543.3 $[M+H]^+$.

8c. Yield: 250 mg, 94% (white solid). ^{1}H-NMR (MHz, CD_3OD): δ δ 8.62 (s, 2H), 5.56 (s, 2H), 3.51 (m, 4H), 3.08 (m, 4H), 2.47 (m, 4H), 1.62 (m, 4H), 1.29 (br, 32H), 0.90 (t, 6H). ^{13}C-NMR (MHz, CD_3OD): δ 172.88, 168.95, 72.44, 39.46, 36.93, 33.39, 31.90, 29.60, 29.47, 29.30, 29.00, 24.62, 22.55, 13.25. IR (cm^{-1}, KBr): 3448 (NH), 1742 (C=O, ester), 1654 (C=O, amide). ESI-MS m/z: 599.5 $[M+H]^+$.

3.4.5. DLS and Zeta Potential Measurements

DLS and zeta potential were measured using a NanoZS90 instrument (Malvern Instruments, Southboro, MA). Samples were dissolved DI water at 1 mg/mL and filtered using 0.45 μm polytetrafluoroethylene (PTFE) syringe filters before measurement. To determine micelle sizes, each sample was run at a 90° scattering angle in triplicate with 30 measurements per run at 25 °C. All results are presented as mean ± standard deviation around the mean.

3.4.6. CMC

The surface tensions (γ) of CAms were measured using a Fisher Surface Tensiometer model 21 (Waltham, MA) according to the du Nouy's method at room temperature [39]. The platinum ring was rinsed with hexane, methanol, and DI water followed by heating with a Bunsen burner before use. A stock solution of CAms (5 mL) was transferred into a carefully cleaned vessel and γ was measured repeatedly at least three times until the variation was smaller than 0.2 mN/m. The amphiphiles were then diluted with an aliquot of DI water and γ was collected at different concentrations. The γ values were then plotted against the logarithm of CAm concentrations, and the inflection point was taken as CMC.

3.4.7. Bacterial Cell Culture *(Performed and written by Ammar Algburi, Rutgers University)*

The bacterial strains used for antimicrobial assay included: Staphylococcus aureus (S. aureus) ATCC 13565, Listeria monocytogenes (L. monocytogenes) Scott A,

Pseudomonas aeruginosa (P. aeruginosa) ATCC 15442, Escherichia coli (E. coli) O157:H7, and Salmonella enterica serovar typhimurium (S. typhimurium). From the frozen stock (- 80˚C), bacteria were inoculated into brain-heart infusion (BHI) agar (Becton Dickinson, Franklin Lakes, NJ) and propagated under aerobic conditions at 37 ˚C for 24 h. After the incubation, one colony of each bacterial strain was transferred separately to BHI broth (Becton Dickinson, Franklin Lakes, NJ) and incubated under aerobic condition at 37 ˚C for 18 – 24 h. For broth microdilution assay, the bacterial growth suspensions were further diluted in fresh BHI medium to achieve 10^6 CFU/mL.

3.4.8. Broth Microdilution Assay *(Performed and written by Ammar Algburi, Rutgers University)*

The minimal inhibitory concentration (MIC) of CAms were identified using a broth microdilution assay modified from previous studies [40]. Briefly, the stock solutions of CAms were prepared at the day of experiment by dissolving in double-distilled water (ddH_2O) and then sterilized under UV light for 25 min. The stock solutions were serial 2-fold diluted into a 96-well microplate ((Becton Dickinson, Franklin Lakes, NJ) with BHI broth with a final volume of 100 μL. Aliquots (100 μL) of bacterial suspensions mentioned above were added to each well of the microplate. Plates were incubated at 37 °C for 24 h under aerobic conditions. The optical density readings of the microorganism at 595 nm were tracked using a microplate reader (Model 550, Bio-Rad Laboratories, Hercules, CA). The MIC was determined as the lowest CAm concentration that produced no visible growth after overnight incubation.

3.4.9. SEM

Bacteria were grown to the mid-exponential growth phase. Silicon wafers were submerged in the bacterial solutions in the presence or absence of CAms at their respective MICs and incubated for 1 h. Glucose (0.25 %) was added to facilitate attachment. The bacteria on wafers were fixed in 2.5% glutaraldehyde for 1 h at room temperature, washed three times with PBS, and post-fixed 1% osmium tetroxide. The samples were then dehydrated in a graded series of ethanol solutions (50%, 70%, 80%, 95%, 100%), dried with graded hexamethyldisilazane (50%, 100%), and air dried for two days at room temperature. After drying, the wafers were mounted on stubs and sputter-coated with 20 nm gold prior to inspection under the microscope (Zeiss Sigma Field Emission SEM, Carl Zeiss, Ontario, CA) at 5 kV.

3.4.10. TEM

For micelle samples, a drop of the micelle solution was deposited onto on a carbon film-coated copper grid. After 60 seconds, excess solution was removed by tapping the edge of the grid with filter paper. A drop of 1% uranyl acetate solution was then applied to the same grid for 60 seconds. The grid was again tapped dry and further dried in the desiccator overnight. For bacteria samples, bacteria were grown as described above for SEM sample preparation. In brief, bacteria were incubated in the presence or absence of CAms at their respective MICs for 1 h. After centrifugation at 500 × *g* for 10 min, the resulting pellet was fixed in 2.5% glutaraldehyde, washed three times with PBS, and postfixed with 1% osmium tetroxide. The samples were then dehydrated with graded ethanol series (50%, 70%, 80%, 95%, 100%) and embedded in epoxy resin (Dr. Spurr's

kit, Electron Microscopy Sciences, Hatfield, PA). Ultrathin sectioning of the cells was stained with 1% uranyl acetate. The microscopy was performed with JEOL 1200EX electron microscope (JEOL USA, Inc., Peabody, MA) at 80 kV.

3.4.11. Hemolytic Activity

Hemolytic activity was determined following a modified procedure in literature [41]. hRBCs were isolated from 7 mL human blood samples by centrifuging at 400 × *g* for 10 min (Allegra 21 centrifugation, Beckman Coulter, Brea, CA) to remove the plasma and buffy coat. The remaining pelleted RBCs were then washed with 15 mL sterile PBS five times until no traces amount of plasma were observed. The supernatant was carefully removed using a pipette.

CAm stock solutions were prepared by dissolving CAms in ddH_2O prior to use; the samples were gently agitated at 37 ˚C for 5 min until completely dissolved. To examine the hemolysis properties of CAms, RBCs were suspended with PBS (5% hematocrit). Then 100 μL of the suspended RBCs was mixed with 400 μL freshly prepared CAm stock solutions with final concentrations of 7.8, 15.6, 31.2, 62.5, 125, and 250 μg/mL. Additionally, ddH_2O water and PBS (400 μL) were incubated with 100 μL RBC suspension, serving as positive and negative controls, respectively. All the mixtures were gently shaken and incubated at 37 ˚C for 1 h. The mixtures were centrifuged at 400 × *g* (Labenet Spectrafuge 16M microcentrifuge, Labnet International, Inc., Edison, NJ) for 10 min. The supernatant (100 μL) was then transferred to a 96-well plate, and the absorbance (Abs) measured at 541 nm using an Infinite M200 PRO plate reader (Tecan

Group Ltd., Männedorf, Switzerland). The following formula is used to calculate the percent of hemolysis of RBCs:

$$\text{Hemolysis \%} = \frac{\text{Abs}_{\text{sample}} - \text{Abs}_{\text{PBS}}}{\text{Abs}_{\text{ddH2O}} - \text{Abs}_{\text{PBS}}} * 100$$

3.4.12. Human Foreskin Fibroblast (HFF) Cell Culture and MTT Assay

HFFs were cultured in DMEM supplemented with 10% fetal bovine serum, 1% penicillin/streptomycin and plated at a concentration of 10,000 cells/well in 96-well plate. Plates were incubated at 37 ˚C and 5% CO_2 for 24 h to allow cell attachment prior to use.

CAms were tested for cytotoxicity against HFFs using a tetrazolium-based colorimetric assay (MTT). CAms were first dissolved in ddH_2O and then diluted in cell medium (DMEM supplemented with 1% penicillin/streptomycin) to reach concentrations of 3.9, 1.9, and 0.95 µg/mL. Cell media (100 µL) containing CAms were then added to allocated wells in a 96-well plate. 1% Triton X-100 and cell medium only treated cells were used as positive and negative controls, respectively. After 24 h incubation, the medium was removed and replaced with fresh medium. MTT reagent (10 µL, 12 mM in PBS) was then added to each well and further incubated for 4 h at 37 °C. Formazan crystals were subsequently dissolved in 100 µL SDS solution (acidified with 0.01 M HCl) at 37 ˚C for 4 h. The absorbance (Abs) was then recorded with an Infinite M200 PRO plate reader (Tecan Group Ltd., Männedorf, Switzerland) at 570 nm. The following equation was used to calculate the percent of cell viability of HFFs:

$$\text{Cell viability \%} = \frac{\text{Abs}_{\text{sample}} - \text{Abs}_{\text{Triton X}-100}}{\text{Abs}_{\text{Trinton X}-100} - \text{Abs}_{\text{Medium}}} * 100$$

3.4.13. **Molecular Dynamics Simulations** *(Performed and written by Prof, Vladyslav Kholodovych, Rutgers University)*

Membrane patches of roughly 100 × 100 Å were constructed with CHARMM-GUI web portal. The mammalian membrane top leaflet consisted of 147 POPC (1-palmitoyl-2-oleoyl-sn-glycero-3-phosphocholine) while the bottom leaflet was an equal mixture of POPE (1-palmitoyl-2-oleoyl-sn-glycero-3-phosphoethanolamine) and POPS (1-palmitoyl-2-oleoyl-sn-glycero-3-phospho-L-serine) molecules (84:84). Bacterial membrane had a mixture of 126 POPE and 42 POPG (1-palmitoyl-2-oleoyl-sn-glycero-3-phospho-(1'-rac-glycerol)) molecules in both leaflets. Membrane minimization and equilibration were performed with established protocols [42]. Details can be found in Supplemental Information.

Leading compound ***5b*** *in its extended conformations was rigidly docked in MOE program on the surface of equilibrated membrane patches obtained after 20 ns of molecular dynamics (MD) simulations. CAm-membrane assemblies generated were selected for further modeling by visual inspection based on two criteria: the distance between any atom of* ***5b*** *and the membrane should not exceed 5 Å; there was no initial penetration of any atom of* ***5b*** *into the membrane.*

To probe the interaction between CAms and membranes, MD program suite Amber 14 was used [43, 44]. Two separate systems were created, one with a mammalian membrane and one with a bacterial membrane. Each system was prepared by solvating it in water and neutralizing with sodium ions as needed with auxiliary preparation programs from AmberTools 15. After initial minimization, heating, and equilibration totaling 2 ns, ***5b****-membrane assembles were subjected to MD simulations for 50 ns. An*

isothermal-isobaric (i.e., NPT) ensemble with Langevin thermostat and Berendsen barostat was used throughout MD simulations with restart checkpoints every 1ns. Trajectory files from each 1 ns checkpoint step of MD simulations were collected and used for obtaining an averaged structure for every 1 ns with a modified subroutine from VMD program. Thus, for each CAm-membrane assembly 50 averaged structures were calculated and compared. All calculations were performed on GPU enabled Linux cluster from OARC, Rutgers University.

3.5. References

[1] Aminov RI. A Brief History of the Antibiotic Era: Lessons Learned and Challenges for the Future. Frontiers in Microbiology. 2010;1:134.

[2] Giamarellou H. Treatment options for multidrug-resistant bacteria. Expert review of anti-infective therapy. 2006;4:601-18.

[3] Hancock REW, Lehrer R. Cationic peptides: a new source of antibiotics. Trends in Biotechnology. 1998;16:82-8.

[4] Findlay B, Zhanel GG, Schweizer F. Cationic Amphiphiles, a New Generation of Antimicrobials Inspired by the Natural Antimicrobial Peptide Scaffold. Antimicrobial Agents and Chemotherapy. 2010;54:4049-58.

[5] Guilhelmelli F, Vilela N, Albuquerque P, Derengowski L, Silva-Pereira I, Kyaw C. Antimicrobial development challenges: the various mechanisms of action of antimicrobial peptides and of bacterial resistance. Frontiers in Microbiology. 2013;4.

[6] Zasloff M. Antimicrobial peptides of multicellular organisms. Nature. 2002;415:389-95.

[7] Pushpanathan M, Gunasekaran P, Rajendhran J. Antimicrobial Peptides: Versatile Biological Properties. International Journal of Peptides. 2013;2013:15.

[8] Yeaman MR, Yount NY. Mechanisms of Antimicrobial Peptide Action and Resistance. Pharmacological Reviews. 2003;55:27-55.

[9] Cheng J, Chin W, Dong H, Xu L, Zhong G, Huang Y, et al. Biodegradable Antimicrobial Polycarbonates with In Vivo Efficacy against Multidrug-Resistant MRSA Systemic Infection. Advanced Healthcare Materials. 2015;4:2128-36.

[10] Zhao J, Zhao C, Liang G, Zhang M, Zheng J. Engineering Antimicrobial Peptides with Improved Antimicrobial and Hemolytic Activities. Journal of Chemical Information and Modeling. 2013;53:3280-96.

[11] Jiang L, Xu D, Sellati TJ, Dong H. Self-assembly of cationic multidomain peptide hydrogels: supramolecular nanostructure and rheological properties dictate antimicrobial activity. Nanoscale. 2015;7:19160-9.

[12] Yin LM, Edwards MA, Li J, Yip CM, Deber CM. Roles of Hydrophobicity and Charge Distribution of Cationic Antimicrobial Peptides in Peptide-Membrane Interactions. Journal of Biological Chemistry. 2012;287:7738-45.

[13] Palermo EF, Vemparala S, Kuroda K. Cationic Spacer Arm Design Strategy for Control of Antimicrobial Activity and Conformation of Amphiphilic Methacrylate Random Copolymers. Biomacromolecules. 2012;13:1632-41.

[14] Colak S, Nelson CF, Nüsslein K, Tew GN. Hydrophilic Modifications of an Amphiphilic Polynorbornene and the Effects on its Hemolytic and Antibacterial Activity. Biomacromolecules. 2009;10:353-9.

[15] Palermo EF, Sovadinova I, Kuroda K. Structural Determinants of Antimicrobial Activity and Biocompatibility in Membrane-Disrupting Methacrylamide Random Copolymers. Biomacromolecules. 2009;10:3098-107.

[16] Liu SQ, Venkataraman S, Ong ZY, Chan JMW, Yang C, Hedrick JL, et al. Overcoming Multidrug Resistance in Microbials Using Nanostructures Self-Assembled from Cationic Bent-Core Oligomers. Small. 2014;10:4130-5.

[17] Tang H, Doerksen RJ, Jones TV, Klein ML, Tew GN. Biomimetic Facially Amphiphilic Antibacterial Oligomers with Conformationally Stiff Backbones. Chemistry & Biology. 2006;13:427-35.

[18] Boughton AP, Andricioaei I, Chen Z. Surface Orientation of Magainin 2: Molecular Dynamics Simulation and Sum Frequency Generation Vibrational Spectroscopic Studies. Langmuir : the ACS journal of surfaces and colloids. 2010;26:16031-6.

[19] Scott RW, DeGrado WF, Tew GN. De novo designed synthetic mimics of antimicrobial peptides. Current Opinion in Biotechnology. 2008;19:620-7.

[20] Abdelhamid DS, Zhang Y, Lewis DR, Moghe PV, Welsh WJ, Uhrich KE. Tartaric acid-based amphiphilic macromolecules with ether linkages exhibit enhanced repression of oxidized low density lipoprotein uptake. Biomaterials. 2015;53:32-9.

[21] Wieprecht T, Dathe M, Beyermann M, Krause E, Maloy WL, MacDonald DL, et al. Peptide Hydrophobicity Controls the Activity and Selectivity of Magainin 2 Amide in Interaction with Membranes. Biochemistry. 1997;36:6124-32.

[22] Chen Y, Guarnieri MT, Vasil AI, Vasil ML, Mant CT, Hodges RS. Role of Peptide Hydrophobicity in the Mechanism of Action of α-Helical Antimicrobial Peptides. Antimicrobial Agents and Chemotherapy. 2007;51:1398-406.

[23] Maloy WL, Kari UP. Structure–activity studies on magainins and other host defense peptides. Biopolymers. 1995;37:105-22.

[24] Zhang Y, Li Q, Welsh WJ, Moghe PV, Uhrich KE. Micellar and structural stability of nanoscale amphiphilic polymers: Implications for anti-atherosclerotic bioactivity. Biomaterials. 2016;84:230-40.

[25] Xu D, Jiang L, Singh A, Dustin D, Yang M, Liu L, et al. Designed supramolecular filamentous peptides: balance of nanostructure, cytotoxicity and antimicrobial activity. Chemical Communications. 2015;51:1289-92.

[26] Wang X, Wang J, Wang Y, Ye J, Yan H, Thomas RK. Properties of mixed micelles of cationic gemini surfactants and nonionic surfactant triton X-100: Effects of the surfactant composition and the spacer length. Journal of Colloid and Interface Science. 2005;286:739-46.

[27] Rosen MJ, Mathias JH, Davenport L. Aberrant Aggregation Behavior in Cationic Gemini Surfactants Investigated by Surface Tension, Interfacial Tension, and Fluorescence Methods. Langmuir. 1999;15:7340-6.

[28] Feder R, Dagan A, Mor A. Structure-Activity Relationship Study of Antimicrobial Dermaseptin S4 Showing the Consequences of Peptide Oligomerization on Selective Cytotoxicity. Journal of Biological Chemistry. 2000;275:4230-8.

[29] Torrent M, Valle J, Nogués MV, Boix E, Andreu D. The Generation of Antimicrobial Peptide Activity: A Trade-off between Charge and Aggregation? Angewandte Chemie International Edition. 2011;50:10686-9.

[30] Li Y, Wu H, Teng P, Bai G, Lin X, Zuo X, et al. Helical Antimicrobial Sulfono-γ-AApeptides. Journal of Medicinal Chemistry. 2015;58:4802-11.

[31] Salton MRJ. Structure and Function of Bacterial Cell Membranes. Annual Review of Microbiology. 1967;21:417-42.

[32] Hartmann M, Berditsch M, Hawecker J, Ardakani MF, Gerthsen D, Ulrich AS. Damage of the Bacterial Cell Envelope by Antimicrobial Peptides Gramicidin S and PGLa as Revealed by Transmission and Scanning Electron Microscopy. Antimicrobial Agents and Chemotherapy. 2010;54:3132-42.

[33] Renner LD, Weibel DB. Cardiolipin microdomains localize to negatively curved regions of Escherichia coli membranes. Proceedings of the National Academy of Sciences. 2011;108:6264-9.

[34] van Meer G, de Kroon AIPM. Lipid map of the mammalian cell. Journal of Cell Science. 2010;124:5-8.

[35] Oursel D, Loutelier-Bourhis C, Orange N, Chevalier S, Norris V, Lange CM. Lipid composition of membranes of Escherichia coli by liquid chromatography/tandem mass spectrometry using negative electrospray ionization. Rapid Communications in Mass Spectrometry. 2007;21:1721-8.

[36] Shai Y. Mode of action of membrane active antimicrobial peptides. Peptide Science. 2002;66:236-48.

[37] Wimley WC. Describing the Mechanism of Antimicrobial Peptide Action with the Interfacial Activity Model. ACS Chemical Biology. 2010;5:905-17.

[38] Faig A, Arthur TD, Fitzgerald PO, Chikindas M, Mintzer E, Uhrich KE. Biscationic Tartaric Acid-Based Amphiphiles: Charge Location Impacts Antimicrobial Activity. Langmuir. 2015;31:11875-85.

[39] Zhang Y, Romsted LS, Zhuang L, de Jong S. Simultaneous Determination of Interfacial Molarities of Amide Bonds, Carboxylate Groups, and Water by Chemical Trapping in Micelles of Amphiphiles Containing Peptide Bond Models. Langmuir. 2013;29:534-44.

[40] Torcato IM, Huang Y-H, Franquelim HG, Gaspar D, Craik DJ, Castanho MARB, et al. Design and characterization of novel antimicrobial peptides, R-BP100 and RW-BP100, with activity against Gram-negative and Gram-positive bacteria. Biochimica et Biophysica Acta (BBA) - Biomembranes. 2013;1828:944-55.

[41] Joglekar M, Roggers RA, Zhao Y, Trewyn BG. Interaction effects of mesoporous silica nanoparticles with different morphologies on human red blood cells. RSC Advances. 2013;3:2454-61.

[42] Dickson CJ, Madej BD, Skjevik ÅA, Betz RM, Teigen K, Gould IR, et al. Lipid14: The Amber Lipid Force Field. Journal of Chemical Theory and Computation. 2014;10:865-79.

[43] Molecular Operating Environment (MOE). 2013.08 ed: Chemical Computing Group, Inc.; 2016.

[44] D.A. Case JTB, R.M. Betz, D.S. Cerutti, T.E. Cheatham, III, T.A. Darden, R.E. Duke, T.J. Giese, H. Gohlke, A.W. Goetz, N. Homeyer, S. Izadi, P. Janowski, J. Kaus, A. Kovalenko, T.S. Lee, S. LeGrand, P. Li, T. Luchko, R. Luo, B. Madej, K.M. Merz, G. Monard, P. Needham, H. Nguyen, H.T. Nguyen, I. Omelyan, A. Onufriev, D.R. Roe, A. Roitberg, R. Salomon-Ferrer, C.L. Simmerling, W. Smith, J. Swails, R.C. Walker, J. Wang, R.M. Wolf, X. Wu, D.M. York and P.A. Kollman. AMBER 2015. University of California, San Francisco; 2015.

4. PEGylated Bolaamphiphiles with Enhanced Retention in Liposomes

[This work is under revision for publication in Journal of Colloid and Interface Science, under the title "Synthesis and Characterization of PEGylated Bolaamphiphiles with Enhanced Retention in Liposomes. Evan Mintzer and Kathryn E. Uhrich are co-authors for this work.]

4.1. Introduction

Liposomes are spherical, enclosed bilayers primarily composed of phospholipids. They have received extensive attention as a promising class of localized drug delivery vehicles that can effectively reduce drug toxicity and increase drug accumulation at pathological sites [1-4]. In addition, liposomes can be utilized to encapsulate both hydrophobic and hydrophilic drugs, in the lipid bilayer and internal aqueous compartment respectively, as biocompatible drug carriers [5]. However, poor colloidal stability (i.e., liposome aggregation) and biological stability (i.e., fast elimination from blood circulation) may hamper their wider application as drug delivery systems [6-8].

The formulation of sterically stabilized liposomes, which were coated with poly(ethylene glycol) (PEG), drastically extended their circulation half-life in blood [9, 10]. The flexible PEG segments form a hydrophilic spatial barrier that prevents both particle aggregation *in vitro* and serum protein adsorption, both of which cause fast blood clearance by the reticuloendothelial system (RES) [6, 11, 12]. While surface modification of liposomes with PEG can be achieved in different ways, the most widely used approach is to incorporate PEGylated phospholipids such as phosphatidylethanolamine (PE) (e.g., N-(Carbonyl-methoxypolyethyleneglycol)-1,2-dipalmitoyl-*sn*-glycero-3-phosphoethanolamine, PEG-DPPE, **Figure 4.1**A) during liposome preparation. The lipid

portion of PEG-PEs is embedded within the hydrophobic domain of the lipid bilayers as an anchor, with the PEG portion effectively extending to the aqueous bulk solution [6]. As the PEG head group has a much larger size than the hydrophobic acyl moiety, PEG-PEs have superior water-solubility compared to unmodified phospholipids, resulting in diffusion from lipid bilayers upon dilution [13-15]. This dissociation behavior seriously undermines the integrity and stabilizing effects of the PEG coating [15].

Alternatively, bolaamphiphiles (bolas) could be used to synthesize PEGylated bolas (PEG-bolas, **Figure 4.1**A) with improved retention in the lipid bilayer due to their special geometry, which may ultimately increase the longevity of the PEG coating on the liposome surface. Bolas have two polar head groups connected by one or two long alkyl chain spacers. As an example, archaebacteria have membranes rich in bolas and are found to show superior membrane integrity towards harsh conditions compared to conventional phospholipids [16, 17]. The unusual stability of the archaebacteria membrane was attributed to the bolas that extend completely across the membrane and act as "rivets" to keep the membrane bilayer intact. This property can be attributed to the high activation barrier against pulling the inner hydrophilic end groups translocating through the membrane's hydrophobic interior [18, 19]. Despite these desirable properties, use of bolas has been limited as it is difficult to isolate bolas from natural membranes in large quantities; synthetic bola mimics are therefore desired [17, 20].

To synthesize PEG-bolas (**Figure 4.1**B), amphiphilic macromolecules (AMs) with structural similarity to PEGylated lipids were used as the key building blocks. Previously, Tao *et al.* successfully demonstrated AM's ability to stabilize liposomes compared to conventional PEG-DPPE, with improved synthetic efficiency [21]. As such, PEG-bolas

were synthesized by coupling two AM molecules through their free carboxylic acid groups (**Figure 4.2**). To promote the membrane-spanning orientation in liposomal membranes over U-shaped conformation (**Figure 4.1**C), rigid aromatic groups including benzene (BZ) and biphenyl (BP) were introduced between the hydrophobic domains of AMs for PEG-bolas (**Figure 4.2**) [19, 22]. In addition, the lengths of alkyl chains connecting AMs were varied to match the thickness of model 1,2-dipalmitoylphosphatidylcholine (DPPC) liposomes lipid bilayers. PEG-bolas with sufficiently long hydrophobic domains were hypothesized to preferentially span the DPPC lipid bilayer with firm association. To test the feasibility of using liposomes stabilized by PEG-bolas as drug carriers, the colloidal and biological stability were systematically evaluated.

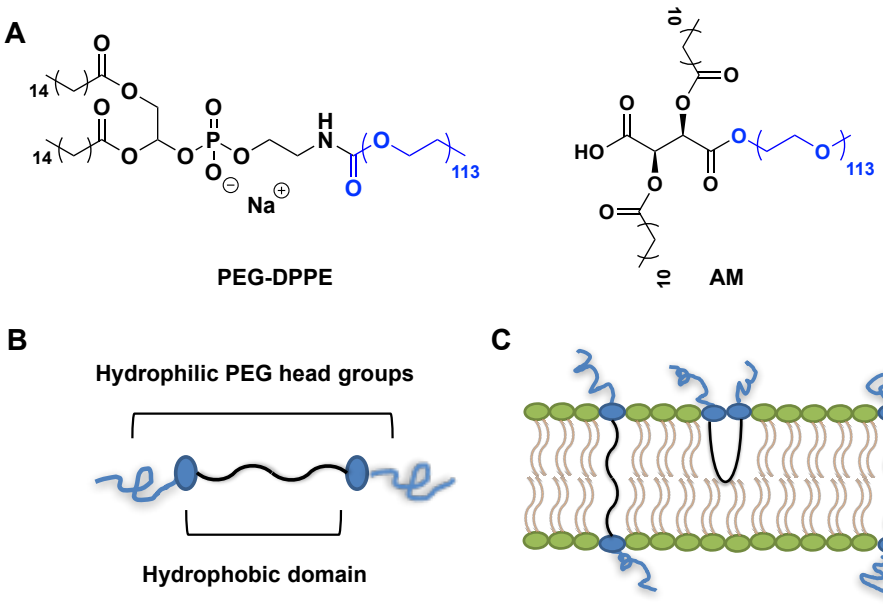

Figure 4.1. Representative chemical structures of PEG-DPPE and AM (A). Schematic illustration of PEG-bolas (B), which have two potential conformations in the lipid bilayer, U-shaped and membrane-spanning (C).

4.2. Results and Discussion

4.2.1. PEG-bolas Synthesis and Characterization

The primary goal of this work was to design and synthesize PEG-bolas that could effectively span lipid bilayers, which was accomplished by coupling two AMs together with a hydrophobic domain as shown in **Figure 4.2**. As only bolas with sufficiently long hydrophobic domains (i.e., molecular length of bolas' hydrophobic portion close to membrane thickness) can extend across membrane [22], diaminoalkanes with varying alkyl chain lengths (C10 and C12) were used as building blocks. In addition, central rigid groups (i.e., phenyl and biphenyl) were introduced into PEG-bolas' hydrophobic domains to promote a membrane-spanning conformation over a U-shaped conformation [19, 22].

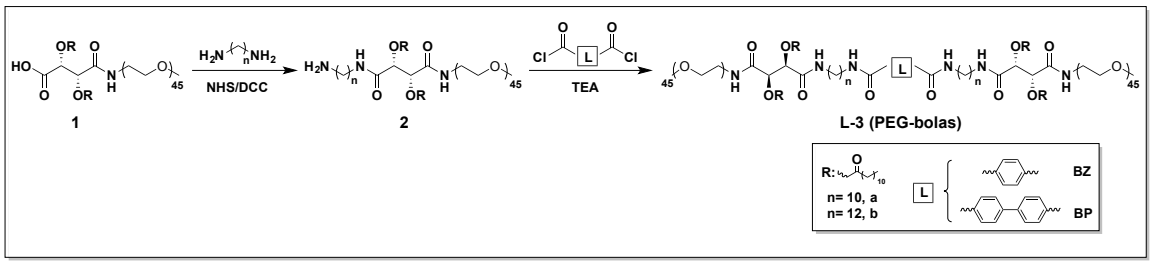

Figure 4.2. Synthetic scheme of PEG-bolas **L-3**.

To ensure monocoupling of **1**, diaminoalkane was used in large excess amount (6 eq.) and N-hydroxysuccinimide (NHS)-activated **1** (1 eq.) was added slowly with diluted concentration. The chemical structure of amine-terminated **2** was confirmed by ^{1}H NMR, as indicated by the appearance of methylene next to the amine at ~ 3.2 ppm, while GPC was used to assess molecular weight and verify the monoconjugation of diaminoalkane. To synthesize PEG-bolas (**L-3**), 2 eq. of **2** was reacted with 1 eq. of acyl chlorides of aromatic

central linkers in the presence of TEA. The appearance of aromatic peaks (7.5 – 8.5 ppm) together with a roughly two-fold molecular weight increase corroborated the successful synthesis of **L-3**, and narrow polydispersities (PDI < 1.3) indicated the complete conversion of the reaction.

4.2.2. Monolayer Study

The behavior of four different PEG-bolas at the air/water interface was studied to shed light on their preferential conformations [21, 23]. Initially, the surface pressure of PEG-bola monolayers gradually increased over a relatively large surface area with compression (i.e., reduction of area per molecule), which was considered to be a process to compress the entangled PEG chains [13]. The following steep increase in surface pressure was observed at 360 $Å^2$/molecule from BZ-linked PEG-bolas with 650 $Å^2$ and 1250 $Å^2$ noted for **BP-3a** and **BP-3b**, respectively. This change indicated the phase transition from expanded liquid phase to compressed solid phase. For PEG-bolas based on a phenyl linker with two PEG segments (2 kDa), their molecular areas were less than 2-fold smaller than that of PEGylated lipids with the same molecular weight (260 $Å^2$) [13]. Thus, it is possible these components are not sufficiently rigid and can adopt bent-shaped (i.e., U-shaped) conformations where PEG chains are compressed to form a condensed structure. In contrast, BP-based PEG-bolas had molecular areas larger than 520 $Å^2$ as mentioned above. These differences are likely due to their long hydrophobic domains in extended conformation conferred by the rigid biphenyl linker, such that molecular area is not limited by the maximum cross-sectional area of the PEG chain.

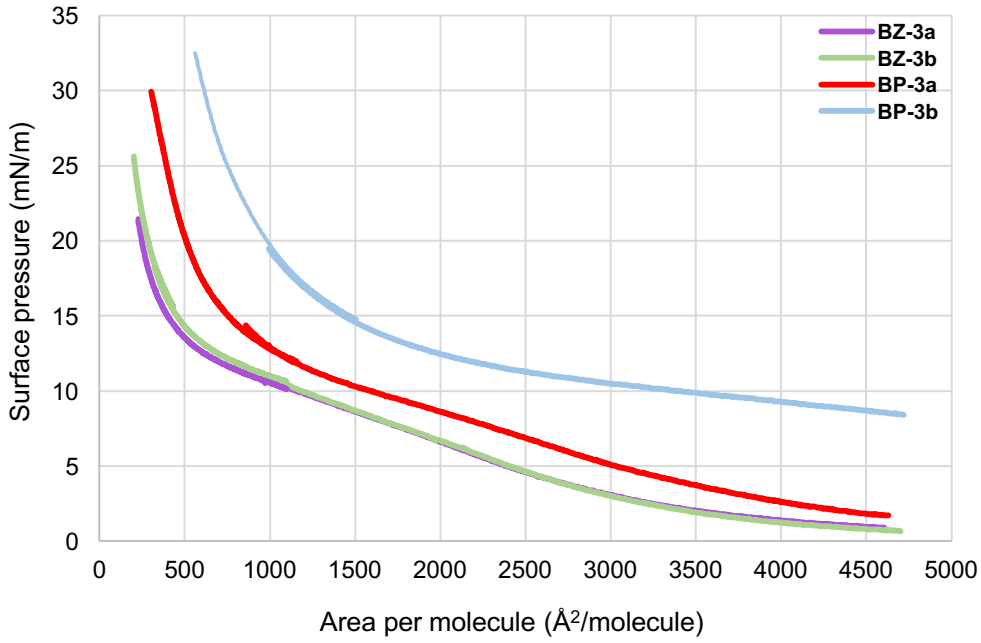

Figure 4.3. π – A isotherms of PEG-bola monolayers at the air/water interface (curves are composites measured using low-to-high surface concentrations of PEG-bolas).

4.2.3. Liposome Colloidal Stability

PEG-bolas were then incorporated into DPPC liposomes as stabilizing agents. Retaining uniform liposome sizes upon storage is crucial in developing robust drug delivery vehicles as an increase in particle size (> 200 nm) generally results in rapid capture by RES *in vivo* with reduced circulation time and altered biodistribution [24]. In addition, liposome aggregation can cause premature drug release and compromise delivery efficiency [25]. Therefore, the colloidal stability of DPPC liposomes stabilized by PEG-bolas was evaluated for up to 8 weeks by DLS. Furthermore, the influence of PEG-bolas' structural parameters on their liposome-stabilizing effects was established.

DPPC liposomes with or without varied mol% of PEG-bolas (2%, 4%, 6%) were prepared systematically via a well-established film-extrusion method [21]. The highest incorporation ratio was kept under 8% to avoid potential phase separation of the liposome membrane or micelle formation [6, 26]. The incorporation of PEG-bolas at different mol% had marginal influence on their particle sizes as shown in **Figure 4.4**A. While all fresh formulations displayed particle sizes between 150 – 165 nm, liposomes with more than 2% of PEG-bolas resulted in slightly larger sizes. The visual turbidity of samples coupled with TEM images ascertained the successful preparation of uniform LUVs.

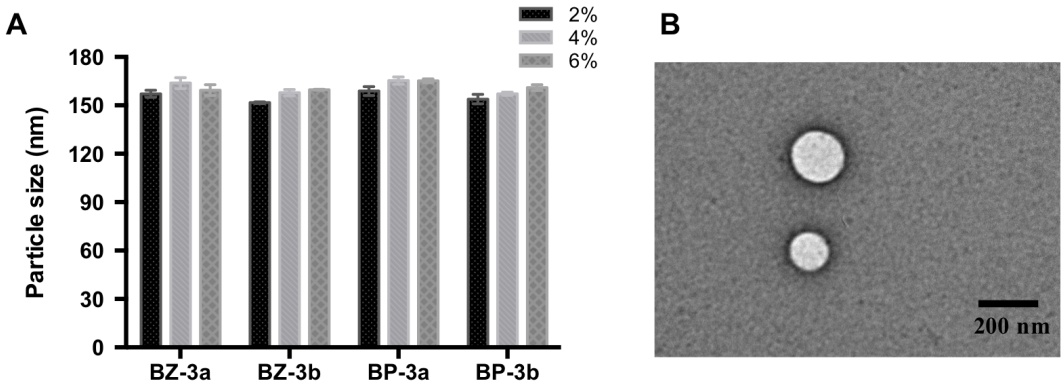

Figure 4.4. Particle sizes of freshly prepared DPPC liposomes stabilized by different ratios of **3-L** (A) and representative TEM images of DPPC liposomes stabilized with **BP-3b** at 6% (B).

To compare the physical stability of liposomes made from different PEG-bolas, the liposomes were stored at refrigeration temperature (4 ˚C), room temperature (25 ˚C), and physiological temperature (37 ˚C) respectively, and their particle sizes as a function of storage time was monitored. The liposome-stabilizing effects of PEG-bolas were compared

to the commercially available PEGylated lipid PEG-DPPE [27, 28]. At 4 ˚C, all PEG-bolas stabilized formulations, except for ones stabilized by **BZ-3a**, exhibited comparable stability to control PEG-DPPE (data not shown). Size increased less than 6% for up to 8 weeks. At this storage temperature, even 2% stabilizing agent provided sufficient steric stabilization to prevent appreciable particle aggregation and fusion.

In contrast, at physiological temperature, liposome size changed to varying degrees for different formulations. For example, liposomes stabilized by 6% **BZ-3a** and **BP-3a**, which were comprised of decacyl chains, experienced notable size differences by 8 weeks (**Figure 4.5**). In particular, the size rapidly increased from 164 nm to 179 nm after 1 week and eventually grew to 230 nm by week 8 for **BZ-3a**, whereas no considerable size increase happened until week 4 for **BP-3a**. Similar to control PEG-DPPE, sizes of liposomes stabilized by **BZ-3b** and **BP-3b** remained constant in the experiment, which is highly desirable for delivery systems. Collectively, the results suggested both alkyl lengths and central linker types had substantial influences on PEG-bolas' stabilizing efficiency; PEG-bolas comprised of dodecyl chains and/or biphenyl linker exhibited better stabilizing effects. Similar trends were also observed at room temperature.

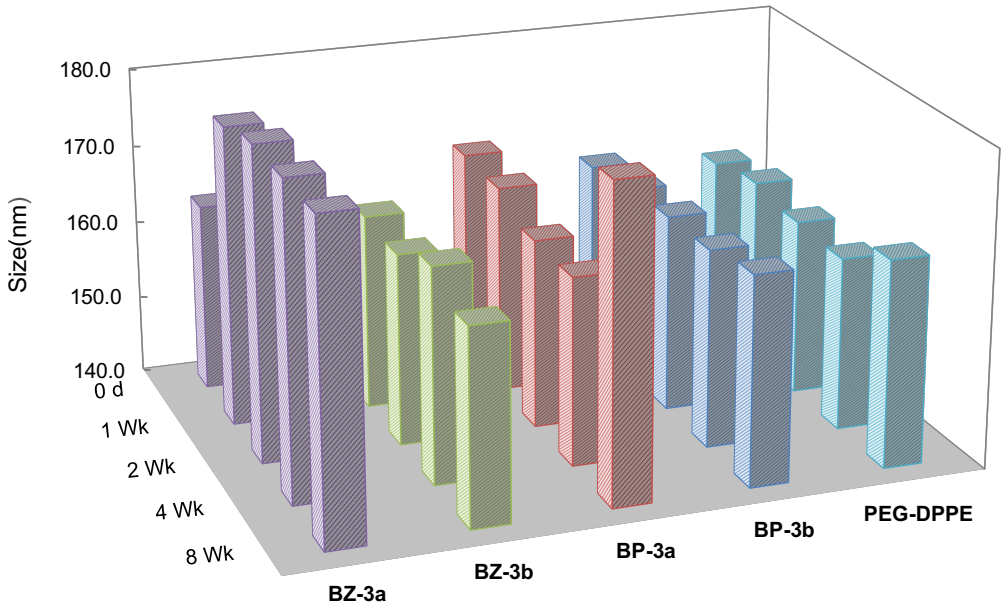

Figure 4.5. Particle sizes of DPPC liposomes stabilized by 6% PEG-bolas or PEG-DPPE upon storage at 37 ˚C for 8 weeks.

4.2.4. Retention of PEG-bolas in Liposomes Upon Dilution

The dissociation behavior of PEGylated lipids from liposomal membranes upon drastic dilution (i.e., systemic administration) severely compromises the integrity of PEG coatings on liposome surfaces, negatively impacting their performance *in vivo* [13-15]. As such, the retention of PEG-bolas was studied using DPPC liposomes with 2% PEG-bolas**,** and the incorporation ratio was examined before and after 10-fold dilution with buffer following literature procedures [13], which mimics extensive dilution. This low incorporation ratio could minimize the PEG chain-chain entanglement on the liposome surface, and thus better reflect the strength of interactions between PEG-bolas and lipid

bilayers [6, 29]. Due to the poor colloidal stability of liposomes stabilized by **BZ-3a**, this compound was not further investigated.

As shown in **Figure 4.6**A, the methylene proton of PEG was well resolved from choline methyl proton of DPPC; thus, their relative ratio was used to calculate the incorporation ratio, normalized to 100% at time zero, and presented as % polymer retention (**Figure 4.6**B). Upon 10-fold dilution, PEG-DPPE experienced a 10% instant loss at 4 h while negligible dissociation was observed for all PEG-bolas. By 48 h, only 83% of PEG-DPPE remained embedded within DPPC liposomes. This effect is consistent with data reported by Tao *et al.* as PEGylated lipids with small hydrophobic domains suffer from poor retention on dilution [21]. In contrast, PEG-bolas exhibited enhanced retention in lipid bilayer and underwent much slower dissociation. Specifically, **BP-3b** with a dodecyl chain and biphenyl linker maintained the highest incorporation ratio (94%) over 48 h, highlighting its promise as a liposome stabilizing agent for use *in vivo*. It is plausible that the PEG-bolas with biphenyl linkers are more likely to adopt membrane-spanning conformation and dodecyl chain provides a longer hydrophobic domain that fits better within the DPPC lipid bilayer.

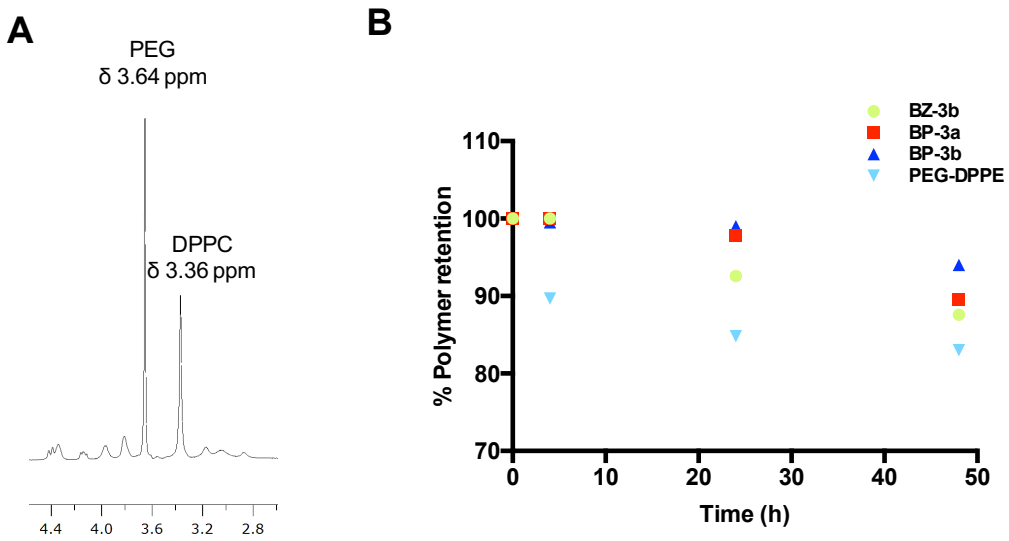

Figure 4.6. ^{1}H NMR spectrum of **BP-3b** in DPPC liposomes with peaks used for incorporation ratio estimation (A). Retention of polymers incorporated at 2% in DPPC liposomes after 10-fold dilution with HEPES buffer (B).

4.2.5. Biological Stability of Liposomes

Surface modification with PEG is a commonly used approach to provide steric protection of liposomes, preventing serum protein absorption and prolonging their circulation time [30]. The protective PEG layer can minimize the interaction between opsonins and liposomes, which impedes the fast blood clearance by the RES [7, 8]. To test the feasibility of using PEG-bolas stabilized liposomes as long-circulating drug carriers, their evasion of the immune response was investigated *in vitro* in the presence of 10% FBS via uptake by macrophages, which are the primary cell types responsible for particle recognition in the RES.

The aggregation and precipitation of DPPC liposomes alone (i.e., free of stabilizing agents) occurred within a few hours after fresh preparation, so cholesterol (CHO, 30 mol%)

was added to the formulations and DPPC/CHO with fluorescently labeled Rh-PE was tested as a control. The uptake of liposomes by macrophages was visualized by fluorescence microscopy. Compared to control liposomes without stabilizing agent (**Figure 4.7**A), DPPC/CHO with 6% PEG-DPPE or **BP-3b** demonstrated significantly less uptake by macrophages (**Figure 4.7**B and C). The uptake was further quantified by flow cytometry and determined as geometric fluorescence intensity (not shown). Introduction of either PEG-DPPE or PEG-bolas resulted in reduction of macrophage uptake by more than 4 fold, indicating their highly improved biological stability.

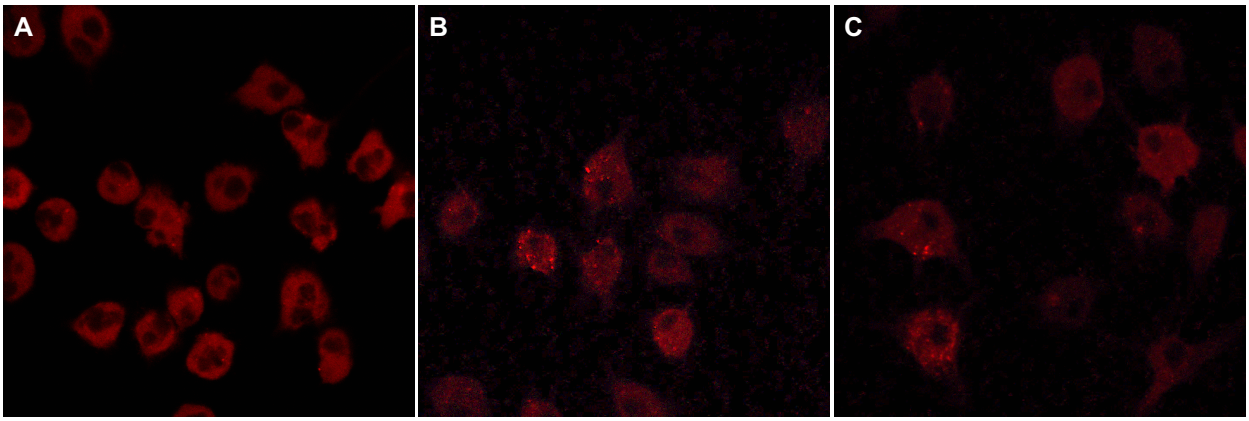

Figure 4.7. Fluorescent images of HMDMs showing uptake of liposomes labeled with 0.2% Rh-PE after 5 h incubation. Control DPPC/CHO (A) and DPPC/CHO stabilized with 6% PEG-DPPE (B) and **BP-3b** (C).

4.3. Conclusion

In this work, a series of novel materials, PEG-bolas were successfully synthesized as PEGylated lipid alternatives to stabilizing liposomes. The colloidal stability of DPPC liposomes stabilized with various PEG-bolas, coupled with their retention ability, implies

that both a central rigid core and the alkyl chain length had substantial influences on their potential as liposome stabilizing agents. **BP-3b** with a dibenzyl linker and dodecyl chain was identified as a lead compound; it demonstrated significantly improved retention in liposomes, provided sufficient steric protection to prevent liposome aggregation, and avoided macrophage uptake compared to commercial standard PEG-DPPE. Currently, PEG-bolas stabilized liposomes are under evaluation as an anticancer drug carrier and will be reported in future work.

4.4. Experimental

4.4.1. Materials

All reagents and solvents were purchased from Sigma-Aldrich (Milwaukee, WI) and used as received unless otherwise indicated. DPPC and 1,2-dipalmitoyl-*sn*-glycero-3-phosphoethanolamine-N-[methoxy(polyethylene glycol)-5000] (sodium salt, PEG-DPPE) were purchased from Avanti Polar Lipids (Alabaster, AL). Lissamine™ rhodamine B 1,2 dihexadecanoyl-*sn*-glycero-3-phosphoethanolamine (triethylammonium salt, Rh-PE) was purchased from Molecular Probes, Inc. (Eugene, OR). Uranyl acetate was purchased from Electron Microscopy Sciences (Hatfield, PA). Polytetrafluoroethylene (PTFE) syringe filters were purchased from Fisher Scientific (Fair Lawn, NJ). RPMI 1640 media was purchased from ATCC (Manassas, VA).

4.4.2. Characterization

Proton (^{1}H) nuclear magnetic resonance (NMR) spectra were recorded on a Varian 400 MHz spectrophotometer. Samples (~ 5 mg/mL) were dissolved in deuterated

chloroform ($CDCl_3$) with trimethylsilane (TMS) as an internal reference. The average weight (M_w) and polydispersity indices (PDI) of PEG-bolas and their precursors were determined by gel permeation chromatography (GPC) using a Waters LC system (Milford, MA) equipped with a PLgel MIXED column (Agilent, Santa Clara, CA). Samples were dissolved at 10 mg/mL in high performance liquid chromatography (HPLC) grade dichloromethane (DCM) and filtered through 0.45 μm PTFE syringe filters prior to injection at a flow rate of 1.0 mL/min. WaterBreeze v3.20 software was used for data collection and processed against a calibration curve derived from broad molecular weight PEG standards (Waters, Milford, MA).

4.4.3. Synthesis

Polymer **1** was prepared as previously published using 2 kDa PEG.[31]

*Synthesis of **2***. Using **2a** as an example, **1** (100 mg, 0.040 mmol) and hydroxyl succinimide (NHS, 5.0 mg, 0.044 mmol) were dissolved in 2 mL anhydrous DCM and 0.2 mL anhydrous dimethyformamide. *N,N*'-Dicyclohexylcarbodiimide (DCC, 1 M in DCM, 0.044 mL) was added dropwise under argon and the reaction stirred for 1 h. In a separate flask, 1,10-diaminodecane (42 mg, 0.24 mmol) was suspended in 0.2 mL DMF and NHS-activated **1** prepared *in situ* was added via a syringe pump at 1.0 mL/h. The reaction was then allowed to stir for an additional 24 h. The reaction mixture was cooled to -20 ˚C to remove the insoluble side product dicyclohexylurea (DCU) via vacuum filtration. The filtrate was washed with 0.1 N HCl (2 × 15 mL), saturated sodium bicarbonate (2 × 15 mL), and brine (2 × 20 mL). The combined organic layers were dried over magnesium sulfate ($MgSO_4$), filtered, and concentrated *in vacuo*. The crude product was purified by

precipitation into chilled diethyl ether (3 × 15 mL) and isolated via centrifugation at 3500 rpm for 5 min (Hettich EBA 12, Beverly, MA).

2a. Yield: 91 mg, 88% (white powder). ^{1}H-NMR (400 MHz, $CDCl_3$): δ 6.67 (br, 1H), 6.08 (br, 1H), 5.64 (dd, 2H) 3.58 (br, ~ 180 H), 3.31 (s, 3H), 3.16 (m, 2H), 2.92 (m, 2H), 2.34 (m, 4H), 1. 61 (m, 4H), 1.42 (m, 4H), 1.18 (br, 44H), 0.81 (t, 6H). M_w, 2.6 kDa; PDI, 1.1.

2b. Yield: 200 mg, 94% (white powder). ^{1}H-NMR (400 MHz, $CDCl_3$): δ 6.64 (br, 1H), 6.10 (br, 1H), 5.60 (dd, 2H) 3.64 (br, ~ 180 H), 3.38 (s, 3H), 3.20 (m, 2H), 2.93 (m, 2H), 2.39 (m, 4H), 1. 61 (m, 4H), 1.41 (m, 4H), 1.25 (br, 48H), 0.88 (t, 6H). M_w, 2.6 kDa; PDI, 1.1.

*Synthesis of **3***. Using **BZ-3a** as an example, **2a** (81mg, 0.030 mmol) and terephthaloyl chloride (3.0 mg, 0.015 mmol) were suspended in 2 mL anhydrous DCM. Triethylamine (TEA, 8.4 μL, 0.06 mmol) was added, and the reaction stirred overnight. The reaction mixture was washed with 0.1 N HCl (2 × 10 mL), saturated sodium bicarbonate (2 × 15 mL), and brine (2 × 20 mL). The crude product was purified by precipitation into chilled diethyl ether (3 × 15 mL) and isolated via centrifugation at 3500 rpm for 5 min (Hettich EBA 12, Beverly, MA). The product was further purified by placing in a Spectra/Por® dialysis tubing (molecular weight cutoff, MWCO 3.5 kDa, Spectrum Laboratories, Inc., Compton, CA) and dialyzing against deionized water for 48 h. The dialyzed solution was then lyophilized to obtain pure **L-3**.

BZ-3a. Yield: 65 mg, 81% (white powder). ^{1}H-NMR (400 MHz, $CDCl_3$): δ 8.11 (br, 2H), 7.84 (s, 4H), 6.86 (br, 2H), 6.22 (br, 2H), 5.60 (dd, 4H) 3.55 (br, ~ 360 H), 3.38

(s, 6H), 3.23 (m, 8H), 2.39 (m, 4H), 1. 63 (m, 8H), 1.48 (m, 8H), 1.25 (br, 76H), 0.88 (t, 12H). M_w, 6.6 kDa; PDI, 1.2.

BZ-3b. Yield: 46 mg, 81% (white powder). ^{1}H-NMR (400 MHz, $CDCl_3$): δ 8.11 (br, 2H), 7.83 (s, 4H), 6.72 (br, 2H), 6.13 (br, 2H), 5.61 (dd, 4H) 3.55 (br, ~ 360 H), 3.38 (s, 6H), 3.23 (m, 8H), 2.40 (m, 4H), 1. 63 (m, 8H), 1.48 (m, 8H), 1.26 (br, 80H), 0.88 (t, 12H). M_w, 6.5 kDa; PDI, 1.3.

BP-3a. Yield: 63 mg, 72% (white powder). ^{1}H-NMR (400 MHz, $CDCl_3$): δ 8.09 (d, 2H), 7.80 (d, 2H), 7.62 (m, 4H), 6.66 (br, 2H), 6.12 (br, 2H), 5.54 (dd, 4H) 3.58 (br, ~ 360 H), 3.31 (s, 6H), 3.16 (m, 8H), 2.33 (m, 4H), 1. 54 (m, 8H), 1.42 (m, 8H), 1.19 (br, 76H), 0.81 (t, 12H). M_w, 6.6 kDa; PDI, 1.1.

BP-3b. Yield: 146 mg, 80% (white powder). ^{1}H-NMR (400 MHz, $CDCl_3$): δ 8.09 (d, 2H), 7.81 (d, 2H), 7.65 (m, 4H), 6.68 (br, 2H), 6.06 (br, 2H), 5.54 (dd, 4H) 3.59 (br, ~ 360 H), 3.31 (s, 6H), 3.16 (m, 8H), 2.33 (m, 4H), 1. 56 (m, 8H), 1.40 (m, 8H), 1.19 (br, 80H), 0.83 (t, 12H). M_w, 6.7 kDa; PDI, 1.1.

4.4.4. Langmuir Monolayers

The surface pressure (π)- area (A) isotherms of PEG-bolas were obtained using a Langmuir surface balance from KSV-Nima (Espoo, Finland) on a subphase of ultra-pure water (resistivity ≥ 18.2 MΩ·cm) at ambient temperature (~ 25 ˚C). PEG-bolas were dissolved in HPLC grade chloroform at 1 mg/mL. For all experiments, the Teflon trough (Biolin Scientific, MD) and barriers were cleaned with chloroform and rinsed thoroughly with ultra-pure water. The subphase surface was cleaned by aspirating during repeated sweeps of the computer-controlled barriers until negligible π changes were observed. PEG-

bolas were spread onto the subphase surface using a digital high precision Hamilton syringe (Reno, NV). After a 10 min delay to allow for complete solvent evaporation, the films were compressed at a rate of 10 mm/min. The surface pressure π was monitored following a Wilhelmy-plate method using a filter paper connected to an electrobalance. Data were collected by KSV-Nima's LB Control software (v. 3.60).

4.4.5. Liposome Preparation

Liposomes were prepared via a film-extrusion method adapted from established procedures.[21] Briefly, PEG-bolas and DPPC lipids were co-dissolved in chloroform at desired molar ratios (0%, 2%, 4%, 6%), and the solvent removed *in vacuo*. When necessary, cholesterol (CHO) and Rh-PE was included in this step at 30% and 0.2% respectively. The mixtures were further dried under high vacuum overnight. To the dried lipid film, 4-(2-hydroxyethyl)-1-piperazineethanesulfonic acid (HEPES) buffer (10 mM, pH adjusted to 7.4 with 0.1 M NaOH) was added to hydrate and resuspend the lipids at 60 ˚C. The hydrated lipid films were subjected to five freeze-thaw cycles, freezing in dry ice (-78 ˚C) and heating in water bath (60 ˚C) alternatively. Large unilamellar vesicles (LUV) were prepared by extruding 15 times through a 100 nm polycarbonate membrane (Sigma-Aldrich, Milwaukee, WI)) using an Avanti Mini-Extruder (Avanti Polar Lipids, Alabaster, AL) at ~ 56 ˚C.

4.4.6. Liposome Morphology and Size

Liposomes were visualized by transmission electron microscopy (TEM) with negative staining. A drop of the liposome suspension (~ 0.1 mg/mL) was deposited onto

on a carbon film-coated copper grid. After 60 seconds, excess solution was removed by tapping the edge of grid with filter paper. A drop of 1% uranyl acetate solution was then applied to the same grid for 60 seconds. The grid was again tapped dry and further dried in the desiccator overnight. Images were taken on JEOL 1200EX electron microscope (JOEL USA, Inc, Pleasanton, MA). Liposome particle sizes and PDI were assessed by dynamic light scattering (DLS) using a NanoZS90 instrument (Malvern Instruments, Southboro, MA) at room temperature. Each sample was run at a 90˚ scattering angle in triplicate with 30 measurements per run.

The colloidal stability of various liposome formulations was studied at 4 ˚C, room temperature, and 37 ˚C for up to 8 weeks. The particle size and PDI of liposomes were monitored by DLS at predetermined time points. Results were analyzed by multiple comparison with two-way ANOVA using built-in statistical analysis function of Prism 6 (GraphPad Software Inc., La Jolla, CA). Significance criteria assumed a 95% confidence level ($p < 0.05$). Standard deviation is reported in the form of error bars.

4.4.7. Retention of PEG-bolas Upon Dilution

The retention of PEG-bolas in DPPC liposomes upon dilution was investigated by ^{1}H NMR spectroscopy with modified procedures[13, 32]. The study was performed with DPPC liposomes with and without 2 mol% stabilizing agents (i.e., PEG-bolas and PEG-DPPE) at 37 ˚C. Liposome samples (30 mM) were diluted 10 times with HEPES buffer under stirring and transferred into a Slide-A-Lyser cassette (MWCO 20 kDa, ThermoFisher Scientific, Waltham, MA), where the unincorporated PEG-bolas were removed by dialysis against HEPES buffer. An aliquot of diluted liposomes (1.5 mL) was taken at

predetermined time points for up to 48 hours. The samples were lyophilized and then dissolved in $CDCl_3$ for NMR characterization. The ratio of the choline methyl proton of DPPC (~ 3.4 ppm) to the methylene proton of PEG (~ 3.6 ppm) was obtained by ^1H NMR spectroscopy before and after dilution, which correlated to the incorporated ratio of stabilizing agents to lipids in the bilayers. The result was normalized to the initial incorporated ratio and reported as % PEG-bolas retention.

4.4.8. Uptake of PEG-bolas Stabilized DPPC Liposomes by Macrophages

The phagocytic uptake of PEG-bolas stabilized DPPC liposomes was determined with human monocytes derived macrophages (HMDMs). HMDMs were isolated and cultured from human buffy coats (New York Blood Center, Long Island City, NY) as previously published.[33] For fluorescence microscopy, 3.75×10^4 cells were seeded in 8-well Lab-Tek^{TM} and incubated at 37 ˚C for 24 h prior to use. DPPC/CHO liposomes (with or without 6 mol% liposome stabilizing agents) containing 0.2 mol% Rh-PE were suspended in RPMI 1640 media supplemented with 10% fetal bovine serum (FBS) and 1% penicillin/streptomycin at 300 μM and an aliquot (250 μL) was added to designated wells. Following 5 h incubation, the cells were washed with cold phosphate buffered saline (PBS, pH 7.4) three times and fixed with 1% paraformaldehyde before imaging on a Leica TCS SP2 confocal microscope (Leica Microsystems, Buffalo Grove, IL).

4.5. References

[1] Drummond DC, Meyer O, Hong K, Kirpotin DB, Papahadjopoulos D. Optimizing Liposomes for Delivery of Chemotherapeutic Agents to Solid Tumors. Pharmacological Reviews. 1999;51:691-744.

[2] Samad A, Sultana Y, Aqil M. Liposomal drug delivery systems: an update review. Current drug delivery. 2007;4:297-305.

[3] Allen TM, Cullis PR. Liposomal drug delivery systems: From concept to clinical applications. Advanced Drug Delivery Reviews. 2013;65:36-48.

[4] Malam Y, Loizidou M, Seifalian AM. Liposomes and nanoparticles: nanosized vehicles for drug delivery in cancer. Trends in Pharmacological Sciences. 2009;30:592-9.

[5] Khan DR, Rezler EM, Lauer-Fields J, Fields GB. Effects of Drug Hydrophobicity on Liposomal Stability. Chemical Biology & Drug Design. 2008;71:3-7.

[6] Bedu-Addo FK, Huang L. Interaction of PEG-phospholipid conjugates with phospholipid: implications in liposomal drug delivery. Advanced Drug Delivery Reviews. 1995;16:235-47.

[7] Ishida T, Harashima H, Kiwada H. Liposome Clearance. Bioscience Reports. 2002;22:197-224.

[8] Yan X, Scherphof GL, Kamps JA. Liposome opsonization. Journal of liposome research. 2005;15:109-39.

[9] Immordino ML, Dosio F, Cattel L. Stealth liposomes: review of the basic science, rationale, and clinical applications, existing and potential. International Journal of Nanomedicine. 2006;1:297-315.

[10] Harrington KJ, Rowlinson-Busza G, Syrigos KN, Uster PS, Vile RG, Stewart JSW. Pegylated Liposomes Have Potential as Vehicles for Intratumoral and Subcutaneous Drug Delivery. Clinical Cancer Research. 2000;6:2528-37.

[11] Du H, Chandaroy P, Hui SW. Grafted poly-(ethylene glycol) on lipid surfaces inhibits protein adsorption and cell adhesion. Biochimica et Biophysica Acta (BBA) - Biomembranes. 1997;1326:236-48.

[12] Yoshioka H. Surface modification of haemoglobin-containing liposomes with polyethylene glycol prevents liposome aggregation in blood plasma. Biomaterials. 1991;12:861-4.

[13] Takeoka S, Mori K, Ohkawa H, Sou K, Tsuchida E. Synthesis and Assembly of Poly(ethylene glycol)−Lipids with Mono-, Di-, and Tetraacyl Chains and a Poly(ethylene glycol) Chain of Various Molecular Weights. Journal of the American Chemical Society. 2000;122:7927-35.

[14] Silvius JR, Zuckermann MJ. Interbilayer transfer of phospholipid-anchored macromolecules via monomer diffusion. Biochemistry. 1993;32:3153-61.

[15] Parr MJ, Ansell SM, Choi LS, Cullis PR. Factors influencing the retention and chemical stability of poly(ethylene glycol)-lipid conjugates incorporated into large unilamellar vesicles. Biochimica et Biophysica Acta (BBA) - Biomembranes. 1994;1195:21-30.

[16] O'Neil EJ, DiVittorio KM, Smith BD. Phosphatidylcholine Derived Bolaamphiphiles via 'Click' Chemistry. Organic letters. 2007;9:199-202.

[17] Popov M, Linder C, Deckelbaum RJ, Grinberg S, Hansen IH, Shaubi E, et al. Cationic vesicles from novel bolaamphiphilic compounds. Journal of liposome research. 2010;20:147-59.

[18] Yan Y, Lu T, Huang J. Recent advances in the mixed systems of bolaamphiphiles and oppositely charged conventional surfactants. Journal of Colloid and Interface Science. 2009;337:1-10.

[19] Forbes CC, DiVittorio KM, Smith BD. Bolaamphiphiles Promote Phospholipid Translocation Across Vesicle Membranes. Journal of the American Chemical Society. 2006;128:9211-8.

[20] Song B, Liu G, Xu R, Yin S, Wang Z, Zhang X. Interfacial Self-Organization of Bolaamphiphiles Bearing Mesogenic Groups: Relationships between the Molecular Structures and Their Self-Organized Morphologies. Langmuir. 2008;24:3734-9.

[21] Tao L, Faig A, Uhrich KE. Liposomal stabilization using a sugar-based, PEGylated amphiphilic macromolecule. Journal of Colloid and Interface Science. 2014;431:112-6.

[22] Yan Y, Xiong W, Huang J, Li Z, Li X, Li N, et al. Organized Assemblies in Bolaamphiphile/Oppositely Charged Conventional Surfactant Mixed Systems. The Journal of Physical Chemistry B. 2005;109:357-64.

[23] Terme N, Jacquemet A, Benvegnu T, Vié V, Lemiègre L. Modification of bipolar lipid conformation at the air/water interface by a single stereochemical variation. Chemistry and Physics of Lipids. 2014;183:9-17.

[24] Litzinger DC, Buiting AMJ, van Rooijen N, Huang L. Effect of liposome size on the circulation time and intraorgan distribution of amphipathic poly(ethylene glycol)-containing liposomes. Biochimica et Biophysica Acta (BBA) - Biomembranes. 1994;1190:99-107.

[25] Deshpande PP, Biswas S, Torchilin VP. Current trends in the use of liposomes for tumor targeting. Nanomedicine (London, England). 2013;8:10.2217/nnm.13.118.

[26] Bedu-Addo FK, Tang P, Xu Y, Huang L. Effects of Polyethyleneglycol Chain Length and Phospholipid Acyl Chain Composition on the Interaction of Polyethyleneglycol-phospholipid Conjugates with Phospholipid: Implications in Liposomal Drug Delivery. Pharmaceutical Research. 1996;13:710-7.

[27] Maruyama K, Yuda T, Okamoto A, Kojima S, Suginaka A, Iwatsuru M. Prolonged circulation time in vivo of large unilamellar liposomes composed of distearoyl phosphatidylcholine and cholesterol containing amphipathic poly (ethylene glycol). Biochimica et Biophysica Acta (BBA)-Lipids and Lipid Metabolism. 1992;1128:44-9.

[28] Crosasso P, Ceruti M, Brusa P, Arpicco S, Dosio F, Cattel L. Preparation, characterization and properties of sterically stabilized paclitaxel-containing liposomes. Journal of Controlled Release. 2000;63:19-30.

[29] Allen C, Dos Santos N, Gallagher R, Chiu GNC, Shu Y, Li WM, et al. Controlling the Physical Behavior and Biological Performance of Liposome Formulations Through Use of Surface Grafted Poly(ethylene Glycol). Bioscience Reports. 2002;22:225-50.

[30] Allen T, Hansen C, Martin F, Redemann C, Yau-Young A. Liposomes containing synthetic lipid derivatives of poly (ethylene glycol) show prolonged circulation half-lives in vivo. Biochimica et Biophysica Acta (BBA)-Biomembranes. 1991;1066:29-36.

[31] Abdelhamid DS, Zhang Y, Lewis DR, Moghe PV, Welsh WJ, Uhrich KE. Tartaric acid-based amphiphilic macromolecules with ether linkages exhibit enhanced repression of oxidized low density lipoprotein uptake. Biomaterials. 2015;53:32-9.

[32] Sou K, Endo T, Takeoka S, Tsuchida E. Poly(ethylene glycol)-Modification of the Phospholipid Vesicles by Using the Spontaneous Incorporation of Poly(ethylene glycol)-Lipid into the Vesicles. Bioconjugate Chemistry. 2000;11:372-9.

[33] Zhang Y, Li Q, Welsh WJ, Moghe PV, Uhrich KE. Micellar and structural stability of nanoscale amphiphilic polymers: Implications for anti-atherosclerotic bioactivity. Biomaterials. 2016;84:230-40.

5. Appendix: Miscellaneous Projects

5.1. Optimization of Ether-linked Amphiphilic Macromolecules Synthesis

Due to compromised anti-atherosclerotic activity of ester-linked amphiphilic macromolecules (AMs) in the presence of enzymes (e.g., lipase), ether-linked AMs were designed and synthesized to improve their degradation stability and bioactivity *in vivo* [1]. However, in the initial synthetic pathway, alkylation dibenzyl *L-tar*trate using NaH suffered from difficulty of purification and extremely low yield (~ 10%), which hampered the further investigation of ether-linked AMs. So, efforts were made to optimize the synthetic pathway through different combinations of base, catalyst and solvent. In addition, alternative substrate other than dibenzyl *L*-tartrate was explored.

5.1.1. Results and Discussion

The low yield of alkylation step of dibenzyl *L*-tartrate is mainly because of the harsh chemical conditions required for ether bond formation, which are not compatible with most carboxylic acid protecting groups (e.g., benzyl). Thus, mild reaction condition with catalyst may address this issue (**Figure 5.1**). The synthesis was first attempted with Ag_2O as catalyst following a modified procedure and the main product purified via column chromatography [2]. Interestingly, based on ^{1}H NMR spectra, disappearance of the methine backbone peak (~ δ 5.7 ppm) coupled with the singlet split pattern of benzyl protons (δ 5.3 ppm) suggested the formation of a symmetric unsaturated compound as indicated in **Figure 5.2** rather than the target product. This result was likely due to the oxidation of alcohol by Ag_2O followed by tautomerization. Thus, an alternative approach using cetyltrimethylammonium (CTAB) as phase-transfer catalysis was investigated to improve

yield of traditional Willamson's as suggested by literature [3]. CTAB forms reverse micelles in organic phase, which solubilizes NaOH in the solid state. As hydroxide ion is a very strong base, it can form alkoxides with alcohol groups thus enabling the reaction with bromoalkane on the reverse micelle. However, this approach still gave low yield (about 11%). Large amount of side product with high polarity was observed from thin layer chromatography (TLC), which was likely the ester hydrolysis product of starting material in the presence of water. Anhydrous conditions should improve the yield.

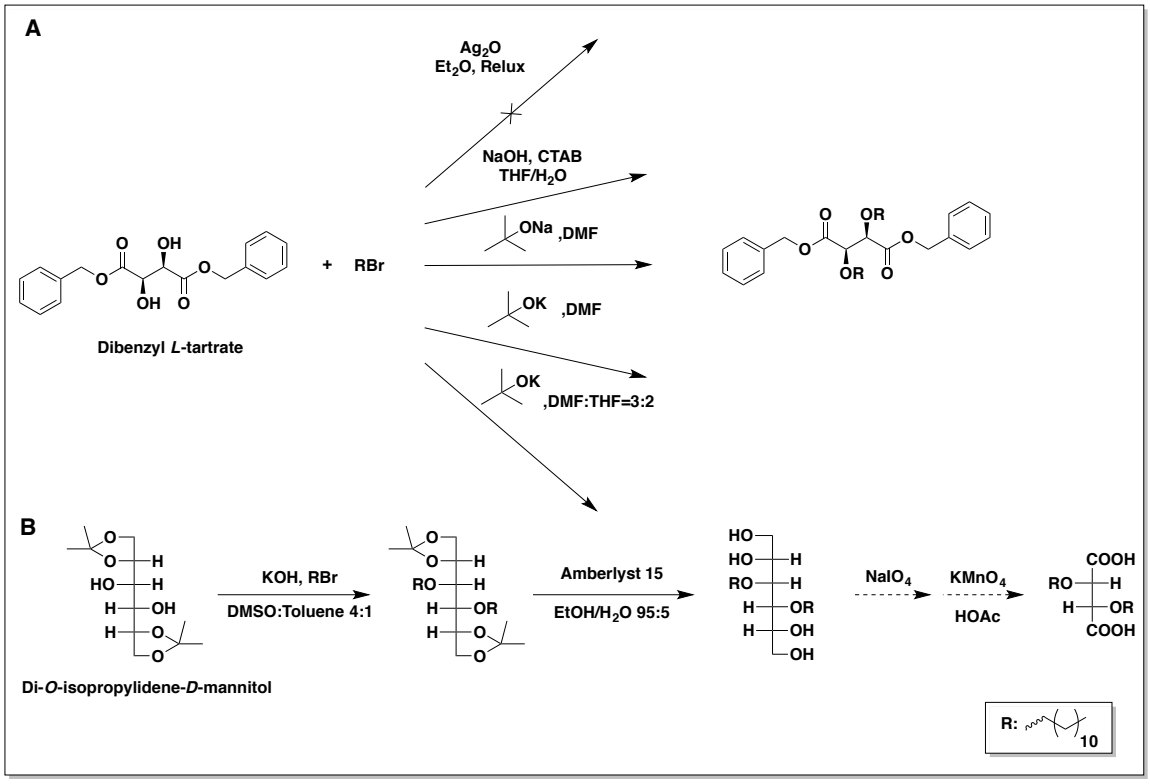

Figure 5.1. Reaction conditions attempted to synthesize ether-linked AM precursors from dibenzyl *L*-tartrate (A) and 1,2:5,6-di-O-isopropylidene-*D*-mannitol (B).

To establish the influence of base and solvent type on the alkylation efficiency, two strong bases sodium (*tert*-butoxide and potassium *tert*-butoxide) were evaluated because of their solubility in organic solvents. These two bulky bases were selected to minimize the deprotonation and alkylation of benzyl protons previously observed with NaH owing to increased steric hindrance. Encouragingly, the yield slightly improved to ~ 18 – 20%. It is worth noting that the alkylation efficiency dropped when the solvent was changed from DMF to a less polar mixture of DMF and THF, implying that the more polar DMF was a better solvent.

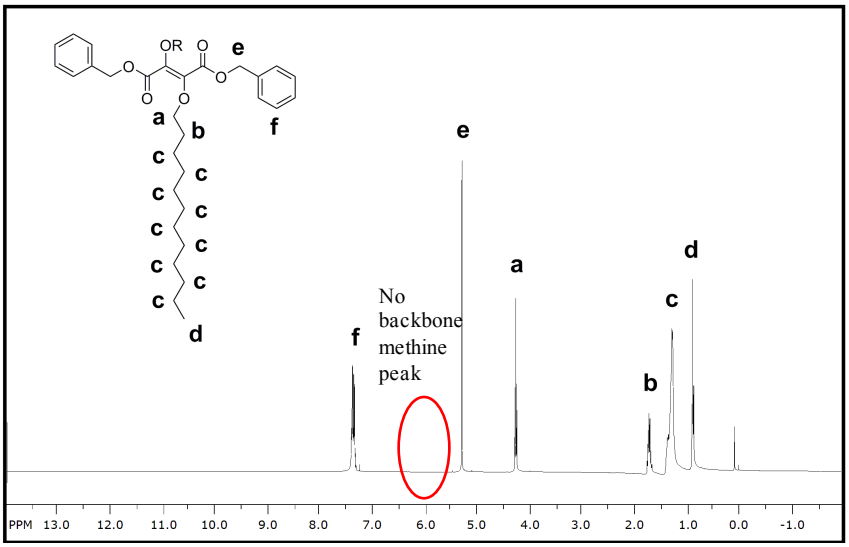

Figure 5.2. ^{1}H NMR spectrum of unsaturated product obtained through refluxing dibenzyl *L*-tartrate with Ag_2O.

The relatively labile benzyl protecting groups in the presence of base may partially attribute to low reaction yields. Thus, more robust protecting groups that cannot be deprotonated were explored. Starting with commercially available 1,2:5,6-Di-O-isopropylidene-*D*-mannitol, alkylation was successful when following published

procedure [4] at 46% yield. The subsequent deprotection of acetonide groups with acidic Amberlyst® resin led to a quantitative yield. However, the attempt to oxidize diol into carboxylic acid yielded no target product; this result was attributed to the poor solubility of hydrophobic intermediate in solvents such as methanol and water, which are required for oxidation.

5.1.2. Experimental

5.1.2.1. Synthesis of dialkylated dibenzyl *L*-tartrate

The experimental procedures of reaction conditions listed in **Figure 4.1**A were provided below in order (from top to bottom).

Following a modified procedure [2], in brief, dibenzyl *L*-tartrate (661mg, 2.0 mmol) and 1-bromododecane (0.99 mL, 4.0 mmol) were dissolved in 10 mL anhydrous diethyl ether and refluxed in the dark. Well-dried Ag_2O (1.07 g, 4.6 mmol) was added to the solution and reaction stirred for 3 days. The detailed characterization of product has been provided in 2.4.3.1.

Following a modified procedure [3], dibenzyl *L*-tartrate (661 mg, 2.0 mmol), 1-bromododecane (0.99 mL, 4.0 mmol), CATB (73 mg, 0.2 mmol), and NaOH (32mg were suspended in 1 mL THF and 0.02 mL H_2O. Insoluble salts were removed by vacuum filtration and the filtrate was dried over $MgSO_4$. The solvent was removed *in vacuo* and crude product was purified on silica gel via column chromatography using a hexane: ethyl acetate gradient (100:0 to 98:2). Yield: 11% (white solid).

5.1.2.2. Synthesis of 3,4-O-didodecyl-1,2:5,6-di-O-isopropylidene-*D*-mannitol

Following published procedure [4], 1,2:5,6-di-O-isopropylidene-*D*-mannitol (508 mg, 1.9 mmol) was dissolved in 5 mL toluene/DMSO (4:1) followed by addition of crushed KOH (435 mg, 7.8 mmol). After stirring for 5 min, 1-bromododecane (1.0 mL, 4.3 mmol) was added and reaction was left stirring overnight. Mixture was filtered, washed with sat. NH_4Cl (7 mL), and extracted with toluene (2x 7 mL). Combined organic layer was dried over $MgSO_4$ and solvent removed *in vacuo*. Crude product was purified on silica gel via column chromatography using a hexane: ethyl acetate (70:30). Yield: 525 mg, 46% (colorless oil). ^{1}H-NMR (400 MHz, $CDCl_3$): 4.18 (q, 2H), 4.07 (m, 2H), 3.94 (m, 2H), 3.58 (m, 4H), 3.51 (d, 2H), 1.55 (m, 4H), 1.40 (s, 6H), 1.34 (s, 6H), 1.26 (br, 36H), 0.88 (t, 6H).

5.1.2.3. Synthesis of 3,4-O-didodecyl-*D*-mannitol

3,4-O-Didodecyl-1,2:5,6-di-O-isopropylidene-*D*-mannitol (524 mg, 0.88 mmol) was dissolved in 5 mL EtOH/H_2O (95:5), and Amberlyst® 15 (877 mg, 1 gmmol^{-1}) was added. The mixture was stirred at 60 °C for 2 days. The resin was filtered off and washed with EtOH (3x 5 mL), and the solvent was removed *in vacuo*. Yield: near quantitative, 436 mg (white solid). ^{1}H-NMR (400 MHz, $CDCl_3$): 3.98 (m, 2H), 3.57 – 3.83 (m, 10H) 1.55 (m, 4H), 1.44 (m, 4H), 1.34 (s, 6H), 1.26 (br, 36H), 0.88 (t, 6H).

5.1.2.4. Synthesis of 2,3-dodecyl-succinaldehyde

Following a modified procedure [5], 3,4-O-didodecyl-*D*-mannitol (41 mg, 0.079 mmol) was suspended in 1.6 mL MeOH/H_2O (3:5) and cooled down to 10 ˚C. Sodium periodate (NaIO4, 19 mg, 0.087 mmol) was added and reaction was stirred for 5 h.

5.1.3. References

[1] Abdelhamid DS, Zhang Y, Lewis DR, Moghe PV, Welsh WJ, Uhrich KE. Tartaric acid-based amphiphilic macromolecules with ether linkages exhibit enhanced repression of oxidized low density lipoprotein uptake. Biomaterials. 2015;53:32-9.

[2] Aurich HG, Biesemeier F. Intramolecular 1, 3-Dipolar cycloaddition of transient enantiomerically pure oxaalkenyl nitrones. Synthesis. 1995:1171-8.

[3] Jursic B. Synthetic application of micellar catalysis. williamson's synthesis of ethers. Tetrahedron. 1988;44:6677-80.

[4] Walton J, Tiddy GJT, Webb SJ. Synthesis and lyotropic phase behavior of novel nonionic surfactants for the crystallization of integral membrane proteins. Tetrahedron Letters. 2006;47:737-41.

[5] Gruner SAW, Truffault V, Voll G, Locardi E, Stöckle M, Kessler H. Design, Synthesis, and NMR Structure of Linear and Cyclic Oligomers Containing Novel Furanoid Sugar Amino Acids. Chemistry – A European Journal. 2002;8:4365-76

5.2. Lipase-catalyzed Hydrolysis of Amphiphilic Macromolecules

[This work is part of publication in Biomaterials, year 2015, volume 53, pages 32-39, under the tile "Tartaric acid-based Amphiphilic Macromolecules with Ether Linkages Exhibit Enhanced Regression of Oxidized Low Density Lipoprotein Uptake" [1]. These paragraphs were originally written by the thesis author]

Susceptibility to esterase hydrolysis is an important consideration in drug design [2]. Ester-linked AMs are vulnerable to esterase-catalyzed hydrolysis and degradation [3], thus suffer from reduced bioavailability during blood circulation given the abundant presence of lipase in human serum [4], leading to compromised bioactivity. As such, it is critical to design AMs with enhanced degradation stability to overcome this potential limitation and exhibit enhanced bioactivity. The degradation stability of lead AMs (**Figure 5.3**), including M12P5, T12P5-*L*, and T(12-O)P5, was examined.

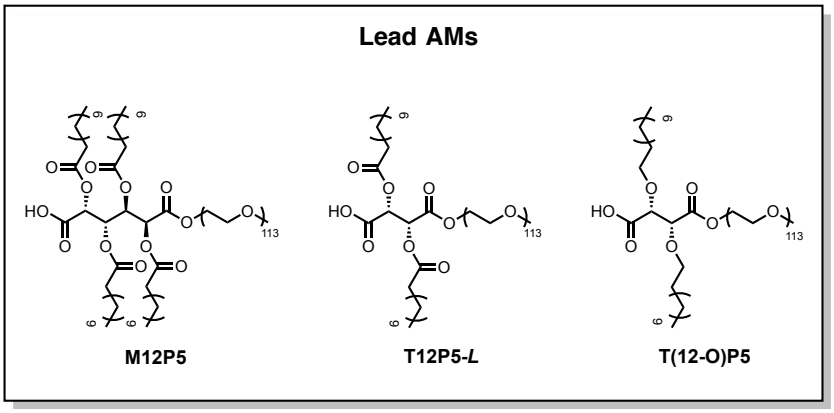

Figure 5.3. Chemical structures of lead AMs with different hydrophobicity and linkage type.

5.2.1. Results and Discussion

As the enzymatic degradation of AMs *in vivo* could significantly alter AM bioavailability and efficiency, the degradation stability of these AMs was carefully examined in the presence of porcine pancreatic lipase by ^{1}H NMR spectroscopy. To understand the influence of linkage types as well as hydrophobicity on the degradation rate of AMs, M12P5, T12P5-L, and T(12-O)P5 were assessed at 37 °C and pH = 7.4 to mimic physiological conditions (**Figure 5.4**). ^{1}H NMR spectroscopy was used to monitor changes in AM chemical structure via the appearance of degradation products. While all three AMs have a hydrolyzable ester bond between the hydrophilic PEG and the hydrophobic segment, compounds T12P5-L and M12P5 also have ester bonds between the alkyl arms and linear backbones in the hydrophobic region. Specifically, the CH_2 of the alkyl chain arms *alpha* to ester carbonyl moieties (2.30 and 2.42 ppm for M12P5, and 2.41 ppm for T12P5-L) and the terminal CH_3 of ether-linked alkyl arms (0.88 ppm for T(12-O)P5) were monitored. For T(12-O)P5, the terminal CH_3 was analyzed instead of the CH_2 of the alkyl

arms *alpha* to the ether linkages due to overlaps between the aforementioned CH_2 signal (~3.6 ppm) and broad PEG peaks (~3.4 – 4.2 ppm). The degradation of M12P5's hydrophobic domain was implied by the appearance of new CH_2 peaks at 2.35 ppm, correlating with hydrolysis of the ester bonds between alkyl arms and the linear backbones, releasing dodecanoic acid. The complete degradation of M12P5 took less than 3 h while complete degradation of T12P5-*L* was longer than 3 h. These observations suggest that M12P5 with a higher level of hydrophobicity interacted more favorably with lipase, leading to an accelerated degradation. A similar observation has been reported for the enzymatic degradation of PEG_{45}-b-PCL_{60} micelles, indicating that more hydrophobic polymers undergo a more rapid degradation [5]. In contrast to both ester-linked AMs, negligible changes were observed for T(12-O)'s terminal CH_3 (0.88 ppm). The absence of a dodecanol degradation product, CH_3 peak at 0.77 ppm, further confirmed the robust stability of AMs with ether linkages in the hydrophobic region. Although T(12-O)P5 exhibited comparable efficiency in reducing oxLDL uptake as M12P5, compound T(12-O)P5 holds more promise for *in vivo* treatment with its resistance to rapid enzymatic degradation.

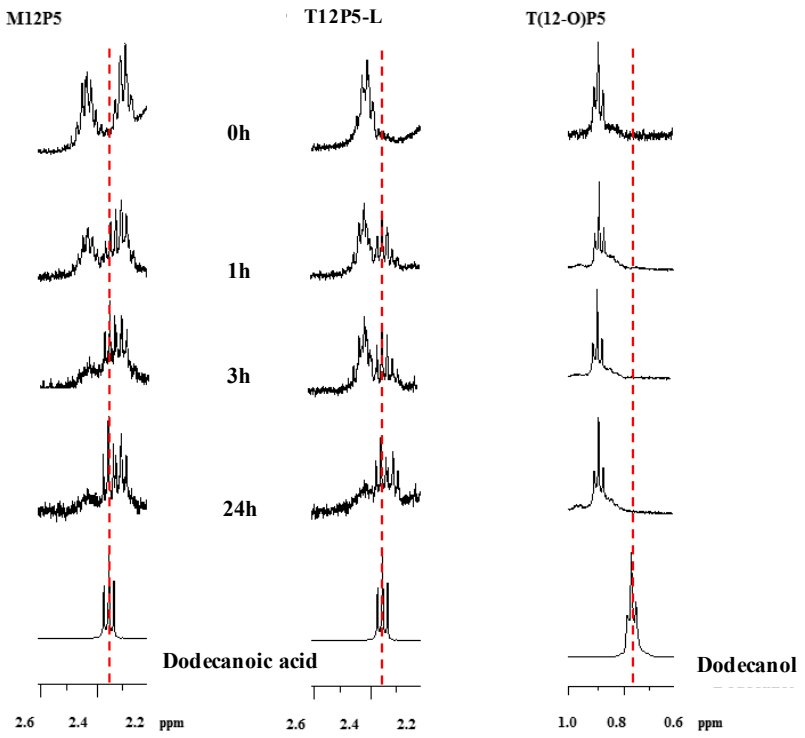

Figure 5.4. Porcine pancreatic lipase catalyzed degradation of ester-linked AMs (M12P5 and T12P5-L) and ether-linked AMs (T(12-O)P5) at an activity of 3 U/mL.

5.2.2. Experimental

5.2.2.1. Lipase-catalyzed hydrolysis and degradation of AM micelles

Lipase-catalyzed degradation experiments were performed in the presence of lipase from porcine pancreas (30 U/mg). AM micelle solutions (3 mg/mL) in PBS (pH = 7.4) were incubated with lipase at 3 U/mL at 37 °C with gentle agitation (60 RPM). 1.5 mL samples were taken at predetermined time points up to 24 h and extracted with DCM (3x 2 mL). DCM was then removed *in vacuo*. The samples were dissolved in $CDCl_3$ and analyzed by ^{1}H NMR for changes in chemical structure.

5.2.3. References

[1] Abdelhamid DS, Zhang Y, Lewis DR, Moghe PV, Welsh WJ, Uhrich KE. Tartaric acid-based amphiphilic macromolecules with ether linkages exhibit enhanced repression of oxidized low density lipoprotein uptake. Biomaterials. 2015;53:32-9.

[2] Casey Laizure S, Herring V, Hu Z, Witbrodt K, Parker RB. The Role of Human Carboxylesterases in Drug Metabolism: Have We Overlooked Their Importance? Pharmacotherapy: The Journal of Human Pharmacology and Drug Therapy. 2013;33:210-22.

[3] Demirdirek B. Synthesis and evaluation of amphiphilic scorpion-like and star macromolecules for biomedical applications: ProQuest; 2009.

[4] Tietz N, Shuey D. Lipase in serum--the elusive enzyme: an overview. Clinical chemistry. 1993;39:746-56.

[5] Zhu X, Fryd M, Wayland BB. Kinetic-mechanistic studies of lipase-polymer micelle binding and catalytic degradation: Enzyme interfacial activation. Polymer Degradation and Stability. 2013;98:1173-81.

5.3. Preparation of Cationic Amphiphiles for Antimicrobial Application with Improved Biocompatibility

Two series of CAms comprised of alkyl hydrophobic arms and cationic ammonium hydrophilic head groups have been shown as promising antimicrobial alternatives with membrane-targeting mechanism. Their biocompatibility was evaluated in terms of hemolytic activity and cytotoxicity. Due to their cationic and hydrophobic nature, while HC_{50} values of identified lead compounds were 11 – 68 fold higher than their MICs, their IC_{50} values were only 2 – 7 fold higher. Thus, to further improve their biocompatibility and suitability for *in vivo* application, two strategies were taken.

Kuroda *et al.* reported synthesis of cationic amphiphilic random copolymers with ethyl methacrylate comonomer and demonstrated that by tuning the length of hydrophobic

spacer (i.e., between hydrophilic group and backbone), maximal antimicrobial potency and minimal hemolysis were obtained with intermediate length [1]. Thus, the hydrophobic spacer was varied for ether-linked CAm, from 2, 4, to 6 carbons. In addition, the cationic charge types could also be varied to optimize the balance between antimicrobial efficiency and cytotoxicity. For example, quaternary ammonimum materials, such as low-molecular-weight compounds [2, 3] and polymers with pendant quaternary ammonium moiety [4, 5], have been widely used as antibacterial agents.

5.3.1. Results and Discussion

To extend the length of hydrophobic spacers, *N*-Boc-1,4-butanediamine and *N*-Boc-1,6-hexanediamine were conjugated to the carboxylic acid groups of ***5.1*** through carbodiimide coupling with high yields, respectively (**Figure 5.5**). Subsequently, the *tert*-butyl groups were deprotected under acidic conditions to afford ***5.3*** as chloride salts. The successful synthesis was confirmed by ^{1}H NMR and ^{13}C NMR spectroscopies. The solubility of ***5.3*** was tested in water and HEPES buffer which was less than the counterpart with shorter space length (2 carbons). This effect was likely due to their enhanced hydrophobicity. Their antimicrobial activity and biocompatibility will be evaluated by broth microdilution assay [6], red blood cells hemolysis assay [7], and MTT cytotoxicity assay [8].

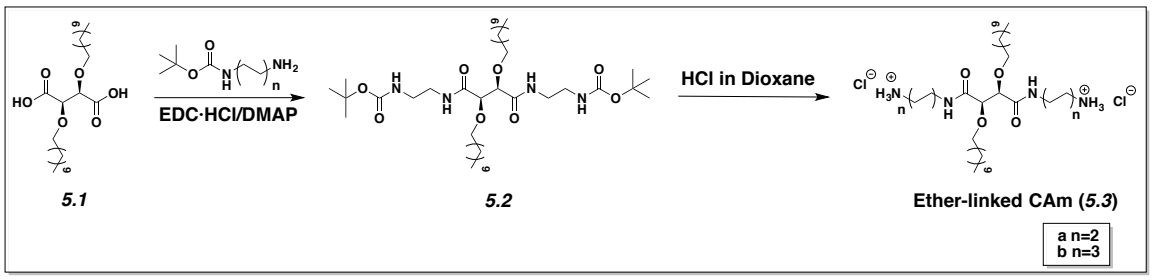

Figure 5.5. Synthesis of ether-linked CAm with extended hydrophobic spacer.

The synthesis of CAm with quaternary ammonium functional group was attempted as described in **Figure 5.6**. As (2-aminoethyl)trimethylammonium chloride hydrochloride had poor solubility in organic solvent such as DCM and DMF, it was suspended in the solution during the reaction. The reaction was monitored by taking aliquot of reaction mixture at different time points and analyzing by MS. While no product was observed at the first 24 h, target molecule MS peak showed up after 48 h and became more prevalent at 72 h (**Figure 5.7**). To purify ***5.5*** in salt form, neutral aluminum oxide column was used directly after solvent removal *in vacuo* as the product stayed in aqueous layer for workup as a result of enhanced water solubility. With no good visualization methods via TLC plate to track tertiary amines, different fractions were characterized by NMR spectroscopy. The fractions containing final product were collected in very low yields (~ 20%). The synthetic yield needs to be optimized and an alternative method with higher yield is desirable. Post-quaternization modification of ***5.3*** containing primary ammonium functionality is one option.

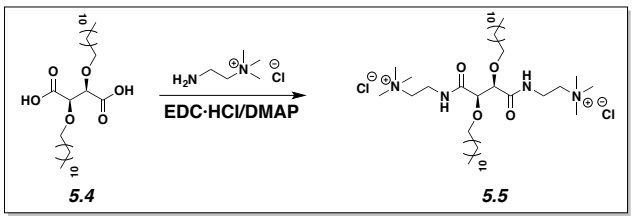

Figure 5.6. Synthesis of ether-linked CAm with quaternary ammonium as hydrophilic head groups.

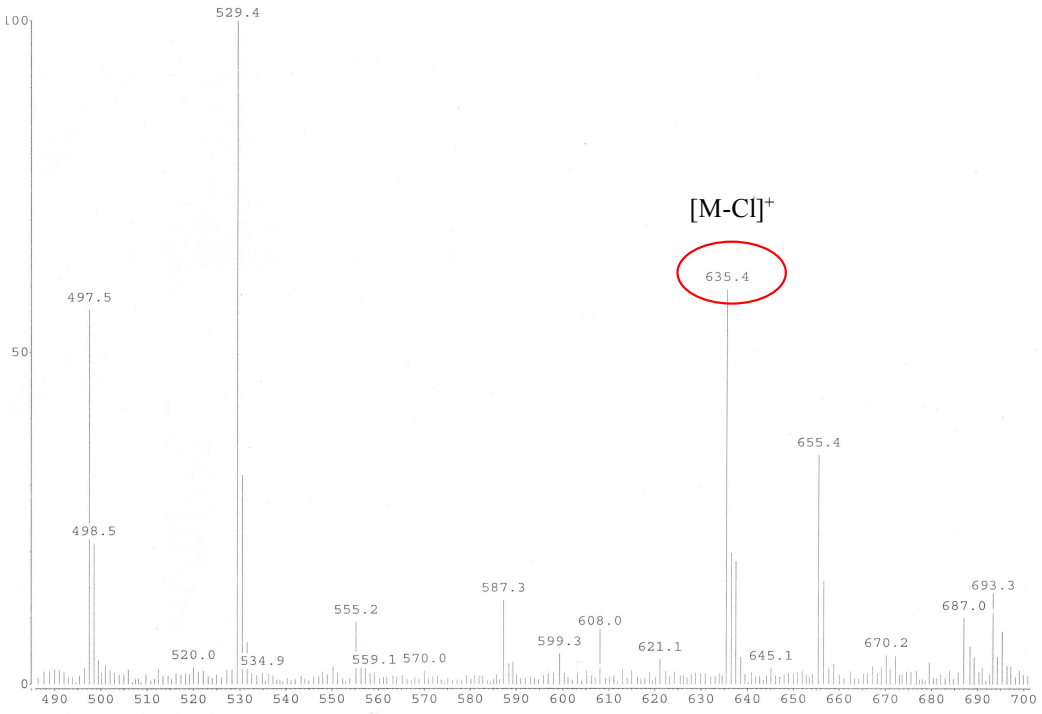

Figure 5.7. MS of reaction after 72 h, indicating the successful synthesis of product.

5.3.2. Experimental

Dialkylated tartaric acid ***5.1*** and ***5.4*** were prepared as previously described in 3.4.3.1.

5.3.2.1. Synthesis of *N*-Boc alkylated tartrate (***5.2***)

The conjugation of di-Boc-protected diamine was carried out following established procedure. Using ***5.2a*** as an example, ***5.1*** (119 mg, 0.32 mmol), EDC•HCl (255 mg, 1.33 mmol), and DMAP (77 mg, 0.63 mmol) were dissolved in 3 mL anhydrous DCM under argon. Upon complete dissolution, *N*-Boc-1,4-butanediamine (0.16 mL, 0.79 mmol) was added via syringe and the reaction stirred overnight at room temperature. The reaction mixture was washed with 10% $KHSO_4$ (2x 10 mL) and brine (1x 10 mL). The crude mixture was then dried over $MgSO_4$, filtered, and concentrated *in vacuo*. The crude product was then precipitated in chilled hexane (50 mL) and isolated via vacuum filtration.

5.2a. Yield: 205 mg, 91% (white powder). ^{1}H-NMR (400 MHz, $CDCl_3$): δ 4.20 (d, 2H), 3.56 (m, 4H), 3.32 (m, 4H), 3.13 (m, 4H), 1.54 (m, 12H), 1.44 (s, 18H), 1.26 (br, 20H), 0.88 (t, 6H). ^{13}C-NMR (500 MHz, $CDCl_3$): δ 169.97, 81.06, 73.39, 40.12, 38.79, 31.77, 29.68, 29.31, 29.23, 28.38, 27.46, 27.00, 25.99, 22.61, 14.07.

5.2b. Yield: 216 mg, 88% (white powder). ^{1}H-NMR (400 MHz, $CDCl_3$): δ 4.19 (d, 2H), 3.59 (m, 4H), 3.27 (m, 4H), 3.10 (m, 4H), 1.51 (m, 12H), 1.44 (s, 18H), 1.33 (m, 8H), 1.26 (br, 20H), 0.88 (t, 6H). ^{13}C-NMR (500 MHz, $CDCl_3$): δ 169.87, 81.06, 73.36, 40.41, 39.03, 31.77, 29.99, 29.69, 29.53, 29.32, 29.23, 28.40, 26.56, 26.39, 26.01, 22.61, 14.06.

5.3.2.2. Synthesis of ether-linked CAms (***5.3***)

The deprotection of ***5.2*** was conducted following an established procedure. Using ***5.3a*** as an example, in brief, ***5.2a*** (180 mg, 0.25 mmol) was dissolved in 2.5 mL HCl (4M in dioxane, 10.07 mmol) and cooled to 0 ˚C. The reaction mixture was stirred overnight and warmed to room temperature. The crude product was concentrated *in vacuo* and re-dissolved in minimal methanol (0.5 mL), followed by precipitation into a 50 mL centrifuge

tube containing chilled diethyl ether (45 mL). ***5.3a*** was then isolated via centrifugation (Hettich EBA 12, Beverly, MA; 3500 rpm, 3x 5 min) and the supernatant decanted.

5.3a. Yield: 148 mg, quantitative yield (off-white solid). ^{1}H-NMR (400 MHz, CD_3OD): δ 4.07 (s, 2H), 3.58 (m, 4H), 3.29 (m, 8H), 3.19 (m, 4H), 2.95 (m, 4H), 1.64 (m, 12H), 1.28 (br, 20H), 0.90 (t, 6H).

5.3b. Yield: 134 mg, quantitative yield (off-white solid). ^{1}H-NMR (400 MHz, CD_3OD): δ 4.07 (s, 2H), 3.58 (m, 4H), 3.29 (m, 8H), 3.19 (m, 4H), 2.95 (m, 4H), 1.64 (m, 4H), 1.55 (m, 8H), 1.40 (m, 8H), 1.28 (br, 20H), 0.90 (t, 6H).

5.3.2.3. Synthesis of ether-linked CAm with quaternary ammonium (***5.5***)

CAm ***5.5*** was prepared in a similar manner to ***5.2*** aforementioned. Briefly, ***5.4*** (81 mg, 0.17 mmol), (2-aminoethyl)trimethylammonium chloride hydrochloride (73 mg, 0.42 mmol), EDC•HCl (134 mg, 0.70 mmol), and DMAP (81 mg, 0.67 mmol) were dissolved in 3 mL anhydrous DCM under argon. The crude product was purified on neutral aluminum oxide via column chromatography using DCM: methanol (95:5) as eluent. Yield: 22 mg, 20 % (white solid). ^{1}H-NMR (400 MHz, $CDCl_3$): δ 4.15 (d, 2H), 3.87 (m, 8H), 3.64 (m, 4H), 3.47 (s, 4H), 1.58 (m, 4H), 1.23 (br, 36H), 0.87 (t, 6H). ESI-MS m/z: 599.5 $[M\text{-}Cl]^{+}$.

5.3.3. References

[1] Palermo EF, Vemparala S, Kuroda K. Cationic Spacer Arm Design Strategy for Control of Antimicrobial Activity and Conformation of Amphiphilic Methacrylate Random Copolymers. Biomacromolecules. 2012;13:1632-41.

[2] Nagamune H, Maeda T, Ohkura K, Yamamoto K, Nakajima M, Kourai H. Evaluation of the cytotoxic effects of bis-quaternary ammonium antimicrobial reagents on human cells. Toxicology in Vitro. 2000;14:139-47.

[3] Fulmer PA, Wynne JH. Development of Broad-Spectrum Antimicrobial Latex Paint Surfaces Employing Active Amphiphilic Compounds. ACS Applied Materials & Interfaces. 2011;3:2878-84.

[4] Jia Z, shen D, Xu W. Synthesis and antibacterial activities of quaternary ammonium salt of chitosan. Carbohydrate Research. 2001;333:1-6.

[5] Lu G, Wu D, Fu R. Studies on the synthesis and antibacterial activities of polymeric quaternary ammonium salts from dimethylaminoethyl methacrylate. Reactive and Functional Polymers. 2007;67:355-66.

[6] Faig A, Arthur TD, Fitzgerald PO, Chikindas M, Mintzer E, Uhrich KE. Biscationic Tartaric Acid-Based Amphiphiles: Charge Location Impacts Antimicrobial Activity. Langmuir. 2015;31:11875-85.

[7] Joglekar M, Roggers RA, Zhao Y, Trewyn BG. Interaction effects of mesoporous silica nanoparticles with different morphologies on human red blood cells. RSC Advances. 2013;3:2454-61.

[8] Sadeghi I, Yousefzadi M, Behmanesh M, Sharifi M, Moradi A. In vitro Cytotoxic and Antimicrobial Activity of Essential Oil From Satureja Intermedia. Iranian Red Crescent Medical Journal. 2013;15:70-4.

5.4. Investigation of Amphiphilic Macromolecule Precursors as Friction Modifier

(In collaboration with ExxonMobil Research and Engineering, Annandale, NJ)

Friction modifiers (FMs) are among the most important additives used in modern engine oils. Their use help improve fuel economy and energy efficiency by reducing friction in the boundary lubrication regime, and their effect is usually demonstrated by lowering of the coefficient of friction (COF) in standard tests [1, 2]. Two main categories of FMs are known: organic friction modifiers (OFMs) and inorganic friction modifiers mostly based on molybdenum compounds. OFMs are surfactant-like molecules with long alkyl chains and polar head groups, such as fatty acid esters, which work through either

physisorption or chemisorption of layers of molecules on the lubricated metal surfaces to form a thin film [1, 3]. However, when formulated in base oil, some of them suffer from poor solubility.

Synthetic intermediates of AMs, including T12 and M12 (**Figure 5.8**), are structurally similar to some OFMs and screened for their lubricating performance by high frequency reciprocating rig (HFRR) analyses. T12 and M12 are comprised of branched C12 lauric acid arms and two free carboxylic acid polar head groups. For the nomenclature, T and M stand for their tartaric acid and mucic acid backbones, respectively, while 12 stands for the alkyl chain length of fatty acid arms. Interestingly, under the same testing conditions, M12 exhibited COFs as high as ~ 0.13 at 100 ˚C, whereas T12 showed much lower friction (~ 0.04) at the same temperature. In addition, the more hydrophobic M12 had lower solubility in both Polyalphaolefin (PAO) and ester base stock oils. Based on these preliminary results, derivatives of T12 were designed, synthesized, and optimized for their friction-modifying performance. Furthermore, a thermo-triggered delivery system was attempted to both improve durability and provide sustained release in internal combustion engine.

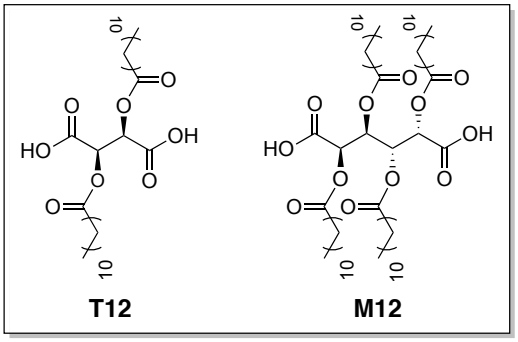

Figure 5.8. Chemical structures of T12 and M12.

5.4.1. Results and Discussion

Based on the structure of T12, different derivatives were synthesized and their friction modifying performances were evaluated at ExxonMobil's Corporate Strategic Research Laboratory (CSR) to establish their structure-activity relationship. Given that longer fatty acid chain promote an increase in the cohesive energy between chains and thus effectively decrease the minimum friction coefficient [4], palmitic acid (C16) was conjugated to the tartaric acid backbone and T16 was synthesized (**Figure 5.9**A). While only marginal improvement of COF was observed at 100 ˚C compared to T12, it has shown slightly improved solubility in base oil. However, when the alkyl chain length was further extended to C18 (i.e., stearic acid), COF values as low as 0.025 were obtained at 100 ˚C such thus T18 was identified as lead candidate compound. In fact, this COF value is among the lowest values known, even when compared to commercially available FMs.

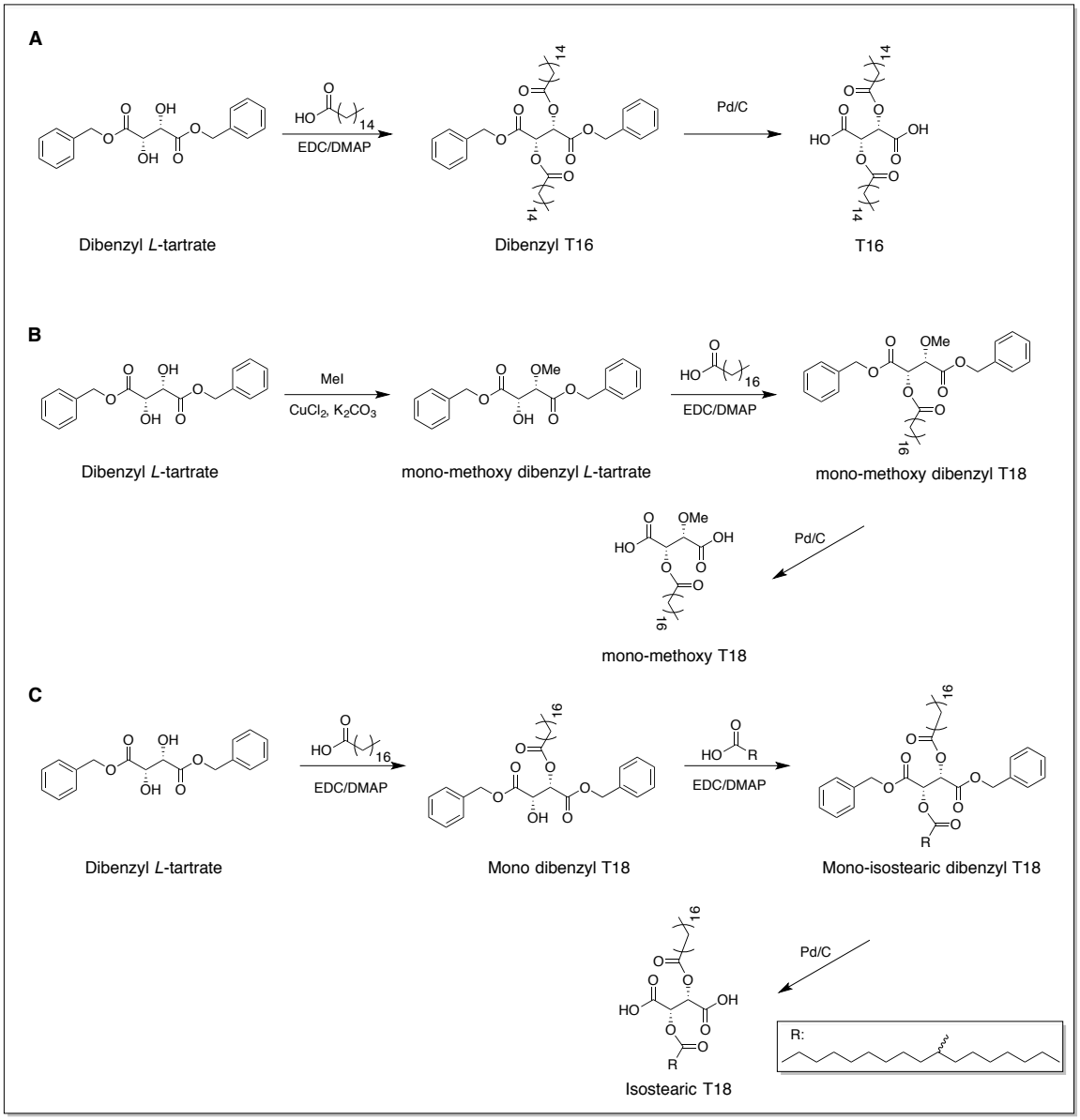

Figure 5.9. Synthetic schemes of T16 (A), mono-methoxy T18 (B), and isostearic T18 (C).

To investigate the influence of molecular symmetry in structure on COF, mono-methoxy T18 was synthesized (**Figure 5.9**B). The mono-alkylation of dibenzyl *L*-tartrate was carried out with a copper catalyst in the presence of a base. Interestingly, even with one stearic acid arm per molecule, it exhibited excellent friction-modifying capability (**Figure 5.10**). While its COF was higher than that of T18 at 100 ˚C, its performance was

even better than T18 at 150 ˚C (0.039 vs 0.056). The mechanism remains unclear and is under investigation.

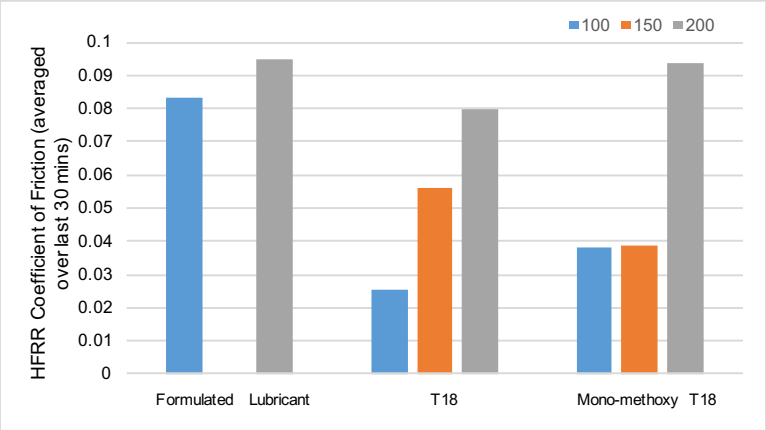

Figure 5.10. Averaged COFs of T18 and mono-methoxyl T18 over last 30 minutes in HFRR experiments under three different temperatures.

To develop a thermo-responsive system that can release T18 over time, di-*tert*-butyl T18 was prepared. The tertiary ester protecting groups of di-*tert*-butyl T18 are expected to be cleaved at high temperatures [5] and result in release of T18, which by itself is an efficient friction modifier.

5.4.2. Experimental

5.4.2.1. Synthesis of dibenzyl T16

Dibenzyl *L*-tartrate (1.00 g, 3.03 mmol), palmitic acid (1.70 g, 6.67 mmol), EDC•HCl (1.74 g, 9.10 mmol), and DMAP (0.81 g, 6.66 mmol) were dissolved in 30 mL anhydrous DCM under argon and the reaction mixture was stirred overnight at room temperature. The reaction mixture was washed with 10% $KHSO_4$ (2 x 100 mL) and brine

(1 x 100 mL). The crude mixture was then dried over $MgSO_4$, filtered, and concentrated *in vacuo*. The crude product was then precipitated in chilled hexane (150 mL) and isolated via vacuum filtration. Yield: 2.10 g, 85% (white solid). ^{1}H-NMR (400 MHz, $CDCl_3$): δ 7.32 (m, 10H), 5.75 (s, 2H), 5.16 (q, 4H), 2.21 (m, 4H), 1.53 (m, 4H), 1.25 (br, 48H), 0.88 (t, 6H). ^{13}C-NMR ($CDCl_3$): δ 172.38, 165.73, 134.78, 128.62, 128.60, 128.47, 70.55, 67.67, 33.43, 31.92, 29.70, 29.66, 29.62, 29.46, 29.36, 29.23, 28.96, 24.58, 22.69,14.11.

5.4.2.2. Synthesis of T16

Following published procedure [6], dibenzyl T16 (2.10 g, 2.60 mmol) was dissolved in 26 mL DCM followed by addition of 0.21 g palladium on carbon (Pd/C, 10 wt%). The reaction stirred under H_2 gas for 24 h. the reaction mixture was filtered through a column of celite and washed several times with DCM. The filtrate was concentrated *in vacuo* to obtain pure T16. Yield: 1.50 g, 94% (white solid). ^{1}H-NMR (400 MHz, $CDCl_3$): δ 5.56 (s, 2H), 2.30 (m, 4H), 1.51 (m, 4H), 1.32 (br, 48H), 0.76 (t, 6H). ^{13}C-NMR ($CDCl_3$): δ 172.49, 70.76, 33.69, 31.86, 29.57, 29.53, 29.40, 29.24, 29.17, 28.96, 28.93, 24.64, 22.58,14.05. ESI-MS m/z: 625.3 $[M-H]^-$.

5.4.2.3. Synthesis of mono-methoxyl dibenzyl *L*-tartrate

Following a published procedure [7], dibenzyl *L*-tartrate (1.00 g, 3.00 mmol), methyl iodide (MeI, 1.87 mL, 30.00 mmol), copper (II) chloride ($CuCl_2$, 40 mg, 0.30 mmol), and potassium carbonate (K_2CO_3, 622 mg, 4.50 mmol) were weighed and dissolved in 25 mL DMF. The reaction was stirred for 36 h. The solvent was removed *in vacuo* and resuspended in 50 mL DCM. The organic layer was washed with 0.1 N HCl (1x 100 mL) and extracted with ethyl acetate (3x 50 mL). The combined organic layer was dried over MgSO4, filtered, and concentrated *in vacuo*. The crude product was purified on silica gel

via column chromatography using a hexane: ethyl acetate gradient (95:5 to 90:10). Yield: 797 mg, 80% (white solid). ^{1}H-NMR (400 MHz, $CDCl_3$): δ 7.36 (m, 10H), 5.23 (m, 4H), 4.64 (d, 2H), 4.18 (s, 1H), 3.32 (s, 3H).

5.4.2.4. Synthesis of mono-methoxy dibenzyl T18

Mono-methoxy dibenzyl T18 was prepared in a manner similar to dibenzyl T16. In brief, mono-methoxyl dibenzyl *L*-tartrate (797 mg, 2.31 mmol), stearic acid (724 mg, 2.55 mmol), EDC•HCl (663 mg, 3.47 mmol), and DMAP (311 mg, 2.55 mmol) were dissolved in 20 mL anhydrous DCM under argon and the reaction stirred overnight at room temperature. Yield: 1.4 g, quantitative yield (white solid). ^{1}H-NMR (400 MHz, $CDCl_3$): δ 7.33 (m, 10H), 5.62 (d, 1H), 5.20 (m, 4H), 4.39 (d, 1H), 3.38 (s, 3H), 2.22 (m, 2H), 1.52 (m, 2H), 1.26 (br, 28H), 0.88 (t, 3H). ESI-MS m/z: 633.8 $[M+Na]^+$.

5.4.2.5. Synthesis of mono-methoxy T18

Mono-methoxy T18 was prepared in a similar manner to T16. In brief, mono-methoxyl dibenzyl T18 (1.40 g, 2.29 mmol) was dissolved in 20 mL DCM followed by addition of 0.14 g palladium on carbon (Pd/C, 10 wt%). The reaction stirred under H_2 gas for 24 h. Yield: 937 mg, 95% (off-white solid). ^{1}H-NMR (400 MHz, $CDCl_3$): δ 5.57 (s, 1H), 4.37 (s, 1H), 3.51 (s, 3H), 2.40 (q, 4H), 1.61 (m, 4H), 1.24 (br, 28H), 0.86 (t, 3H). ^{13}C-NMR ($CDCl_3$): δ 172.77, 79.31, 72.25, 59.90, 33.79, 31.90, 29.68, 29.65, 29.63, 29.62, 29.46, 29.33, 29.25, 29.05, 24.73, 22.66,14.10.

5.4.2.6. Synthesis of mono dibenzyl T18

Dibenzyl *L*-tartrate (5.00 g, 15.14 mmol), EDC•HCl (0.87 g, 3.03 mmol), and DMAP (0.41 g, 3.33 mmol) were dissolved in 20 mL anhydrous DCM. In a separate flask, stearic acid (0.86 g, 3.03 mmol) was dissolved in 12 mL DCM/DMF (5:1) and added

dropwise via syringe pump to the solution of reaction mixture over 6 h. The reaction was stirred overnight. The reaction mixture was washed with 1N HCl (3 x 50 mL) and brine (1 x 50 mL). The crude mixture was then dried over $MgSO_4$, filtered, and concentrated *in vacuo*. The crude product was purified on silica gel via column chromatography using hexane: DCM: ethyl acetate (85:10:5). Yield: 1.13 g, 63% (white solid). ^{1}H-NMR (400 MHz, $CDCl_3$): δ 7.34 (m, 10H), 5.51 (s, 1H), 5.23 (m, 4H), 4.82 (d, 1H), 3.09 (s, 3H), 2.19 (m, 2H), 1.54 (m, 2H), 1.26 (br, 28H), 0.88 (t, 3H). ESI-MS m/z: 597.9 $[M+H]^+$.

5.4.2.7. Synthesis of mono-isostearic dibenzyl T18

Mono dibenzyl T18 (0.90 g, 1.53 mmol), isostearic acid (80% purity, mostly 2-octyldecanoic acid, 0.60g, 1.68 mmol), EDC•HCl (0.44 g, 2.30 mmol), and DMAP (0.21 g, 1.68 mmol) were dissolved in 15 mL anhydrous DCM under argon and the reaction stirred overnight at room temperature. The crude mixture was then dried over $MgSO_4$, filtered, and concentrated *in vacuo*. The crude product was purified on silica gel via column chromatography using hexane: ethyl acetate gradient (95:5). Yield: 1.12 g, 85% (white solid). ^{1}H-NMR (400 MHz, $CDCl_3$): δ 7.33 (m, 10H), 5.74 (s, 2H), 5.16 (q, 4H), 2.21 (m, 3H), 1.54 (m, 5H), 1.26 (br, 51H), 0.88 (t, 9H).

5.4.2.8. Synthesis of isostearic T18

Isostearic T18 was prepared as discussed previously with T16. In brief, mono-isostearic dibenzyl T18 (1.12 g, 1.30 mmol) was dissolved in 13 mL DCM followed by addition of 0.11 g palladium on carbon (Pd/C, 10 wt%). The reaction stirred under H_2 gas for 24 h. Yield: 866 mg, 98% (yellow paste). ^{1}H-NMR (400 MHz, $CDCl_3$): δ 5.76 (s, 1H), 2.43 (m, 3H), 1.64 (m, 5H), 1.25 (br, 51H), 0.87 (m, 9H).

5.4.2.9. Synthesis of di-*tert*-butyl T18

Di-*tert*-butyl *L*-tartrate (150 mg, 0.57 mmol), stearic acid (358 mg, 1.26 mmol), EDC•HCl (328 mg, 1.72 mmol), and DMAP (154 mg, 1.26 mmol) were dissolved in 7 mL anhydrous DCM under argon and the reaction stirred overnight at room temperature. The reaction mixture was washed with 10% $KHSO_4$ (2 x 20 mL) and brine (1x 20 mL). The crude mixture was then dried over $MgSO_4$, filtered, and concentrated *in vacuo*. The crude product was then precipitated in chilled hexane (50 mL) and isolated via vacuum filtration. Yield: 373 mg, 82% (white solid). ^{1}H-NMR (400 MHz, $CDCl_3$): δ 5.61 (s, 2H), 2.40 (m, 4H), 1.62 (m, 4H), 1.43 (s, 18H), 1.24 (br, 56H), 0.87 (t, 6H). ^{13}C-NMR (500 MHz, $CDCl_3$): δ 172.54, 164.89, 83.24, 70.98, 33.65, 31.92, 29.76, 29.70, 29.68, 29.66, 29, 60, 29.44, 29.37, 29.23, 29.10, 27.86, 24.71, 22.69, 14.12. IR (cm^{-1}, $CHCl_3$): 3100 – 3600 (COOH), 1744 (C=O). ESI-MS m/z: 817.2 $[M+Na]^+$.

5.4.2.10. Coefficient of friction *(Performed and written by ExxonMobil, Corporate Strategic Research Laboratory (CSR), Annandale, NJ)*

The friction modifying performance of AM precursor additive oil samples was measured by the HFRR under boundary conditions. The reference oil was also subjected to the same test conditions to establish the COF in the absence of friction modifiers. The HFRR test configuration was an oscillating ball-on-disk, with ball and disk hardware immersed in oil. The device used was a HFRR (PCS Instruments, London, UK). The HFRR conditions were a load of 400 g (translates to a 1 GPa Herzian contact), a reciprocating frequency of 60 Hz, and a stroke length of 1.0 mm. The tests were run for a total of 2 h under isothermal conditions. The ball was a 52100 steel with a typical hardness of 800 Hv. The disk was a 52100 steel with a typical hardness of 200 Hv. Friction was measured with

a load cell, and film thickness between the rubbing surfaces of the ball and disk were measured electrically.

5.4.3. References

[1] Ratoi M, Niste VB, Alghawel H, Suen YF, Nelson K. The impact of organic friction modifiers on engine oil tribofilms. RSC Advances. 2014;4:4278-85.

[2] Kenbeek D, Buenemann T, Rieffe H. Review of Organic Friction Modifiers-Contribution to Fuel Efficiency? : SAE Technical Paper; 2000.

[3] Ratoi M, Bovington C, Spikes H. In Situ Study of Metal Oleate Friction Modifier Additives. Tribology Letters.14:33-40.

[4] Jahanmir S, Beltzer M. Effect of additive molecular structure on friction coefficient and adsorption. Journal of tribology. 1986;108:109-16.

[5] Chen S, Du X, Ye G, Cao J, Sun H, Xiao Z, et al. Thermo-cleavable fullerene materials as buffer layers for efficient polymer solar cells. Journal of Materials Chemistry A. 2013;1:11170-6.

[6] Abdelhamid DS, Zhang Y, Lewis DR, Moghe PV, Welsh WJ, Uhrich KE. Tartaric acid-based amphiphilic macromolecules with ether linkages exhibit enhanced repression of oxidized low density lipoprotein uptake. Biomaterials. 2015;53:32-9.

[7] Maki T, Ushijima N, Matsumura Y, Onomura O. Catalytic monoalkylation of 1,2-diols. Tetrahedron Letters. 2009;50:1466-8.

6. Copyright Permission

6.1. Biomaterials I

Title: Tartaric acid-based amphiphilic macromolecules with ether linkages exhibit enhanced repression of oxidized low density lipoprotein uptake

Author: Dalia S. Abdelhamid,Yingyue Zhang,Daniel R. Lewis,Prabhas V. Moghe,William J. Welsh,Kathryn E. Uhrich

Publication: Biomaterials

Publisher: Elsevier

Date: June 2015

Order Completed

Thank you for your order.

This Agreement between Yingyue Zhang ("You") and Elsevier ("Elsevier") consists of your license details and the terms and conditions provided by Elsevier and Copyright Clearance Center.

Your confirmation email will contain your order number for future reference.

Get the printable license.

License Number	3890510643237
License date	Jun 15, 2016
Licensed Content Publisher	Elsevier
Licensed Content Publication	Biomaterials
Licensed Content Title	Tartaric acid-based amphiphilic macromolecules with ether linkages exhibit enhanced repression of oxidized low density lipoprotein uptake
Licensed Content Author	Dalia S. Abdelhamid,Yingyue Zhang,Daniel R. Lewis,Prabhas V. Moghe,William J. Welsh,Kathryn E. Uhrich
Licensed Content Date	June 2015
Licensed Content Volume	53
Licensed Content Issue	n/a
Licensed Content Pages	8
Type of Use	reuse in a thesis/dissertation
Portion	full article
Format	both print and electronic
Are you the author of this Elsevier article?	Yes
Will you be translating?	No
Order reference number	
Title of your thesis/dissertation	DESIGN, SYNTHESIS, AND CHARACTERIZATION OF AMPHIPHILIC MOLECULES FOR BIOMEDICAL APPLICATIONS
Expected completion date	Jun 2016
Estimated size (number of pages)	140
Elsevier VAT number	GB 494 6272 12
Requestor Location	Yingyue Zhang Rutgers University PISCATAWAY, NJ 08854 United States

6.2. Biomaterials II

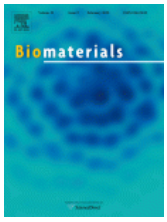

Title:	Micellar and structural stability of nanoscale amphiphilic polymers: Implications for anti-atherosclerotic bioactivity
Author:	Yingyue Zhang,Qi Li,William J. Welsh,Prabhas V. Moghe,Kathryn E. Uhrich
Publication:	Biomaterials
Publisher:	Elsevier
Date:	April 2016

Order Completed

Thank you for your order.

This Agreement between Yingyue Zhang ("You") and Elsevier ("Elsevier") consists of your license details and the terms and conditions provided by Elsevier and Copyright Clearance Center.

Your confirmation email will contain your order number for future reference.

Get the printable license.

License Number	3890510773066
License date	Jun 15, 2016
Licensed Content Publisher	Elsevier
Licensed Content Publication	Biomaterials
Licensed Content Title	Micellar and structural stability of nanoscale amphiphilic polymers: Implications for anti-atherosclerotic bioactivity
Licensed Content Author	Yingyue Zhang,Qi Li,William J. Welsh,Prabhas V. Moghe,Kathryn E. Uhrich
Licensed Content Date	April 2016
Licensed Content Volume	84
Licensed Content Issue	n/a
Licensed Content Pages	11
Type of Use	reuse in a thesis/dissertation
Portion	full article
Format	both print and electronic
Are you the author of this Elsevier article?	Yes
Will you be translating?	No
Order reference number	
Title of your thesis/dissertation	DESIGN, SYNTHESIS, AND CHARACTERIZATION OF AMPHIPHILIC MOLECULES FOR BIOMEDICAL APPLICATIONS
Expected completion date	Jun 2016
Estimated size (number of pages)	140
Elsevier VAT number	GB 494 6272 12
Requestor Location	Yingyue Zhang Rutgers University PISCATAWAY, NJ 08854 United States Attn: Yingyue Zhang
Total	0.00 USD